To the University of Wyoming:

The members of the Committee approve the thesis of Cody L. Perkins presented on August 25th, 2022.

Dr. Dimitri Mavriplis, Chairperson

Dr. Bart Geerts, Outside Member

Dr. Michael Stoellinger

,

APPROVED:

Dr. Erica Belmont, Head, Department of Mechanical Engineering

Dr. Cameron Wright, Dean, College of Engineering and Applied Sciences

Perkins, Cody L., *Computational Analysis of a Slotted, Natural-Laminar-Flow Transonic Truss-Braced Wing Aircraft Configuration*, M.S., Department of Mechanical Engineering, December, 2022.

The integration of a slotted, natural-laminar-flow (SNLF) airfoil with a transonic, truss-braced wing (TTBW) configuration has been shown to offer significant benefits in comparison to other widely implemented designs for commercial aircraft transport applications. This work focuses on the computational analysis of the S207 airfoil and it's derivative geometries. Two-dimensional analysis concerned the baseline geometry and three drooped leading-edge variants. Three-dimensional analysis scrutinized several iterations of a S207 SNLF TTBW vehicle and an SNLF swept wing wind tunnel model. The performance of SNLF technology is largely dependent on the duration of laminar flow maintained across the chord length. Thus proper prediction of the transition from laminar to turbulent flow and its sensitivity to geometric changes is of top priority. Computations were performed using Reynolds-averaged Navier-Stokes (RANS) solvers on unstructured grids with partial-differential equation (PDE)-based transition prediction models. Results of the baseline geometry agree closely with design performance metrics, and also illustrate the sensitivity of this airfoil to flap positioning. Data acquired for the drooped variants show success in preventing stall and increasing lift but discrepancies are observed between various solvers. Computational results for the S207 SNLF TTBW vehicle were instrumental in uncovering and rectifying several wing design flaws. The final geometry was analyzed extensively over a range of Mach numbers and angles of attack, and these three-dimensional computational results were provided to partners at The Boeing Company for further vehicle performance assessment. Finally, the computational results for the wind-tunnel model were compared to experimental data, showing similar trends but larger regions of turbulent flow compared to experimental flow visualization.

COMPUTATIONAL ANALYSIS OF A SLOTTED, NATURAL-LAMINAR-FLOW TRANSONIC TRUSS-BRACED WING AIRCRAFT CONFIGURATION

by

Cody L. Perkins, B.S.M.E.

A thesis submitted to the
Department of Mechanical Engineering
and the
University of Wyoming
in partial fulfillment of the requirements
for the degree of

MASTER OF SCIENCE
in
MECHANICAL ENGINEERING

Laramie, Wyoming
December 2022

Contents

List of Figures

List of Tables

Acknowledgments

First and foremost the author would like to extent his gratitude to Dr. Dimitri Mavriplis who served as advisor for this project and has offered extensive guidance over the last two years. The author considers himself incredibly fortunate to have studied under the mentorship of an individual not only of such renown and achievement, but also one who demonstrates humility, diligence, and compassion. Further gratitude is extended to the other members of the advisory committee, Dr. Michael Stoellinger and Dr. Bart Geerts, who both offered notable suggestions in strengthening this thesis. Additional acknowledgement is given to members, both past and present, of the Mavriplis CFD Lab who have often been key in expediting the author's learning and educational experiences: Zhi Yang, Emmett Padway, Andrew Kirby, Soudeh Kamali, Ilker Topcuoglu, Sung Yoon, Enrico Fabiano, and Matteo Ugolotti. Finally, the author would like to thank the network of friends and family who supported this endeavor: Ethan, Alex, Tanner, Adam, Delta, Robert, Gavin, Brendan, Matt, Dalton, Nate, Gabi, Anthony, Devin, and Kailey. A special thanks is given to the author's mother, Sandy Kingsley, whose actions were not only an example in perseverance, but were a deciding factor in the author's ability to pursue an advanced degree.

Cody L. Perkins

University of Wyoming

December 2022

Chapter 1

Introduction

1.1 Need for Improvement

The International Energy Agency reported a 126.6% increase in international aviation energy consumption between 1990 and 2017, with the United States attaining a growth of 89.4% [1]. Consequently, air travel is progressively playing a more prominent role in the global warming crisis. Individual use of private aircraft alone make contributions of 7500 tons of emitted CO_2 per year [2], and a 2018 study estimated a 2.18ppm increase in the atmospheric concentration of CO_2 due to the aviation industry [3]. This undeniable rise in greenhouse gas emissions comes with the necessity to develop and implement preventative improvements to aircraft technology.

The NASA Aeronautics Research Mission Directorate (ARMD) has formulated six thrusts in response to global climate change and other drivers shaping the needs of the aviation industry [4], each with their own near-term (N+1), mid-term (N+2), and far-term (N+3) metrics. The third thrust outlines long-term improvements to subsonic transport aircraft, making them more economically viable and environmentally conscious. Technology associated with N+3 criteria will contribute to a fleet-level net reduction in emissions of 50% compared to a 2005 baseline. This goal is realistically attainable within the specified timeline only if extensive progress is made in the realms of air-frames, propulsion, vehicle systems integration, and modeling and simulation capabilities.

1.2 Slotted, Natural-Laminar-Flow Technology

A typical analysis on the topic of boundary layer theory is consideration of flow over a flat plate of arbitrary length and width. Comparing two solutions for this problem, one assuming a laminar boundary layer and the other a turbulent boundary layer, provides significant insight into the benefits of extensive runs of laminar flow. The laminar boundary layer is characterized by constant streamlines and no random variations in the velocity field. On the contrary, the turbulent boundary layer is characterized by random variations in the velocity field and continual mixing. Turbulent boundary layers are also thicker than laminar boundary layers. A sketch characterizing the differences in these two solutions is included as Figure 1.1.

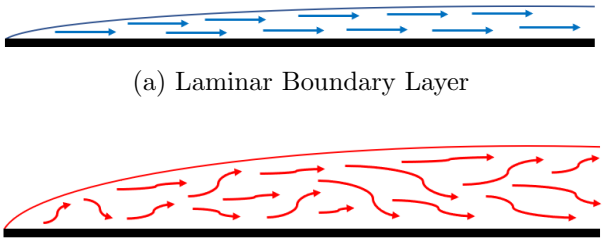

(a) Laminar Boundary Layer

(b) Turbulent Boundary Layer

Figure 1.1: Sketched Geometric and Velocity Characteristics of Laminar and Turbulent Boundary Layers on a Flat Plate for Left to Right Moving FLow

In the case where the Reynolds number based on plate-length is 1 million, the turbulent boundary layer solution, which is the expected solution for a Reynolds number of this magnitude, is accompanied by a skin friction drag coefficient that is 3.3 times that of the laminar boundary layer solution [5]. In other words, the drag forces due to friction between the fluid and the flat plate surface become more prominent when the boundary layer is turbulent. In the context of aircraft design this behavior becomes important for consideration as delaying the transition from laminar to turbulent flow offers a route to improved efficiency through a reduction in overall drag. Unfortunately, transonic aircraft struggle to maintain significant runs of laminar flow across the entirety of the wing due to the associated high Reynolds numbers at flight conditions. Fabricating a solution that successfully stabilizes the boundary layer and prevents transition from laminar to turbulent flow can be a key factor

for meeting N+3 goals. One such method, among others, is the application of a natural-laminar flow (NLF) airfoil. Through careful shaping of the airfoil cross-section, a favorable pressure gradient is established as far along the chord length as possible. This gradient is favorable in the sense that the streamwise pressure decreases along the surface of the airfoil in the downstream direction (i.e. $dp/dx < 0$), creating a less hostile environment for the flow. On the other hand, an adverse pressure gradient results in a streamwise pressure force that increases as a function of downstream position on the surface of the airfoil (i.e. $dp/dx > 0$). Ultimately, the pressure becomes substantial enough to destabilize the boundary layer and the transition from laminar to turbulent flow occurs. A sketch illustrating the benefits of a negative pressure gradient on the curved surface of an airfoil in comparison to a positive pressure gradient is shown in Figure 1.2. Ultimately, NLF airfoils are capable of achieving laminar flow up to 70% the chord length on the upper and lower surfaces as a result of successfully established favorable pressure gradients [5, 6].

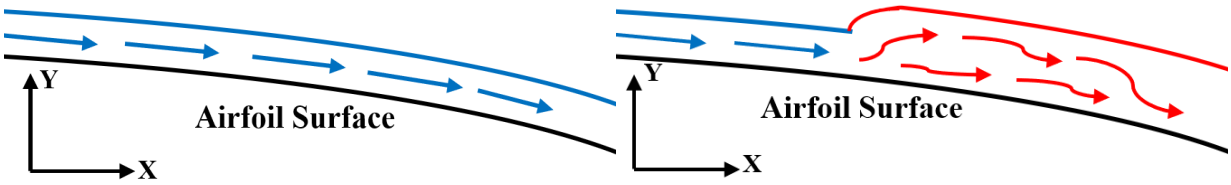

(a) Favorable Pressure Gradient ($dp/dx < 0$) (b) Adverse Pressure Gradient ($dp/dx > 0$)

Figure 1.2: Expected Boundary Layer Behavior as a Function of Boundary Layer Direction

Slotted, natural-laminar-flow (SNLF) technology was first proposed by Somers in 2005 [7] and seeks to improve upon the performance of NLF airfoils. It differs through the addition of an aft element, introducing design considerations characterized by the flow present between the two elements, a region more commonly known as the slot. A diagram of the S103 SNLF airfoil, which was designed for general aviation applications [6], is included in Figure 1.3 as an example. The flow through the slot facilitates a favorable pressure gradient on the upper surface of the fore element. The trailing-edge pressure of the fore element becomes lower than freestream pressure due to the velocity of the flow at the slot exit [8]. This is also referred to as the dumping velocity [9]. This gradient stabilizes the boundary layer, offering

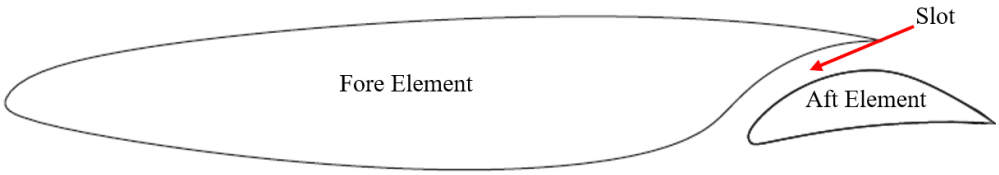

Figure 1.3: The S103 Slotted, Natural-Laminar-Flow Airfoil

two distinct benefits. First, laminar flow is theoretically achieved for the entire chord length of the fore element and a notable portion of the aft element, reducing skin friction drag even further than what an NLF airfoil is capable of. Second, a reduction in profile drag is achieved through prevention of flow separation. In the context of commercial transport vehicles, this becomes incredibly beneficial as wing profile drag accounts for roughly 1/3 of the total drag acting on the aircraft [6]. Additionally, SNLF technology lends itself to lighter aircraft. It is less complex mechanically, structurally, and operationally than other profile drag reduction techniques such as active laminar flow control and active high lift systems [7]. SNLF airfoils also have high maximum lift coefficients, especially at low-speeds, permitting a reduction in wing planform [8].

The low-drag bucket is an attribute unique to NLF, and by extension SNLF, type airfoils and is characterized by a minimum in drag across a large range of lift coefficient (C_L) values. It is bounded by the upper and lower C_L conditions, beyond which a significant increase in drag is observed. This is due to the movement of the boundary-layer transition line further upstream for conditions outside of the drag bucket C_L range, resulting in increased turbulence [10]. A performance polar illustrating the formation of the low-drag bucket can be viewed in Figure 1.4. Design values for the upper and lower C_L values are determined based on desired aircraft application.

The study of already existing SNLF geometries offer testament to the technology's benefits. The S414 is an SNLF airfoil proposed for rotor-craft applications. This airfoil was designed to meet high maximum lift and low profile drag objectives through both computational analysis and wind tunnel testing [11, 12]. Furthermore, comparison of these results to those of a single-element NLF airfoil of similar design highlighted the benefit of the slot. The S204 SNLF airfoil is designed for business jet applications and was also able to achieve

high maximum lift and low profile drag goals based upon initial computational analysis [13].

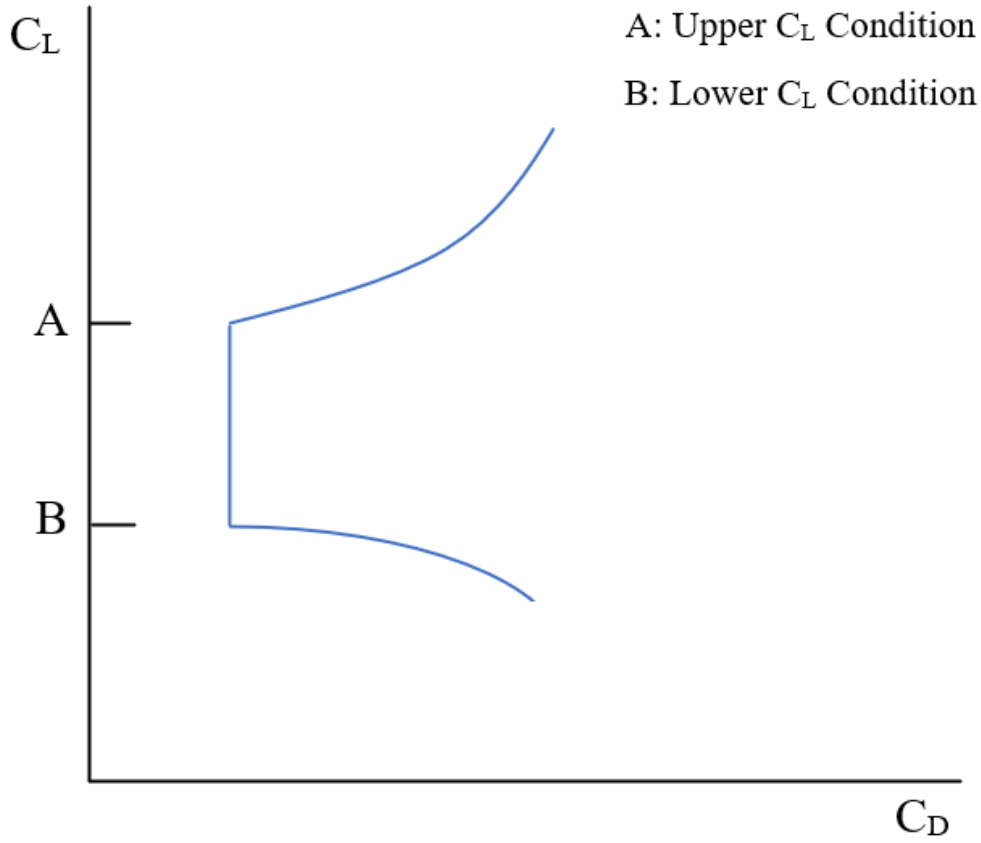

Figure 1.4: Illustration of the Low-Drag Bucket for NLF-type Wings

1.3 The S207 SNLF Airfoil and Relevant Configuration

The S207 is a 13.49%-thick SNLF airfoil designed for transonic commercial transport applications [8, 10]. It is insensitive to roughness and computational results predict the lower and upper C_L limits for the low-drag bucket region to be 0.37 and 0.74 for a Mach number of 0.700 and Reynolds number of 13.2 million, respectively [10]. The maximum C_L value at a Mach number of 0.225 and Reynolds number of 16.0 million is initially computed to be 2.13. The profile of the S207 is included as Figure 1.5. Design metrics for this airfoil were derived from the Boeing Mach 0.745 Transonic Truss-Braced Wing (TTBW) aircraft [8], a concept that utilizes a large aspect-ratio wing and was designed under the

Subsonic Ultra Green Aircraft Research (SUGAR) initiative [14]. A concept illustration of a TTBW configuration can be viewed in Figure 1.6. It has been found that pairing the S207 airfoil with a TTBW structure has the potential to decrease the block fuel per seat by approximately 58% compared to the SUGAR free baseline geometry [8].

Current efforts conducted under the Advanced Aerodynamic Design Center for Ultra-Efficient Commercial Vehicles, which is a NASA funded University Leadership Initiative (ULI) led by the University of Tennessee at Knoxville, are focused on the extensive analysis of a S207-based SNLF TTBW vehicle configuration with the goal being a 70% reduction in fuel and energy burn compared to 2005 standards [15]. Through the course of this project, the superior performance this vehicle offers in comparison to modern aircraft has been demonstrated [16]. This thesis summarizes the methodology and results associated with a collaborative effort to support the ULI project through computational analysis of the S207 airfoil and associated TTBW aircraft. Data presented will first detail the performance of the S207 airfoil as well as three morphed leading-edge variants in two dimensions. Three-dimensional results for several S207 SNLF TTBW configurations as well as a wind tunnel model representative of the aircraft wing are included in the latter chapters. It is appropriate to note that work described in this thesis has been published in references [17, 18].

Figure 1.5: S207 Slotted, Natural-Laminar-Flow Airfoil Geometry

Figure 1.6: Boeing TTBW Aircraft Concept Configuration

Chapter 2

Methodology

2.1 Predicting Transition

Most transport aircraft today employ a high-lift system composed of a main element, a slat at the leading-edge, and a select number of trailing-edge flaps. The slat and trailing-edge flaps are deployed during takeoff and landing to increase lift, but both systems are retracted during cruise to create a more streamlined airfoil shape. The retraction of the slat in particular creates an imperfect step geometry near the leading-edge of the wing, causing the transition from laminar to turbulent flow [7]. As an example, the takeoff and cruise configurations of the 30P30N airfoil, a multi-element, high-lift airfoil designed by McDonnell Douglas [19], is shown in Figure 2.1.

The use of a slat is incompatible with natural-laminar-flow, as it triggers the transition from the laminar to turbulent regime very near the leading-edge. It is for this reason that an SNLF airfoil such as the S207 airfoil is designed without a slat. That is not to say, however, that instances of transition are not present on an SNLF wing. Turbulence is expected on a measurable portion of the upper surface of the flap near the trailing-edge [10]. Presence of both the laminar and turbulent regimes adds complexity to the computational analysis of an SNLF airfoil. Whereas a high-lift system can be studied exclusively using the fully turbulent flow assumption, an SNLF airfoil must be analyzed with an approach in which the turbulence model is coupled with a transition prediction model. This modeling strategy is

(a) Slat and Flap Deployed

(b) Slat and Flap Stowed

Figure 2.1: McDonnell Douglas 30P30N High-Lift Airfoil

commonly referred to as free transition.

This work concerns itself with the use of two transition prediction models. The first is the single-equation Menter model [20]. This model draws its foundation from the concept of Local-Correlation-based Transition Modeling (LCTM) and is an improvement on the two-equation γ-Re model [21, 22]. The need for the Re-equation is removed, making the model exclusively dependent on the turbulence intermittency (γ) for triggering the transition from laminar to turbulent flow. The second is the Two-Equation Amplification Factor Transport (AFT2 or AFT2019) model [23]. Founded on linear stability theory, the model computes the progression of the amplification factor associated with streamwise instabilities. This transport equation is coupled with an intermittency equation as well. The transition criterion is met once the maximum amplification ratio of any considered instability in the boundary layer reaches a specific value denoted N_{crit}. This parameter can be used as a direct input or computed from freestream turbulence intensity (Tu_∞) using Mack's relationship [23, 24]. It is necessary to note that these models do not account for all mechanisms of transition, particularly crossflow instabilities are not taken considered in the models. This mechanism becomes more relevant with increasing wing sweep and is dominant when wing sweep is above 15° [8]. The SNLF wing analyzed under ULI project efforts was intentionally designed to

have a sweep of 12.5° to minimize concern for crossflow instabilities. Therefore, this design decision validates the use of the AFT2 and Menter transition prediction models for use in this work. Both models have been implemented into the RANS solvers used for this work by Zhi Yang [25].

2.2 Solutions in 2D

In this work, two-dimensional CFD analyses were performed using NSU2D [26]. NSU2D is an in-house developed steady-state code that solves the compressible RANS equations on unstructured grids. The NSU2D spatial discretization method is a central difference scheme with added matrix-based dissipation and is nominally second-order accurate. An efficient multigrid scheme can be utilized to accelerate convergence, but various other solver modules are available as well. Modeling capabilities include various turbulence models and transition prediction. Two-dimensional results presented in this work are computed using either the Spalart-Allmaras (SA) turbulence model [27] alone or with a coupled SA-AFT2 implementation [25]. The AFT2 model parameter N_{crit} is computed from an input for freestream turbulence intensity. Grids for the 2D CFD anlayses performed in this work were generated using UMESH2D [28], a code associated with the NSU2D software package.

2.3 Solutions in 3D

The three-dimensional CFD analyses performed in this work were acquired using NSU3D [29]. Like NSU2D, this software is a steady-state RANS solver, and it extends the schemes, accuracy, and capabilities of its predecessor to three dimensions. NSU3D is compatible with various grid formats including hybrid grids that have various cell types. The code has been extensively validated through its use in previous high-lift, drag prediction and aeroelastic prediction workshops [30–32]. The three-dimensional CFD analyses performed in this work will include data generated from approaches utilizing either the Menter model or the AFT2 model for transition prediction, and only the SA model for turbulence modeling. The AFT2

model parameter N_{crit} is accepted as a direct input. Grids for the three-dimensional geometries were generated by members of the ULI at the University of Tennessee at Knoxville using the Pointwise software.

A patch- and box-based modeling specification capability was implemented by Zhi Yang into NSU3D [18]. This allows the selected free transition model or turbulence model to be applied to the surface of the aircraft based on patch identifiers and a distance value, or to regions of the domain bounded by specified points. These implementations can both overlap and override each other through a priority number. Figure 2.2 visually details this capability through an example where the first 3% chord is intended to be modeled as free transition and the remaining chord length is fully turbulent.

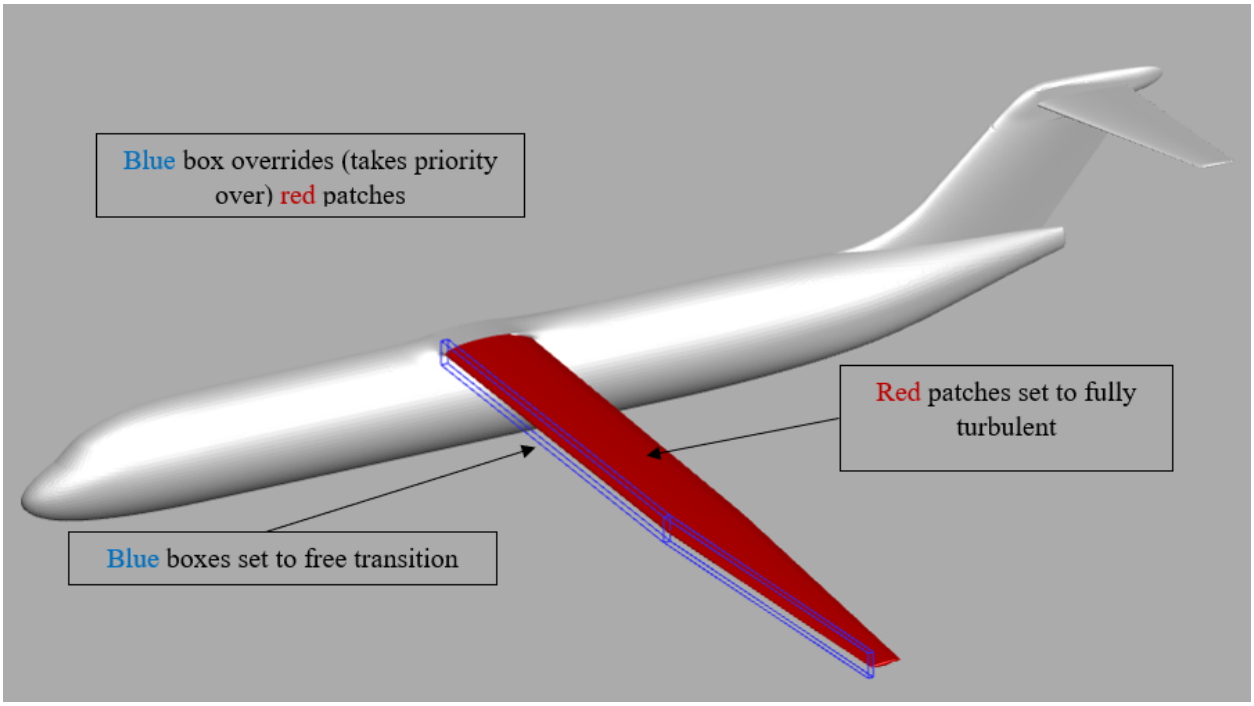

Figure 2.2: Patch- & Box-Based Modeling Implementation Example: Free Transition Up to 3% Chord

2.4 Validation Efforts

Validation of the transition prediction implementations associated with NSU2D and NSU3D, as well as the application of an optimization framework to SNLF technology, was

conducted under the ULI [33]. Results from the free transition validation efforts are reproduced herein. The NSU2D AFT2 model was validated through study of the S204 SNLF airfoil. The low-drag bucket for this SNLF airfoil is bounded by C_L values of approximately 0.2 and 0.4, with slight variations for different Reynolds numbers [13]. Figure 2.3a illustrates the NSU2D results computed with and without the use of the AFT2 model compared to the design polar for a Mach number of 0.5 and Reynolds number of 12x10^6. A freestream turbulence value of 0.07%, which corresponds to an N_{crit} value of 9.0, was used in the case of free transition, and these results show close agreement with reference data [13]. Furthermore, adequate capture of the low-drag bucket is achieved. A contour plot of eddy viscosity for the free transition solution is included as Figure 2.3b and suggests that laminar flow is maintained for a large percentage of the chord length.

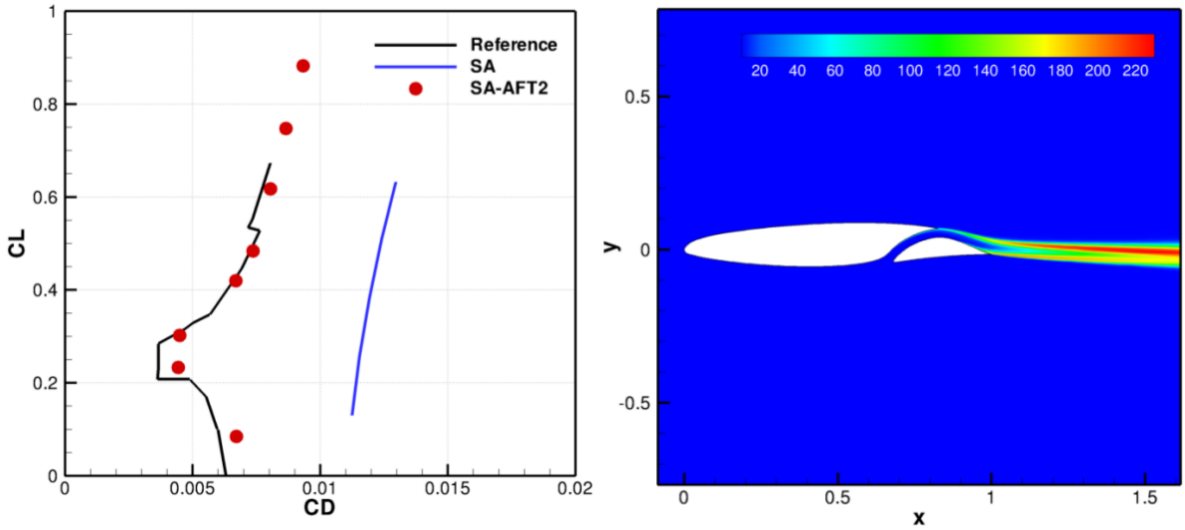

(a) Comparison to Reference [13]

(b) Eddy Viscosity for AOA = 0°

Figure 2.3: NSU2D Results for the S204 Airfoil at Mach = 0.5, Re = 12.0x10^6, Tu_∞ = 0.07%

The TU Braunschweig sickle wing transition experiment was selected for testing the performance of the NSU3D free transition modeling capabilities [33]. Results using both the Menter and AFT2 models were compared to data associated with the original experiment [34] and a solution acquired using OVERFLOW [23], a RANS solver that operates on overset structured grids, for an angle of attack of -2.6° and a Reynolds number of 2.5 Million. Figure 2.4 illustrates this comparison for the upper surface of the wing. Figure 2.5 does the same

for the lower surface. Overall, transition locations on the upper surface predicted by NSU3D using both the Menter and AFT2 models agree qualitatively with those presented in reference [23]. Lower surface transition locations do appear to be predicted slightly downstream with NSU3D, but within acceptable margins.

NSU3D has been utilized for problems associated with SNLF TTBW configurations as well, as results for a notional S204-based three-dimensional TTBW configuration with free transition are presented in reference [33]. This analysis included the effects of coupled aero-structural displacements [35], and a subsequent twist distribution optimization was performed. However, optimization and aero-structural analysis were not exercised in the current work for the S207-based SNLF TTBW configuration. It should be noted that the notional character of the S204-based TTBW configuration precluded the availability of preexisting computational or experimental data for validation purposes.

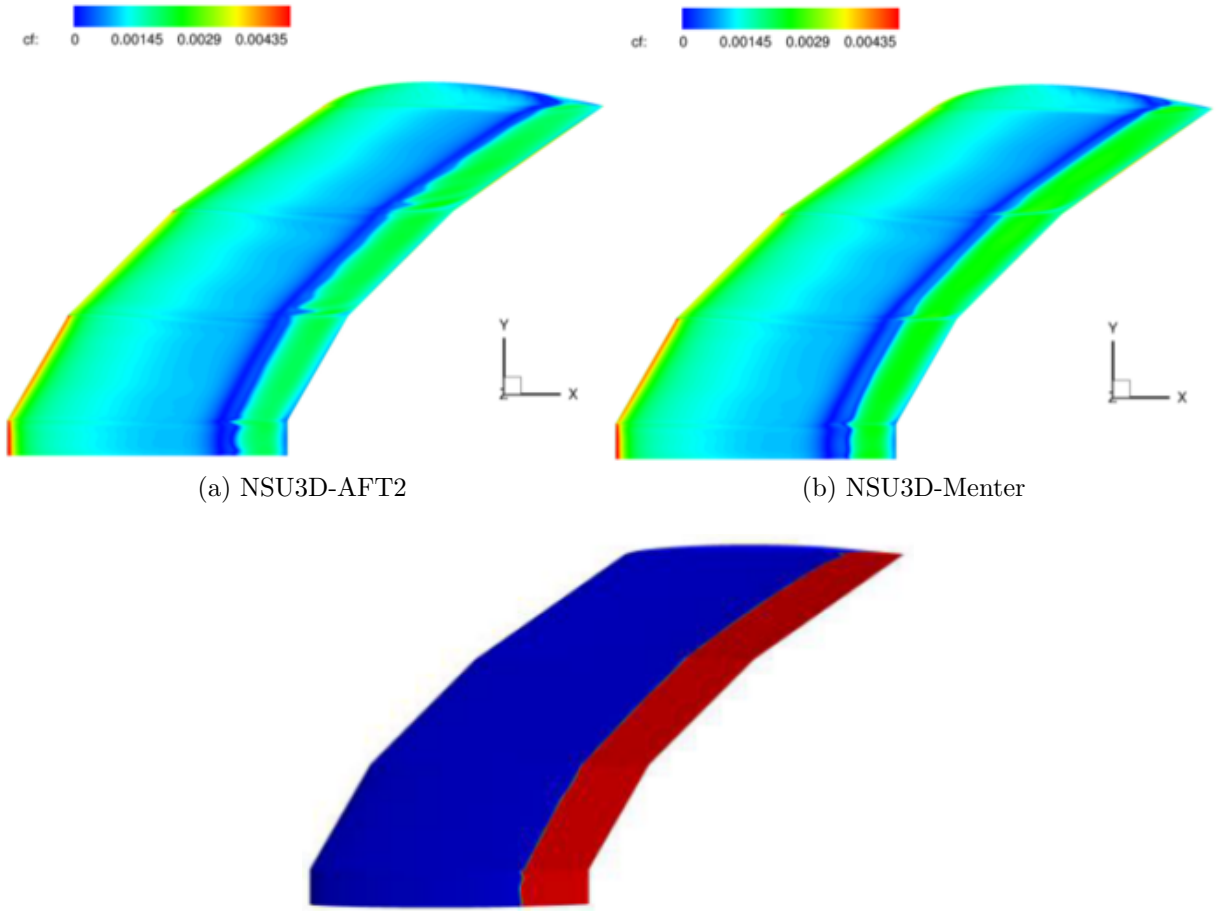

(a) NSU3D-AFT2

(b) NSU3D-Menter

(c) OVERFLOW-AFT2

Figure 2.4: Upper Surface Transition Location Comparison for AOA=-2.6° and Re=2.5x10^6: NSU3D vs. OVERFLOW

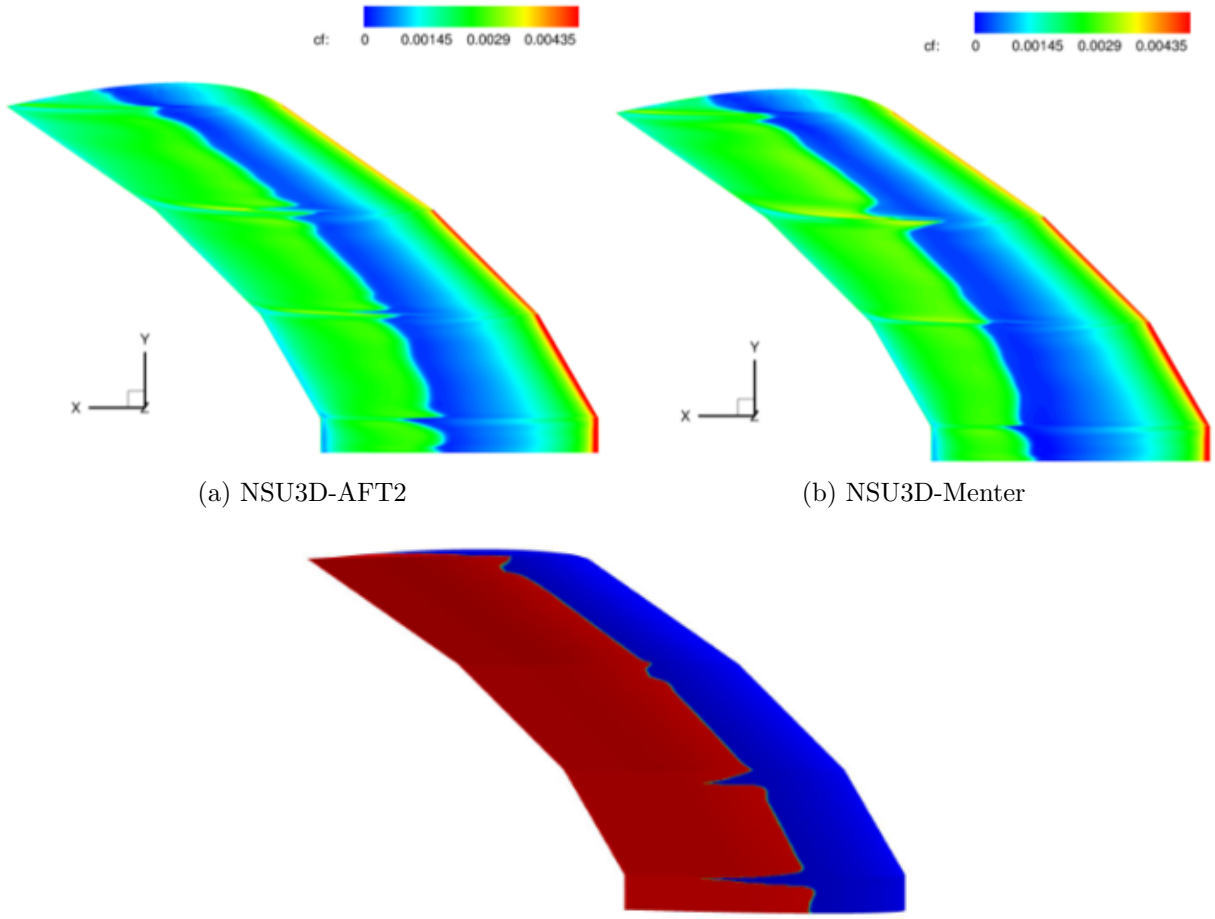

(a) NSU3D-AFT2

(b) NSU3D-Menter

(c) OVERFLOW-AFT2

Figure 2.5: Lower Surface Transition Location Comparison for AOA=-2.6° and Re=2.5x10^6: NSU3D vs. OVERFLOW

Chapter 3

Two Dimensional Analysis of the S207 SNLF Airfoil

3.1 Computational Mesh for the S207 Airfoil Analysis

A two-dimensional unstructured mesh was generated for the S207 SNLF airfoil using the UMESH2D software, which is part of the NSU2D CFD package. The mesh consists of 689326 triangular cells in total. Images of the mesh are included in Figure 3.1. The far-field boundaries are located at a distance of 1000 chord lengths in each cardinal direction. Both the fore and aft elements have 2000 surface points. Streamwise spacing at the leading and trailing edges of each element was set to 0.02% the chord length, and the normal wall-spacing for both elements was set to 10^{-6} chord lengths. The growth rate of the cells nearest the airfoil body was set to 1.1 in order to capture the expected thin laminar boundary layer.

3.2 Simulations at Cruise

Nominal angles of attack for the S207 SNLF airfoil are predominantly negative [10]. An attempt to establish correspondence between an NSU2D solution and original design computational results was made for a Mach number of 0.700, a Reynolds number of 13.2 million, and an angle of attack of -1.3°. Four simulations were performed: one that employed

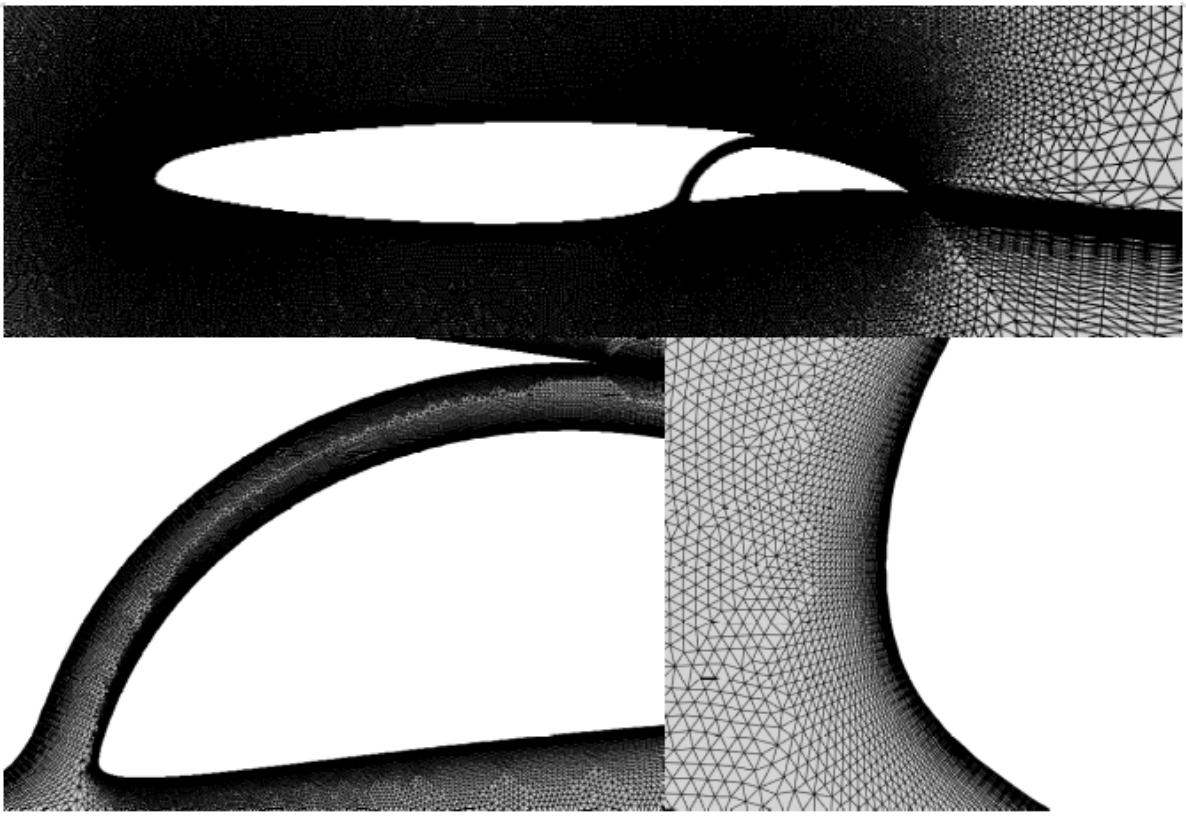

Figure 3.1: 2D Grid for the S207 SNLF Airfoil

strictly fully turbulent modeling through use of the SA turbulence model, which is denoted as Run 0, and three others that considered the impact of free transition through a coupled SA-AFT2 approach. These simulations are denoted as Run 1, Run 2, and Run 3. Runs 1 and 2 were both restarted from a fully turbulent simulation that was run for 100 cycles, denoted Run A. This was done due to difficulties in preventing numerical divergence when the solution was started from freestream values. Runs 1 and 2 utilized different freestream turbulence intensity values to explore the impact this parameter had on the transition line. Run 1 used a freestream turbulence intensity of 0.001% (N_{crit}=19.2), and Run 2 used a more realistic value of 0.07% (N_{crit}=9.0). For both of these simulations the transition prediction model was frozen after 3250 cycles to prevent residual stagnation and to replicate the convergence methodology utilized for a notional SNLF-based vehicle conducted previously under the ULI [33]. Run 3 used Run 2 as its initial condition and kept the same freestream turbulence intensity value of 0.07%. The transition equations were unfrozen for the first 2000 cycles to determine if the transition line would change if the initial condition was already sufficiently converged to a steady-state solution. A more precise summary of the cases is included as Table 3.1. Additionally, the convergence histories for the density residuals and lift coefficient values for each simulation are included in Figure 3.2. Difficulty in establishing a steady decrease in the density residual is observed for free transitional simulations prior to the freeze of the transition prediction equations. However, once the freeze has been invoked, a steady decrease in the density residual can be maintained.

Table 3.1: NSU2D S207 Airfoil Simulation Summary at Mach = 0.7, Re=13.2x10^6, and AOA=-1.3°

Simulation	Modeling	Cycles	Tu_∞	Trans. Freeze	Initial Condition
Run A	SA	100	NA	NA	Freestream
Run 0	SA	10000	NA	NA	Freestream
Run 1	SA-AFT2	10000	0.001%	3250	Run A
Run 2	SA-AFT2	20000	0.07%	3250	Run A
Run 3	SA-AFT2	10000	0.07%	2000	Run 2

Table 3.2 details the exact force coefficient values associated with each of these cruise simulations, and Figure 3.3 illustrates the comparison of these force coefficient values to the

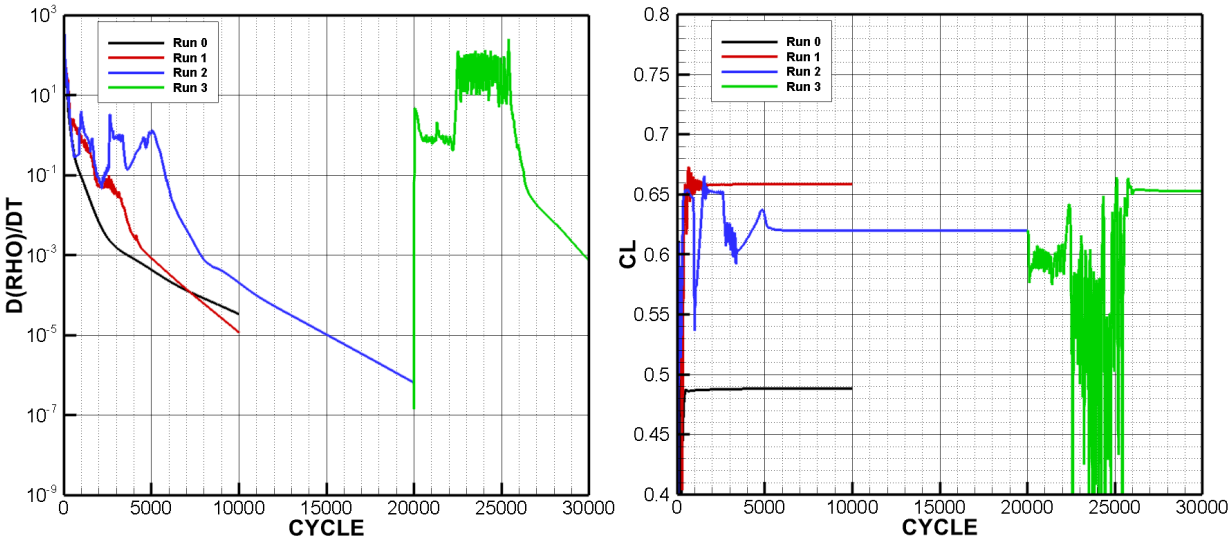

(a) Density Residual Convergence History

(b) Lift Coefficient Convergence History

Figure 3.2: NSU2D S207 Airfoil Simulation Histories for = 0.7, Re = 13.2x10^6, AOA = -1.3°

original drag polar produced using MSES, a two-dimensional solver that solves the Euler equations with interactive boundary layer for single and multi-element airfoils [36], in the design of the S207 airfoil in reference [10]. Drag coefficient values in the vicinity of the low-drag bucket for these flow conditions were predicted to be between 27 and 29 counts. NSU2D predicts 32 to 39 counts when using free transition with corresponding C_L values of 0.620 to 0.658. These lift coefficient values are slightly lower than the upper limit of the low-drag bucket. A note should be made upon examination of this data. The magnitude of the discrepancy between the NSU2D solution found using strictly fully turbulent modeling and the solutions using free transition is quite large. The drag computed for the fully turbulent simulation using the SA turbulence model alone is much higher at 117.7 counts, and the computed C_L is lower at 0.488. This is a strong indication of the benefits of laminar flow.

Table 3.2: NSU2D Cruise Simulations Summary

Simulation	C_L	C_D
Run 0	0.488	0.0117
Run 1	0.658	0.0032
Run 2	0.620	0.0035
Run 3	0.652	0.0039

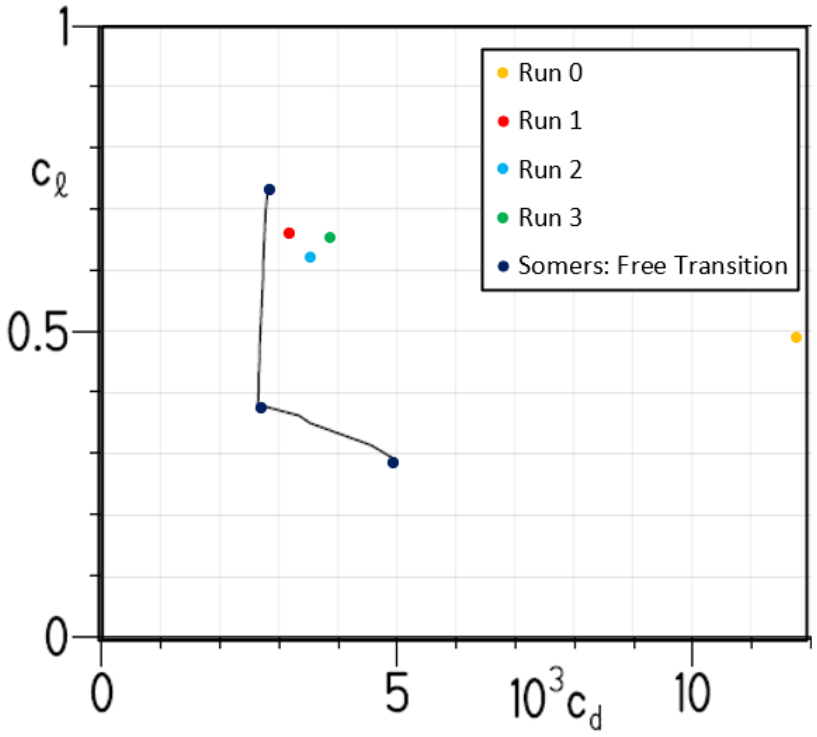

Figure 3.3: NSU2D Results Compared to Original Design Data [8] for Mach = 0.7, Re = 13.2x10^6, AOA = -1.3°

By design, the S207 SNLF airfoil should only have turbulent flow on the upper surface of the aft element [10]. Figure 3.4 illustrates the solution flow fields of Run 1, Run 2, and Run 3 quantified with eddy viscosity for the entire S207 airfoil geometry, and with Mach number for the aft element. It is evident from these images that appreciable runs of laminar flow are maintained as well as a smooth velocity profile through the slot. There appears to be no formation of a strong shock wave or other discontinuity that could destabilize the boundary layer as the flow accelerates through the slot. Differences in these free transition solutions is minimal despite the variations in freestream turbulence intensity and duration of transition prediction application. Run 2 and Run 3 predict a wider region of supersonic flow through the exit of the slot compared to Run 1, and Run 3 predicts the region of supersonic flow on the upper surface of the aft element near the entrance of the slot to be thinner. Additionally, Run 3 shows that the velocity gradient on the upper surface of the aft element downstream of the slot exit is steeper than what is shown in Runs 1 and 2.

The location of transition computed by the transition prediction model can be deter-

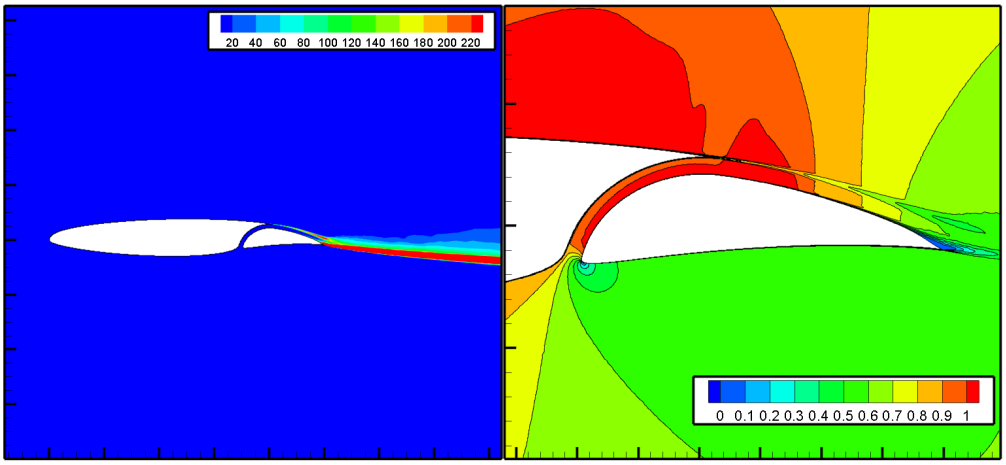

(a) Run 1 Eddy Viscosity (b) Run 1 Slot Mach Number

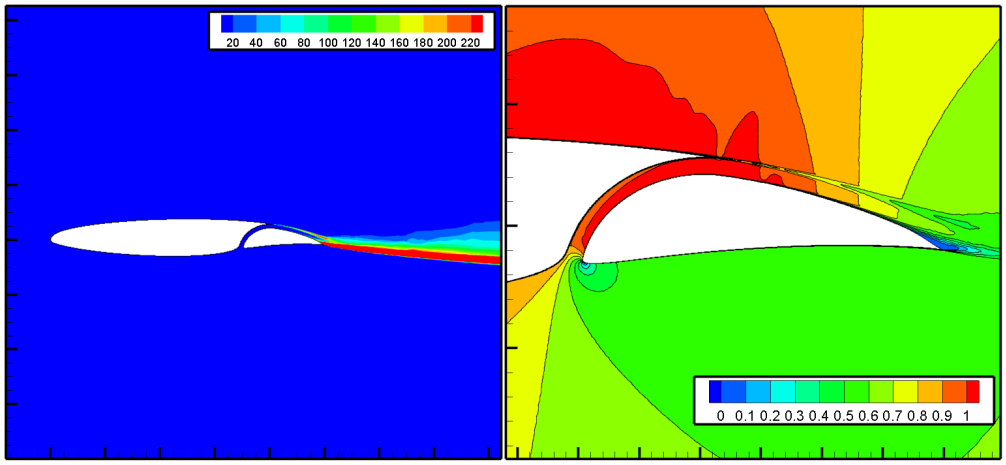

(c) Run 2 Eddy Viscosity (d) Run 2 Slot Mach Number

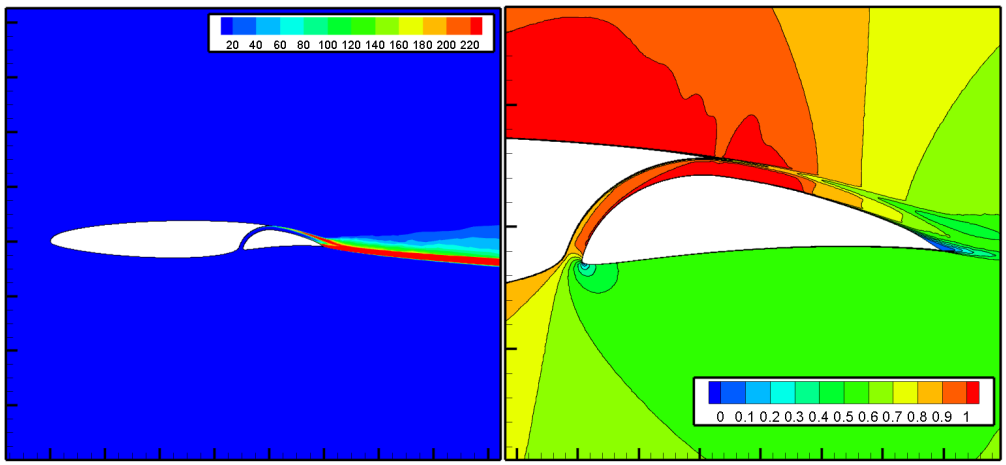

(e) Run 3 Eddy Viscosity (f) Run 3 Slot Mach Number

Figure 3.4: NSU2D-SA-AFT2 Free Transition Flow Field Solutions at Mach = 0.7, Re = 13.2x10^6, AOA = -1.3°

mined upon examination of the surface skin friction drag coefficient. This value is illustrated for the fore element in Figure 3.5a for Run 1, Run 2, and Run 3. The same is done for the aft element in Figure 3.5b. Note that in both the cases of the fore and aft element, negative skin friction drag is plotted on the lower surface by convention. Run 2 predicts transition to occur on the upper surface of the aft element at approximately 84% the chord length where a large spike in the skin friction drag coefficient profile is observed. By the same token, Runs 1 and 3 closely agree, predicting transition to occur at roughly 88% the chord length on the upper surface of the aft element. Note that there exists another large spike in skin friction drag at the leading-edge of the aft element for all cases. This is an artifact of leading-edge stagnation flow. In the cases of Run 1, Run 2, and Run 3, the predicted transition location on the aft element is in alignment with S207 airfoil design intent, as turbulent flow is only expected on the upper surface of the aft element near the trailing-edge [10]. Interestingly, the transition line on the aft element for Run 3 moved downstream given that its initial condition was Run 2, which had a more upstream transition line. However, Run 3 also predicts transition on the fore element in the region of the slot, whereas both Runs 1 and 2 predict laminar flow on the entirety of the fore element. This deviation in Run 3 is not in alignment with performance metrics. Finally, the skin friction on the upper surface of the fore element near the trailing-edge becomes negative in all cases, indicating a laminar separation bubble. This phenomenon is also observed in original design runs [10].

In summary, results for simulations of the S207 SNLF airfoil in two dimensions at cruise conditions using a transition prediction model align well with design intent set forth in the original S207 airfoil report. Across three cases, each with differing model specifics in freestream turbulence intensity and evolution of the transition equations, predicted drag coefficient values lie within proximity of the low-drag bucket. Additionally, lift coefficient values were slightly lower than the upper limit of the low-drag bucket for the S207 airfoil. Investigation of eddy viscosity and Mach number quantities across the flow field, particularly through the slot, determined that discontinuities such as shock waves are not present to disrupt stability in the boundary layer. However, examination of the skin friction profile drag indicates issues with the transition prediction model, as discrepancies between Runs 1, 2, and

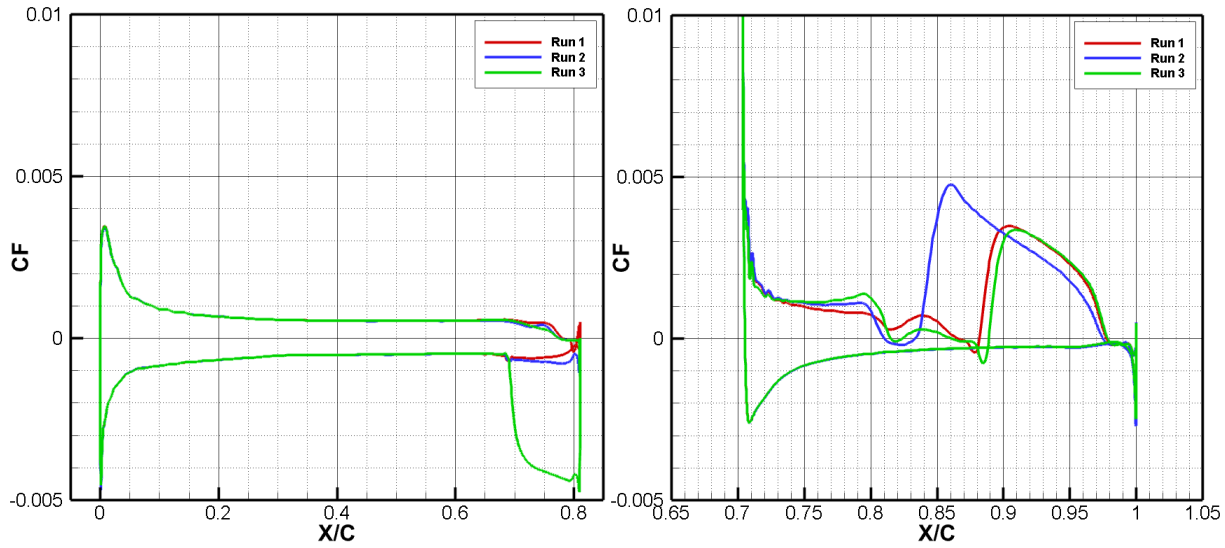

(a) Fore Element (b) Aft Element

Figure 3.5: NSU2D-SA-AFT2 Free Transition Skin Friction Drag Solutions at Mach = 0.7, Re = 13.2x10^6, AOA = -1.3°, with Negative Skin Friction Drag Plotted for Lower Surfaces and a Freeze of the Transition Prediction Equations at 3250 Cycles

3 were observed. Namely, Run 3, which used the final solution of Run 2 as its initial condition and allowed the transition equations to evolve for its first 2000 cycles, predicted transition on the lower surface of the fore element in the region of the slot. This is in disagreement with the other CFD solutions and design intent, indicating that accurate solutions may be dependent on the duration in which the transition equations are allowed to evolve. The difficulty in establishing a consistent decrease in the solution residuals while transition is unfrozen also adds uncertainty to the accuracy of the predicted transition location on the fore element in the final solution of Run 3.

3.3 Additional 2D Free Transition Investigation

Additional study of the behavior of the transition line on the two-dimensional S207 airfoil geometry was encouraged by a slow transient observed on an S207-based wind tunnel model, and in part by results from Run 3 in the previous section. This wind tunnel model simulation, which is more extensively described in Section 5.4, saw mostly laminar flow initially. However, as the simulation evolved, more turbulent flow was observed in the skin

friction drag contours as the transition line moved slowly forward from the trailing-edge to the leading-edge. This simulation did not employ a freeze of the transition prediction model, so this approach was used in two dimensions to determine if the the slow transient was not unique to the wind tunnel model. Namely, Run 2 from the previous section was rerun without invoking the freeze of the transition prediction equations. Figure 3.6 shows the skin friction drag coefficient for this simulation whose flow conditions were a Mach number of 0.7, a Reynolds number of 13.2 million, and an angle of attack -1.3°. It should be additionally noted that this simulation was run for 15000 cycles to ensure a stationary or near stationary transition line. Though the transition location on the aft element sees relatively no change in comparison to when the transition freeze was invoked, these results show that transition is predicted on both the upper and lower surfaces of the fore element. This is in disagreement with the design intent of this airfoil as the fore element should only see laminar flow [10]. Additionally, comparing Figure 3.5 to Figure 3.6, it can be concluded that there is indeed a transient present in the two-dimensional results that slowly pushes the transition line forward on the upper surface of the aft element, as well as the upper and lower surfaces of the fore element.

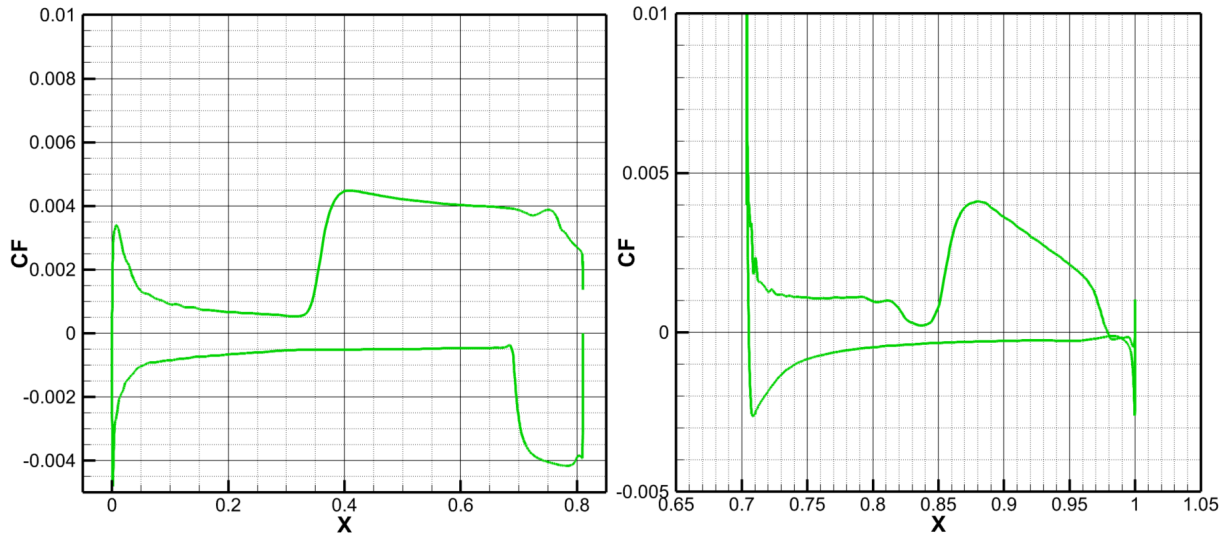

(a) Fore Element

(b) Aft Element

Figure 3.6: NSU2D-SA-AFT2 Free Transition Skin Friction Drag Solutions at Mach = 0.7, Re = 13.2x10^6, AOA = -1.3°in the Case of no Transition Freeze After 15,000 cycles with Negative Skin Friction Drag Plotted for Lower Surfaces

Evidence suggests that the two-dimensional behavior of the S207 airfoil may not be in as close alignment with performance intent as originally thought given the discrepancies between solutions acquired with and without the freeze of the transition prediction equations. In an attempt to establish closer correspondence between NSU2D and MSES results presented in the original report [10] without the use of the transition model freeze, several performance polars were developed for the S207 airfoil for Mach numbers of 0.7 and 0.65, a Reynolds Number of 13.2 Million, and varying values of freestream turbulence intensity. Once again, simulations were run for 15000 cycles to ensure a stationary or near stationary transition line. Results are shown in Figure 3.7 and indicate that freestream turbulence intensity values of 0.02% (N_{crit}=12.0) to 0.04% (N_{crit}=10.34) most closely agree with MSES data presented in reference [10], which used a freestream turbulence intensity value of 0.07% (N_{crit}=9.0).

Though more success was found in creating closer agreement between MSES and NSU2D results without a freeze of the transition prediction model through a reduction in freestream turbulence intensity, the difference in freestream turbulence intensities used for MSES and NSU2D simulations that most closely agree is cause for concern. In other words, the need to reduce the NSU2D freestream turbulence value to 0.04% to align with MSES results that used a freestream turbulence intensity of 0.07% indicates that the NSU2D-AFT2 transition prediction implementation may need to be revisited. Additionally, these issues were not encountered with study of the S204 SNLF airfoil [33], suggesting that the behavior of the transition prediction model under more adverse flow characteristics, such as those associated with the S207 airfoil, is worth investigation. The transition prediction model is, however, including all the expected trends in transition location with angle of attack and freestream turbulence values.

3.4 Sensitivity of Performance to Flap Position

The performance of an SNLF airfoil is known to be particularly sensitive to geometric changes, especially at the slot. A sensitivity study of the performance of the S207 airfoil to flap position was undertaken as part of this work. This was motivated in part by the

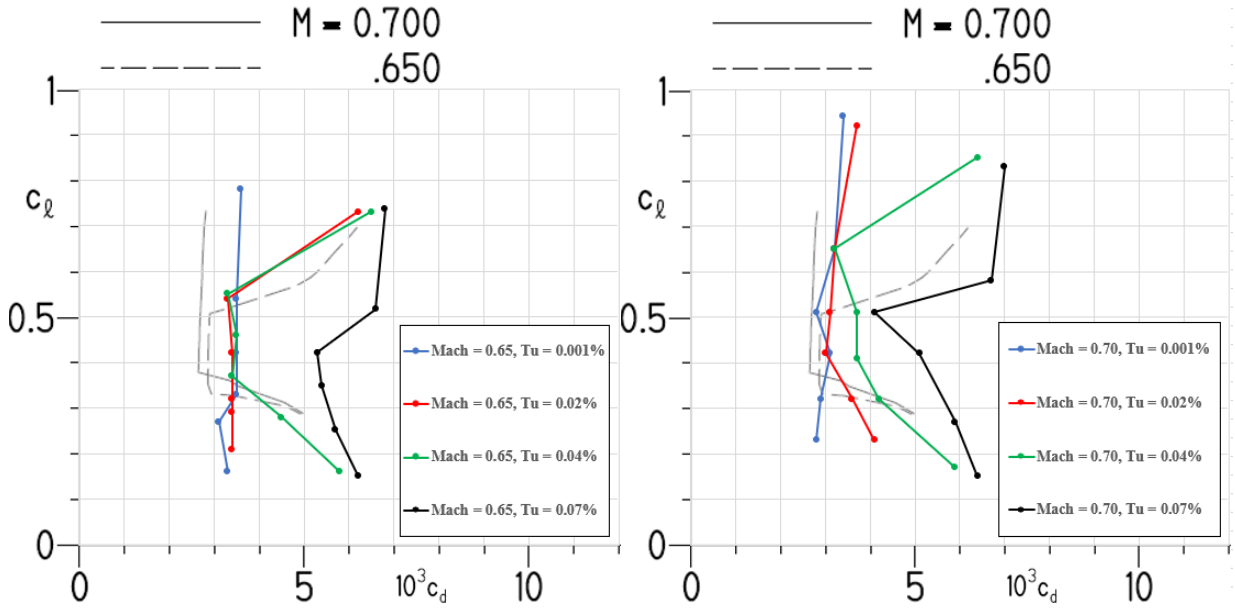

(a) Mach = 0.650 (b) Mach = 0.700

Figure 3.7: NSU2D-SA-AFT2 Performance Polars for Re = 13.2x10^6 and Varying Freestream Turbulence Intensities

formation of a shock in the slot region encountered in the three-dimensional analysis, as will be described further in Chapter 4. This issue was present in both fully turbulent and free transition solutions, so the decision was made to conduct this study using exclusively fully turbulent modeling. This approach offers quick insight to issues originating from small flow and geometric variations without the convergence difficulties and expenditures that accompany free transition simulations, which are much more significant in the presence of adverse flow characteristics. This would have presented a possibly prohibitive obstacle in the case of the more extreme flap settings. Additionally, there is an interest in comparing these sensitivities to expected structural displacements under aerodynamic loading and manufacturing tolerances.

Several solutions at a Mach number of 0.7, a Reynolds number of 13.2 million, and an angle of attack of -1.3° were obtained. A different flap position defined by a unique horizontal, vertical, or diagonal displacement was used for each simulation. In all cases, a nearly identical mesh was used based on the parametric multi-element positioning capabilities built into the UMESH2D grid generation code. A summary quantifying the flap displacements for each

solution is provided in Table 3.3. Figure 3.8 illustrates the computed flow field for each case shown as local Mach number contours. From these results it can be stated that narrowing the slot horizontally results in the formation of a shock near the exit. On the contrary, vertically translating the aft element further from the fore element predicts a shock wave near the entrance of the slot. With diagonal narrowing, again a shock wave is formed near the exit of the slot. The shock wave formation in these cases is accompanied by severe flow separation on the upper surface of the aft element due to the total pressure loss that occurs through the shock wave. Vertically wide variations with no predicted shock wave produce flow separation on the concave portion of the fore element. Unsurprisingly, extreme changes in the geometry of the slot and the consequential flow behavior leads to undesirable increases in drag and reductions in lift as shown in Figure 3.9. These values are tabulated in Table 3.4.

It can be conclusively stated from these results that the performance of the S207 airfoil is highly sensitive to changes in the geometry of the slot. Though there appears to be a slight benefit with smaller horizontal and diagonal widening of the slot, it is important to note that results were only obtained for one specific set of flow parameters and performance improvements may not carry over to other flow conditions within the desired operating range of the S207 airfoil. The flap position sensitivity study indicates that to avoid compromising the desired capabilities of the airfoil, the flap positioning should deviate no more than 0.1% chord from its nominal design position. These values are well above manufacturing tolerances. Additionally, preliminary structural results for the S207 wing box under gravity loads predict displacements that are well below these limits [37]. These results indicate that the S207 airfoil should be able to maintain design metrics since the aerodynamic sensitivity is not large enough to compromise performance in practice due to manufacturing variabilities or aeroelastic deformations.

Table 3.3: Slot Sensitivity Study: Displacement Summary

Trans. Direction	Case Number	Trans. Magnitude
Horizontal	1a	-0.0055
	2a	-0.0050
	3a	-0.0025
	Baseline	0.0000
	5a	0.0025
	6a	0.0050
	7a	0.0100
	8a	0.0200
Vertical	1b	-0.0055
	2b	-0.0050
	3b	-0.0025
	Baseline	0.0000
	5b	0.0025
	6b	0.0050
	7b	0.0100
	8b	0.0200
Diagonal	1c	-0.0071
	2c	-0.0035
	Baseline	0.0000
	4c	0.0035
	5c	0.0071
	6c	0.0141
	7c	0.0283

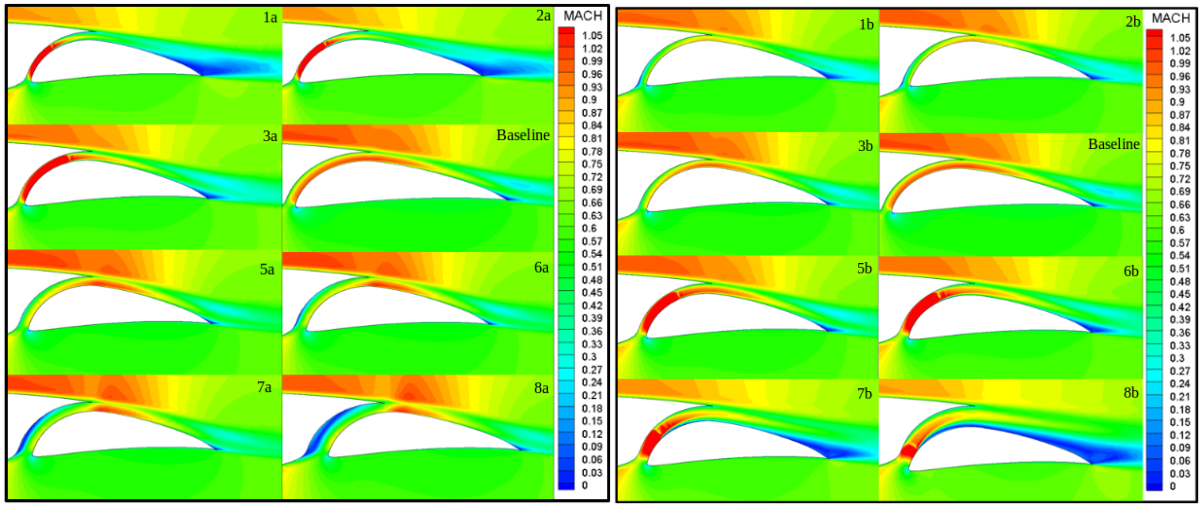

(a) Horizontal

(b) Vertical

(c) Diagonal

Figure 3.8: NSU2D-SA Fully Turbulent Flow Field Solutions Quantified with Mach Number for Varying Flap Perturbations for Mach = 0.7, Re = 13.2x10^6, AOA = -1.3°

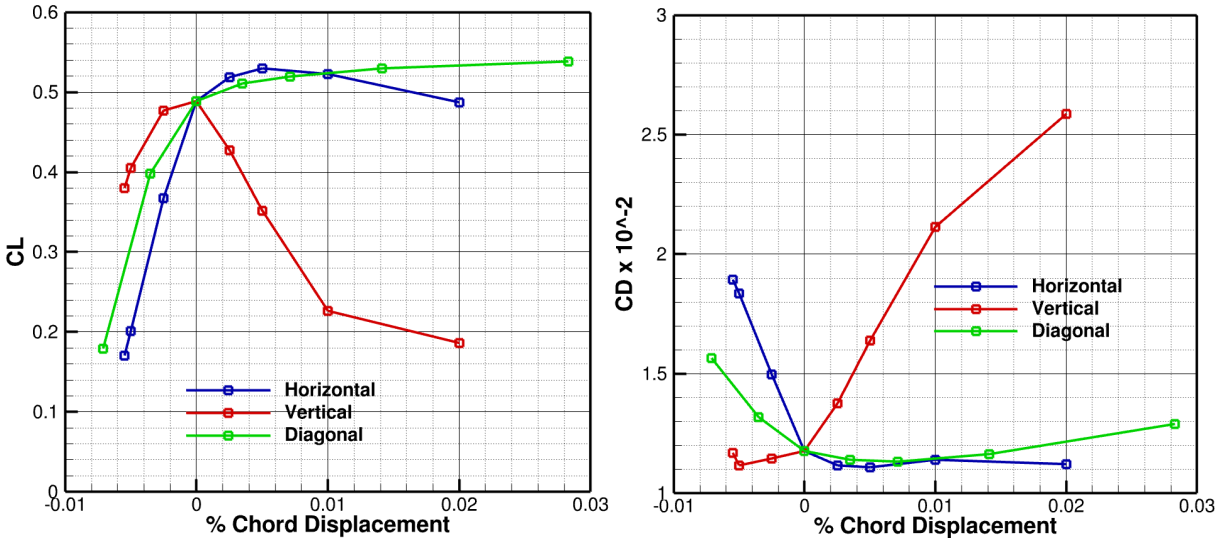

(a) Lift Coefficient

(b) Drag Coefficient

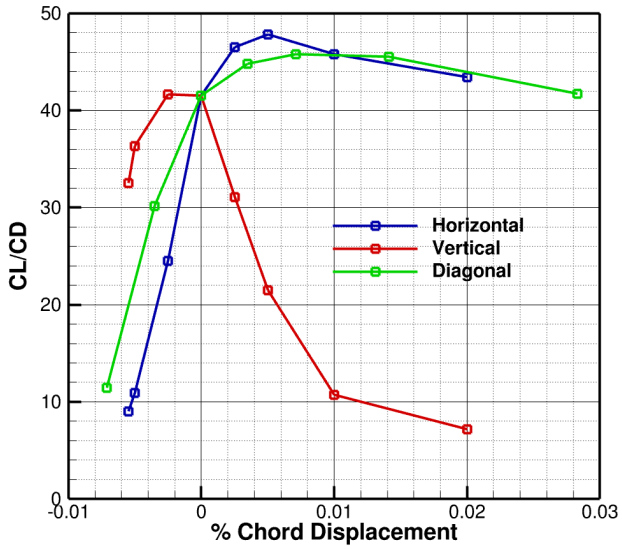

(c) Lift over Drag

Figure 3.9: NSU2D-SA Fully Turbulent Force Coefficients Computed for Varying Flap Perturbations for Mach = 0.7, Re = 13.2x10^6, AOA = -1.3°

Table 3.4: Slot Sensitivity Study: Computed Force Coefficient Summary

Trans. Direction	Case Number	CL	CDx10^{-2}	CL/CD
Horizontal	1a	0.1704	1.8937	8.998
	2a	0.2007	1.8346	10.940
	3a	0.3671	1.4973	24.517
	Baseline	0.4885	1.1770	41.504
	5a	0.5187	1.1154	46.503
	6a	0.5299	1.1076	47.842
	7a	0.5225	1.1408	45.801
	8a	0.4867	1.1218	43.386
Vertical	1b	0.3800	1.1697	32.487
	2b	0.4055	1.1158	36.342
	3b	0.4767	1.1456	41.611
	Baseline	0.4885	1.1770	41.504
	5b	0.4269	1.3753	31.041
	6b	0.3514	1.638	21.453
	7b	0.2266	2.114	10.719
	8b	0.1858	2.5869	7.182
Diagonal	1c	0.1788	1.5642	11.431
	2c	0.3979	1.3193	30.160
	Baseline	0.4885	1.1770	41.504
	4c	0.5105	1.1400	44.781
	5c	0.5190	1.1330	45.808
	6c	0.5294	1.1636	45.497
	7c	0.5380	1.2907	41.683

3.5 Results for Morphed Leading-Edge Variants

Additional efforts under the ULI project have sought to increase performance and reduce stall characteristics under circumstances where the angle of attack is high, such as during landing or takeoff. Exploration into adjusting flap configuration to increase lift and extend the bounds of the design envelop have already been conducted by ULI contributors at the University of Illinois at Urbana-Champaign and the University of Tennessee at Knoxville. Variation in the position of the flap of the S414 SNLF airfoil, designed for rotorcraft applications, offered evidence that a low-pressure region can be imposed on the upper surface of the aft element if the dumping velocity is targeted as the mechanism for improved lift [38]. Study of a business-jet SNLF airfoil concluded that maintaining a constant slot width is most advantageous to efficiency at angles of attack near maximum lift [39]. Investigation of high-lift approaches in the context of the S207 airfoil has extended into the realm of drooped and morphed leading-edges. Unlike a slat used in a high-lift system, which introduces a step in the airfoil geometry when stowed during cruise and causes transition, drooped and morphed leading edges seek to alleviate stall characteristics through a smooth, continuous reshaping of the leading-edge. They offer compatibility with natural-laminar-flow as they do not introduce gaps and steps or other geometric features that may induce turbulence [40].

Collaborators at the University of Illinois at Urbana-Champaign designed a genetic algorithm used to develop a library of possible morphed leading-edge variations of the S207 SNLF airfoil [41]. Ten different cost functions were used to guide the optimization process based on lift coefficient and boundary layer shape factor. This led to the fabrication of geometries that both increased lift and drove the instance of flow separation more toward the trailing-edge of the airfoil. These variations were computationally analyzed using the MSES code at the University of Illinois at Urbana-Champaign. Results proved that the generated geometries are viable for intended design application. Wind tunnel tests in the Illinois low-speed, low-turbulence wind tunnel further support this claim, with the angle of attack at which stall occurs and lift coefficient increase due to use of a morphed leading-edge agreeing with MSES results [42].

Research support was provided to the efforts made at the University of Illinois for three

candidate morphed leading-edge derivatives of the S207 airfoil. They are denoted the 503, 511, and A00. Geometric comparisons of these airfoils to the baseline S207 SNLF airfoil are included in Figure 3.10. Simulations of these high-lift configurations were conducted using fully turbulent modeling in both NSU2D and MSES. Grids fabricated for use in NSU2D were held identical to the original S207 airfoil mesh with the only change being an increase in fore element surface points to accommodate the change in leading-edge shape. It is worth noting that the genetic algorithm optimization maintained a constant leading-edge arc length between variants [41]. This change in surface points resulted in a cell number that landed between 770000 and 780000 for each grid. A Mach number of 0.225 and a Reynolds number of 16 million were used as they are representative of high-lift flight conditions for a commercial transport aircraft. Figure 3.11 details NSU2D performance results for the 503, 511, A00 and baseline shape. Unsurprisingly, the addition of the morphed leading-edge increases both the lift coefficient and the angle of attack at which stall occurs. Comparison of results to MSES data is shown in Figure 3.12. NSU2D predicts a higher lift coefficient in all cases. This behavior was unexpected as MSES has been shown to often overpredict lift for high-lift, multi-element configurations [42].

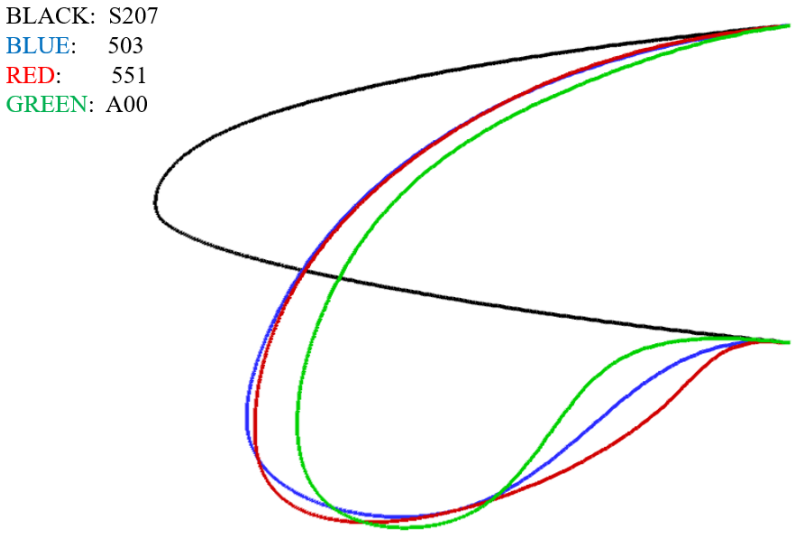

Figure 3.10: Geometric Comparison for Candidate Morphed Leading-Edge Variants of the S207 SNLF Airfoil

Further efforts in establishing correspondence between computational results for the

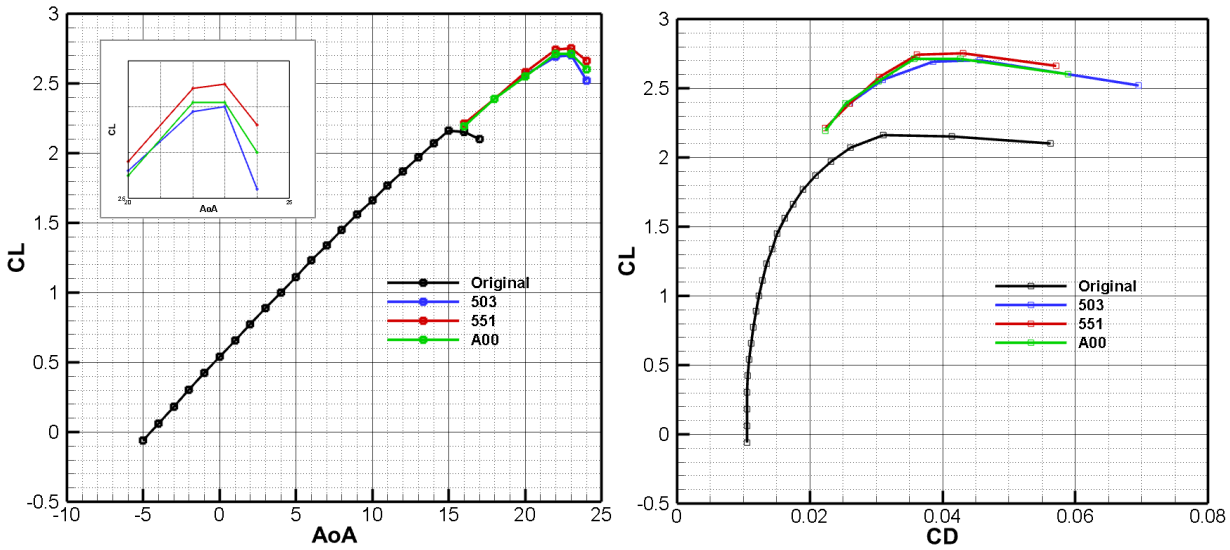

(a) Lift Curves (b) Polar Curves

Figure 3.11: NSU2D-SA Fully Turbulent Results for the 503, 511, and A00 Morphed Leading-Edge Variants at Mach = 0.225 and Re = 16x10^6

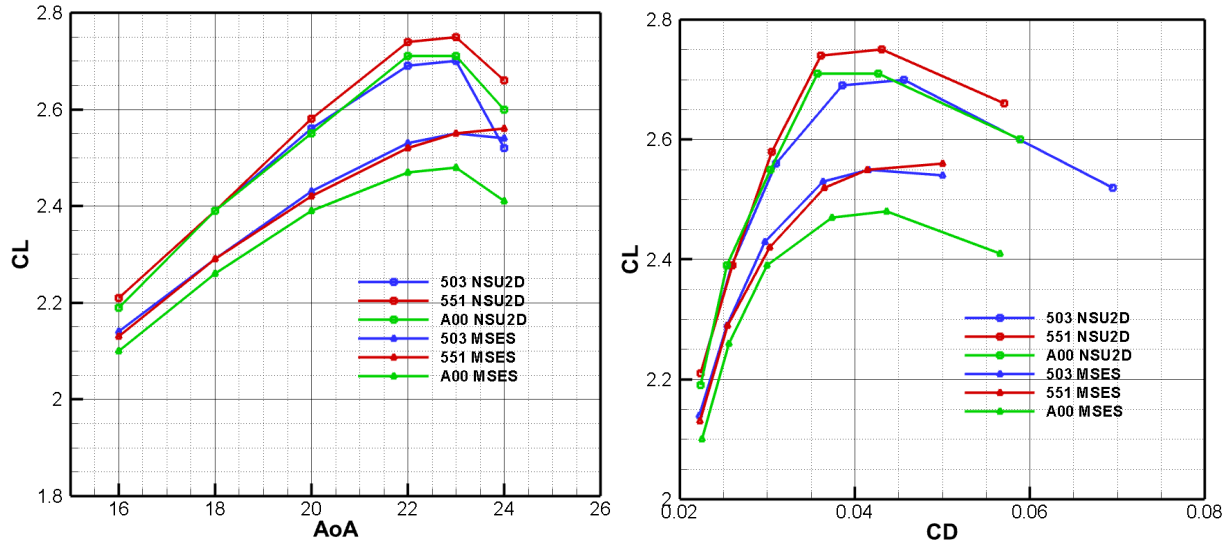

(a) Lift Curves (b) Polar Curves

Figure 3.12: NSU2D-SA Fully Turbulent Results for the 503, 511, and A00 Morphed Leading-Edge Variants Compared to MSES Data Provided by the University of Illinois at Urbana-Champaign for Mach = 0.225 and Re = 16x10^6

morphed leading-edge variants of the S207 were conducted through comparisons between NSU2D and OVERFLOW. Data was provided by collaborators at the University of Tennessee at Knoxville and flow conditions were requested to be set to a Mach number of 0.180 and a Reynolds number of 1.4 million. Figure 3.13 illustrates the lift and drag polar curves computed strictly with NSU2D. Again, the morphed leading-edge variants delay stall and increase lift. Differences in computed lift and drag values between NSU2D and OVERFLOW can be viewed in Figure 3.14. Results are in much closer agreement than the prior comparison with MSES up until stall. However, NSU2D predicts stall to occur earlier than OVERFLOW.

In summary, results for fully turbulent simulations of three morphed leading-edge S207 derivatives in NSU2D support objectives in increasing lift and delaying stall. However, comparison of these results to data acquired using MSES and OVERFLOW suggest further investigation is needed. In both cases NSU2D is in disagreement on the maximum C_L value accomplished through utilization of the morphed leading-edge variants. For a Mach number of 0.225 and a Reynolds number of 16 million, MSES predicts the maximum lift coefficient and stall angle of attack for the A00, 503, and 511 to be approximately 2.56 and 23°, respectively [41]. The stall angle predicted by NSU2D is also approximately equal to 23°. However, NSU2D computes the maximum C_L to be closer to 2.70, as can be concluded from Figure 3.12. This difference in computed lift coefficient values is observed at angles of attack smaller than 23° as well. For a Mach number of 0.180 and a Reynolds number of 1.4 million, OVERFLOW and NSU2D predict C_L values that are approximately equal up until an angle of attack of 20°, as observed in Figure 3.14. NSU2D predicts the occurrence of stall at this angle of attack with the maximum lift coefficient being equal to about 2.35. OVERFLOW computes an increase in lift up until 24°, where the maximum C_L is approximately equal to 2.8. While NSU2D and OVERFLOW are both RANS codes and use the same turbulence model, MSES is an Euler solver with interactive boundary layer. The agreement in C_L values up until stall between NSU2D and OVERFLOW is thus expected, though different stall mechanisms may be being predicted between these two codes at these flow conditions. Additionally, the NSU2D comparisons to MSES and OVERFLOW were run at different flow conditions, making it hard to assess if MSES and OVERFLOW would provide better

agreement if compared. MSES and OVERFLOW solutions were performed externally, and further validation between these three codes was beyond the scope of the project.

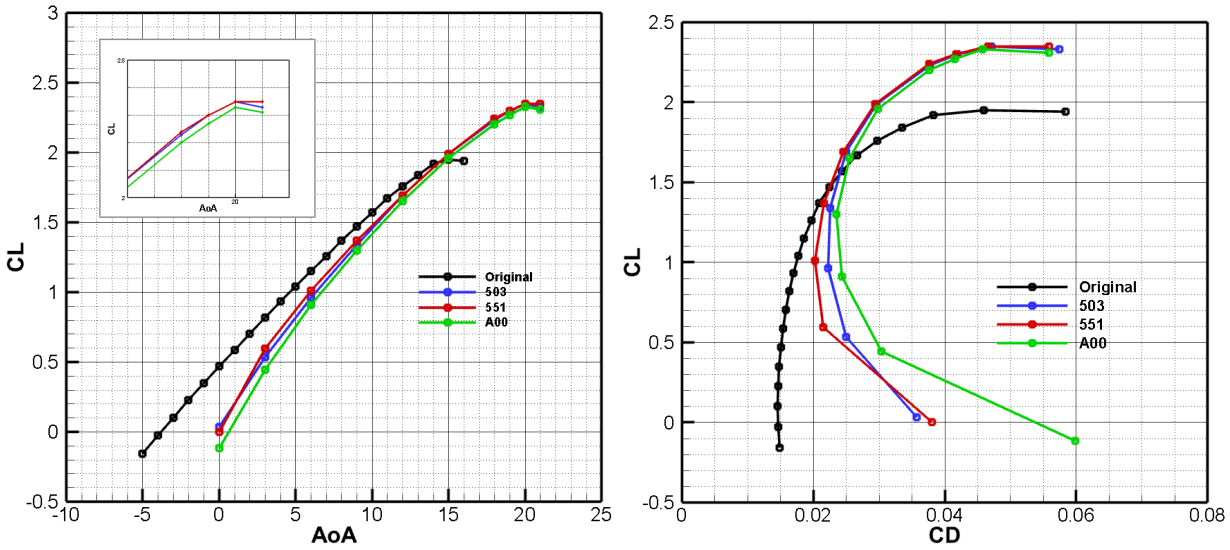

(a) Lift Curves (b) Polar Curves

Figure 3.13: NSU2D-SA Fully Turbulent Results for the 503, 511, and A00 Morphed Leading-Edge Variants at Mach = 0.18 and Re = 1.4x10^6

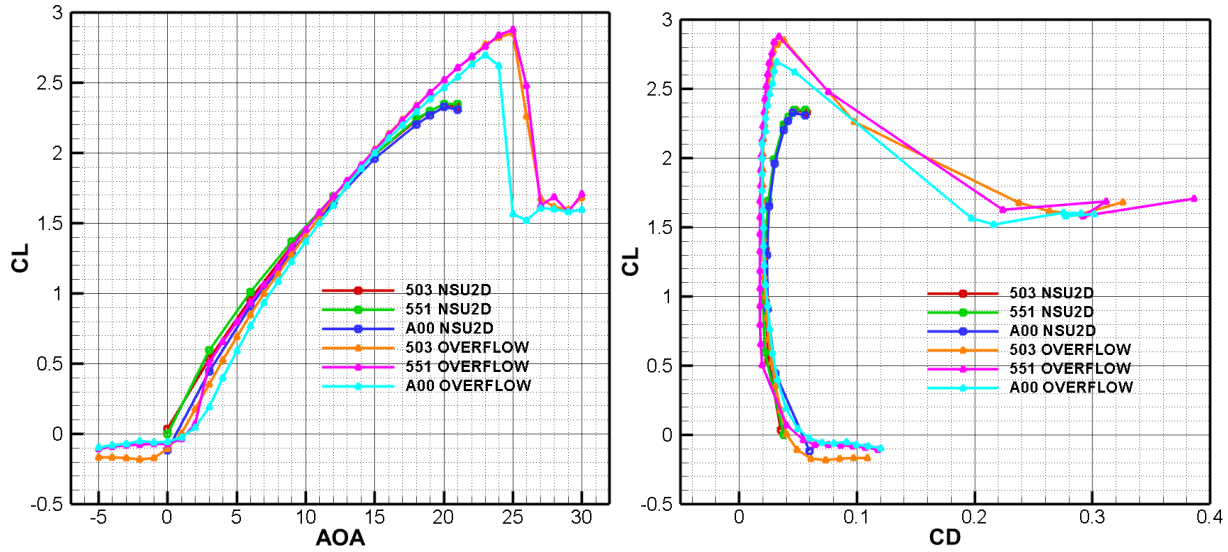

(a) Lift Curves

(b) Polar Curves

Figure 3.14: NSU2D-SA Fully Turbulent Results for the 503, 511, and A00 Morphed Leading-Edge Variants Compared to OVERFLOW Fully Turbulent Data Provided by the University of Tennessee at Knoxville for Mach = 0.18 and Re = 1.4x10^6

Chapter 4

Three-Dimensional Analysis of an S207-Based Vehicle

4.1 The Geometry and Its Evolution

The design of the S207 SNLF TTBW aircraft is based on the 2015 version of the Boeing SUGAR aircraft, which is the baseline comparison for the ULI project [43]. However, the wing was resized from 1477ft^2 to 1350ft^2 to account for the higher maximum lift coefficient of the clean S207 airfoil [16, 44]. All other planform properties, such as aspect ratio and sweep, were maintained. The twist was defined as two degrees of linear washout on the inboard panel and an additional degree in the outboard panel. The wing position was also adjusted to maintain the tail volume coefficients of the SUGAR design. A three-view of the aircraft is shown in Figure 4.1. The strut is not included for the current aerodynamic analysis.

Three iterations of a half-span model of the S207 SNLF TTBW configuration were analyzed computationally, with subsequent geometries being developed upon discovery of errors in its predecessor. These errors will be discussed in depth in coming sections of this chapter. The generated grids were hybrid with prisms in the near-wall boundary layer regions and tetrahedral elements in the regions of inviscid flow. Meshing parameters were held relatively constant so the number of elements changed very little between grids generated for each configuration. The grids for Configuration 1, Configuration 2, and Configuration 3

had 70, 72, and 72 million nodes, respectively. As an example, images of the Configuration 2 mesh with details of the resolution through the slot can be viewed in Figure 4.2.

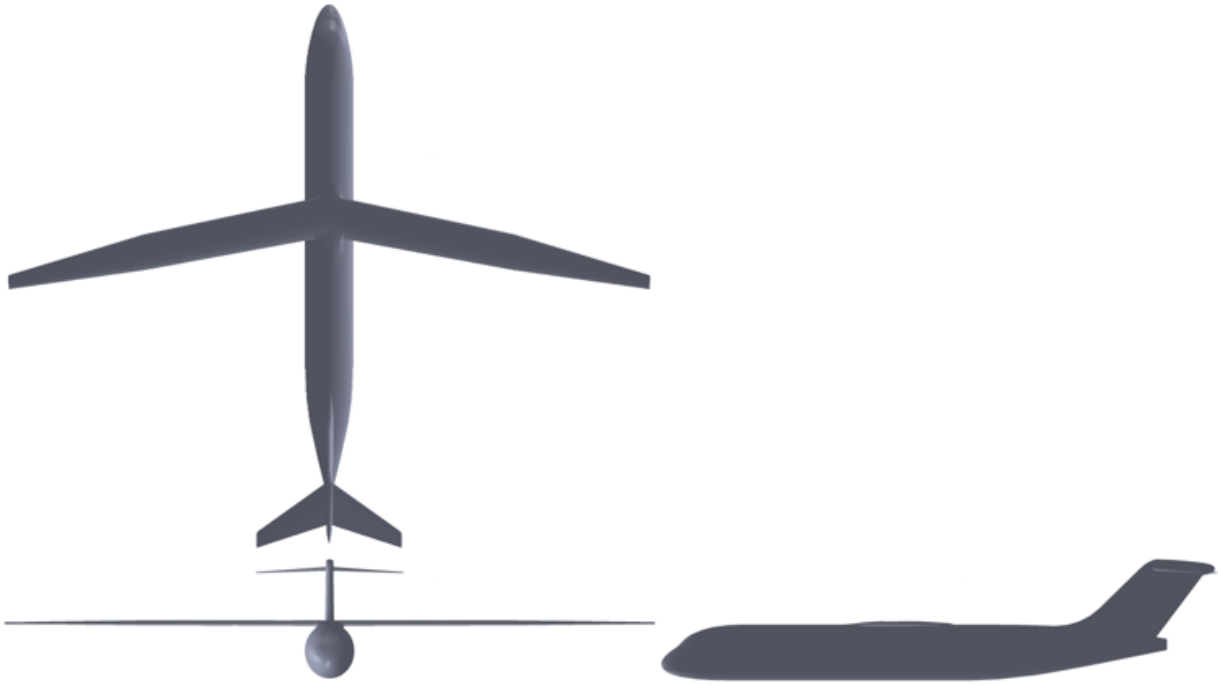

Figure 4.1: S207 Vehicle Geometry for Aerodynamic Analysis

4.2 Results for the Initial Configuration

Configuration 1 was used to compute a full set of drag polars for Mach numbers ranging from 0.200 to 0.750, and angles of attack incremented from -2.0° to 5.0°. This data was requested by ULI associates at The Boeing Company to serve as input for their analysis of the S207 SNLF TTBW aircraft. Every case was run using both only the SA turbulence model, and a coupled SA-Menter free transition approach. This was done to examine the effect of free transition through comparison to fully turbulent results. In the case of free transition modeling, an N_{crit} value of 8.4 was used. The Reynolds number was held at a value of 1.4 million per foot. The reference value is the mean aerodynamic chord (MAC) and has a value of 8.786ft, making the chord-based Reynolds number equal to 12.3 million.

The drag polars obtained for Mach numbers of 0.5 and 0.7 are shown in Figure 4.3a.

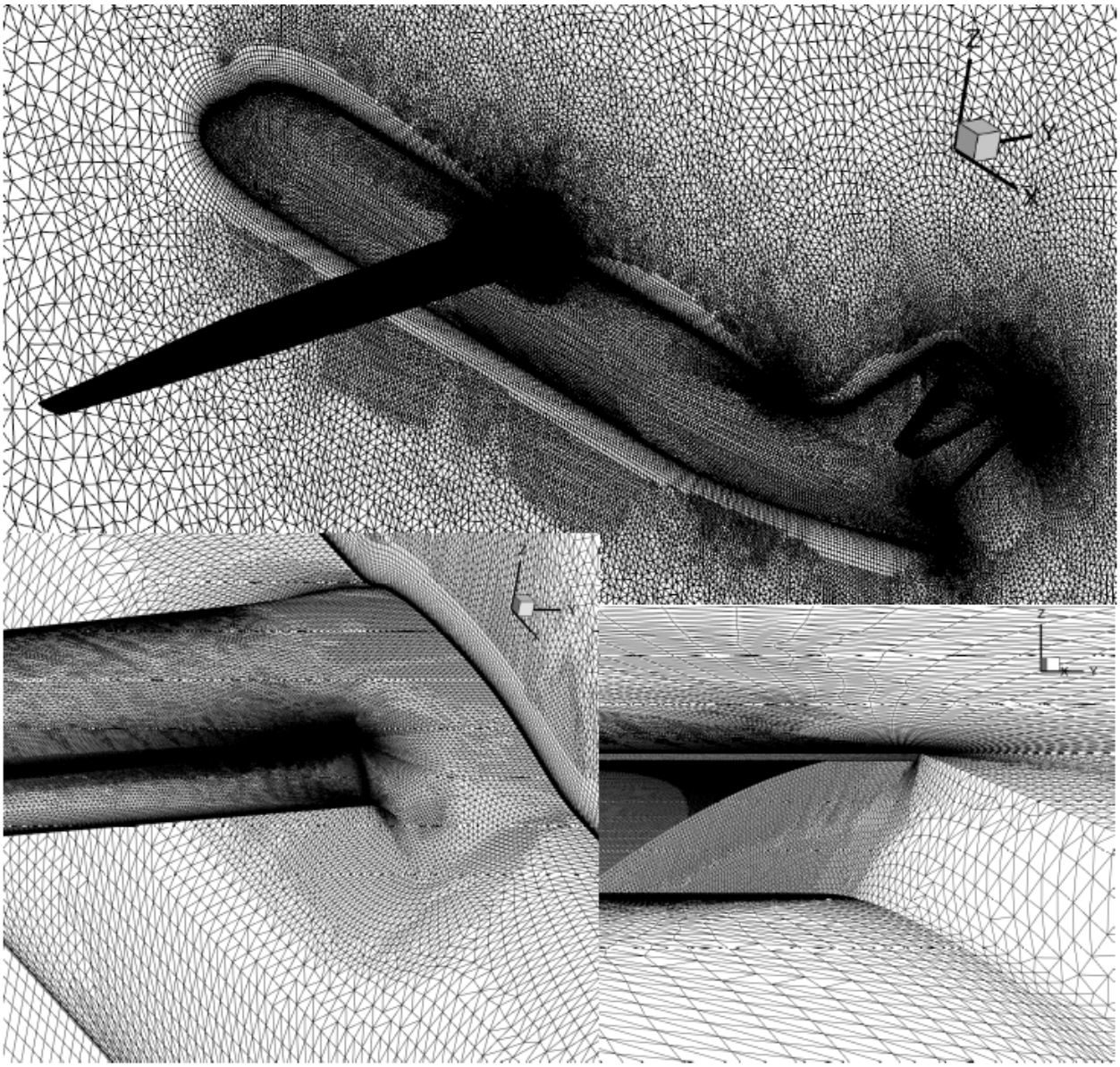

Figure 4.2: S207 Vehicle Configuration 2 Grid with Slot Refinement

The polars obtained for the free transition simulations display lower drag coefficient and higher lift coefficient values than the corresponding fully turbulent cases. This is similar to the behavior observed in two dimensions and again demonstrates the value of laminar flow. The spanwise lift distributions for these two Mach numbers computed with free transition are shown in Figure 4.3b. The Mach = 0.5 distribution appears smooth, with a nearly elliptic distribution, whereas the Mach = 0.7 distribution shows a lift deficit outboard of the 60% span location. This unexpected behavior was traced to the presence of a shock wave in the slot at the outboard span locations. Interestingly, and as mentioned in Section 3.3, the shock wave was present in both fully turbulent and free transition results. The solution associated with an angle of attack of 0° was scrutinized, and Figure 4.4a shows Mach contours at 12.2%, 61.4%, and 73.7% span. From these images the formation of the shock wave in the slot becomes evident. Figure 4.4b displays a pressure coefficient (C_p) contour with the flap removed for visualization through the slot. There is a region of low pressure indicative of supersonic flow clearly visible in the outboard region where the shock wave forms. It is clear that the formation of the shock wave causes flow separation downstream on the surface of the flap due to the total pressure loss across the shock wave.

4.3 Configuration 2 Results

In the design of the aircraft wing, a sweep transformation was used on the S207-based TTBW configuration to define profiles parallel to the freestream. This was convenient for lofting purposes. The streamwise airfoil sections were generated by transforming the standard S207 airfoil for the local sweep of inboard and outboard panels using conical sweep transformation relations [45, 46]. A miscalculation in the transformation was discovered, and its correction led to the definition of a new wing geometry which was used in turn to construct a new aircraft denoted as Configuration 2. A comparison of wing cross sections for Configurations 1 and 2 can be viewed in Figure 4.5. The difference in coordinates at the entrance of the slot was 0.13 inches in the horizontal direction and 0.16 inches in the vertical direction. This is in the range 0.1% chord variations that was found in Section 3.3 to have

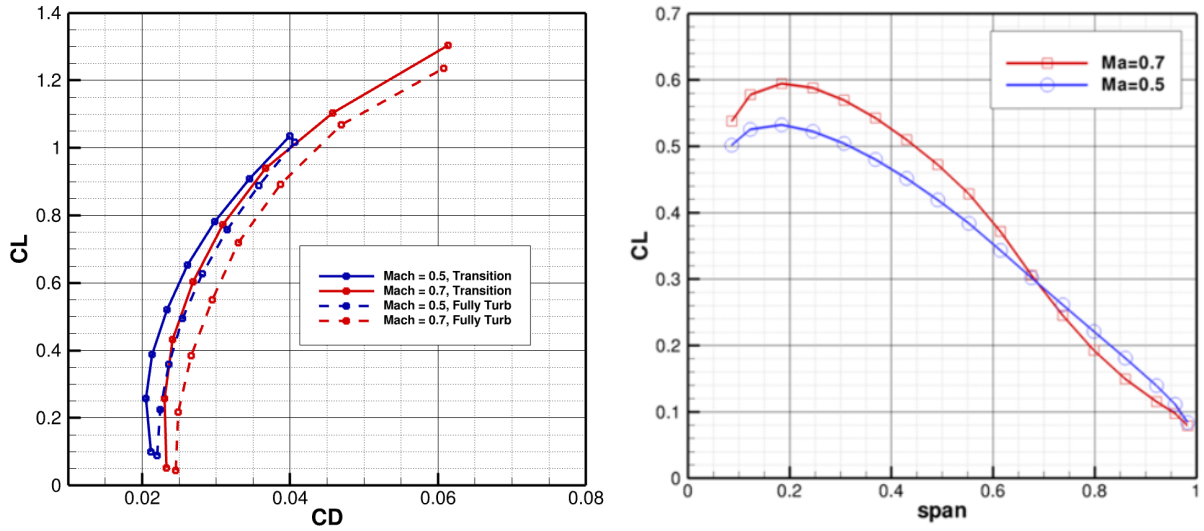

(a) Performance Polars

(b) Free Transition Lift Distributions

Figure 4.3: Configuration 1 NSU3D-SA Fully Turbulent and NSU3D-SA-Menter Free Transition Results

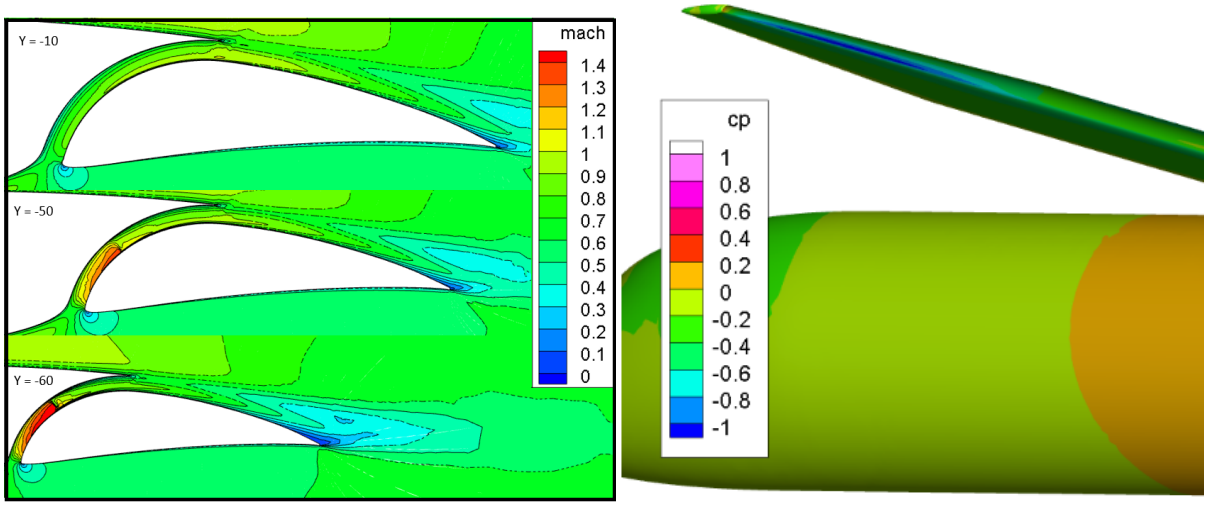

(a) Mach Contours at 12.2% (top) , 61.4% (middle), 73.7% (bottom) Span

(b) C_p Contour Through Slot with Flap Removed for Visualization

Figure 4.4: Configuration 1 NSU3D-SA Fully Turbulent Shock Formation at Mach = 0.7, Re = 12.3x10^6, AOA = 0°

adverse effects on the airfoil performance and is larger than manufacturing tolerances.

An examination of spanwise flow characteristics was conducted for a fully turbulent Configuration 2 simulation at a Mach number of 0.7, a Reynolds number of 12.3 million, and an angle of attack of 0°, and no shock wave formation was observed through the slot in the outboard region. Figure 4.6 illustrates this more desirable behavior through Mach contour plots again at 12.2%, 61.4%, and 73.7% span as well as the surface C_p distribution in the slot region. It is evident that not only is there no shock, but the previously observed region of low pressure is no longer present.

Drag polars for fully turbulent flow, using the SA turbulence model alone, and free transition flow, using the SA-Menter approach, were generated for identical Mach numbers and angles of attack as done previously for Configuration 1. Again, this data was requested and provided to ULI project members at The Boeing Company to serve as input for their analysis of the S207-based SNLF TTBW aircraft. N_{crit} was set to 8.4 and the Reynolds number was held at 1.4 million per foot with the MAC being equal to 8.786ft. These drag polars are included in Figure 4.7. The effect of free transition is more precisely quantified through the drag polars and lift curves for Mach numbers of 0.5 and 0.7 in Figure 4.8, and the previously observed trends hold with the free transition solutions predicting higher lift coefficients and lower drag coefficients than the fully turbulent computations. As another means to highlight the differences in the modeling approaches, Figure 4.9 compares the computed skin friction drag for free transition and fully turbulent simulations. Here, the fully turbulent cases show relatively flat profiles as a function of angle of attack, whereas the free transition data forms a low-drag bucket roughly in the region between 0° and 3° angle of attack. The transition location predicted by the free transition model can be found with the use of skin friction drag contours, as shown for a Mach number of 0.7 and angle of attack of 0° in Figure 4.10.

Though the use of Configuration 2 was successful in eliminating the presence of any shock waves at cruise conditions, skin fiction drag contours in Figure 4.10 suggest that transition occurs significantly more upstream on both the upper and lower surfaces of the fore element compared to the two-dimensional design behavior discussed in Section 3.2.

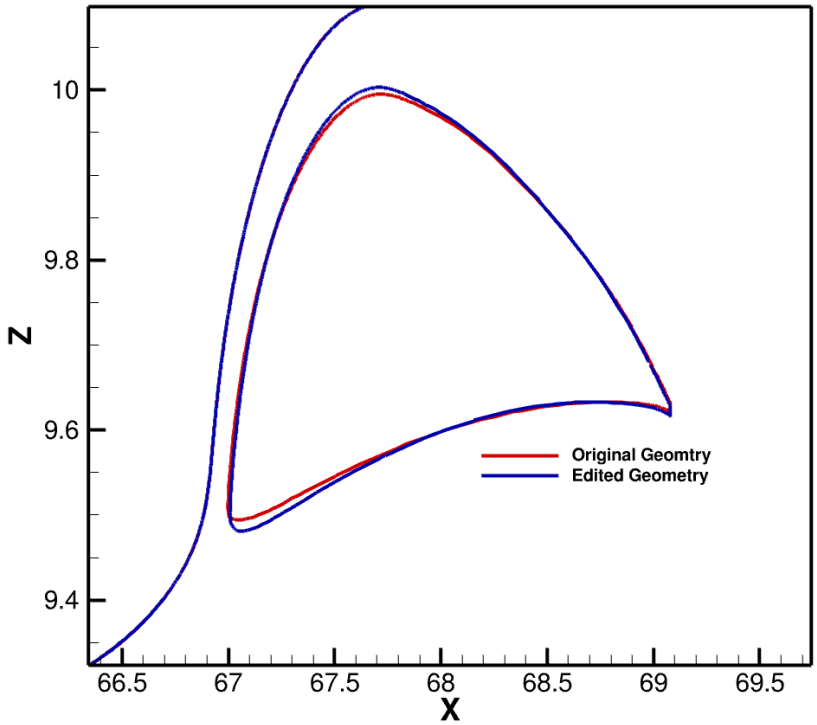

Figure 4.5: Wing Cross Section Comparison Between Configurations 1 and 2

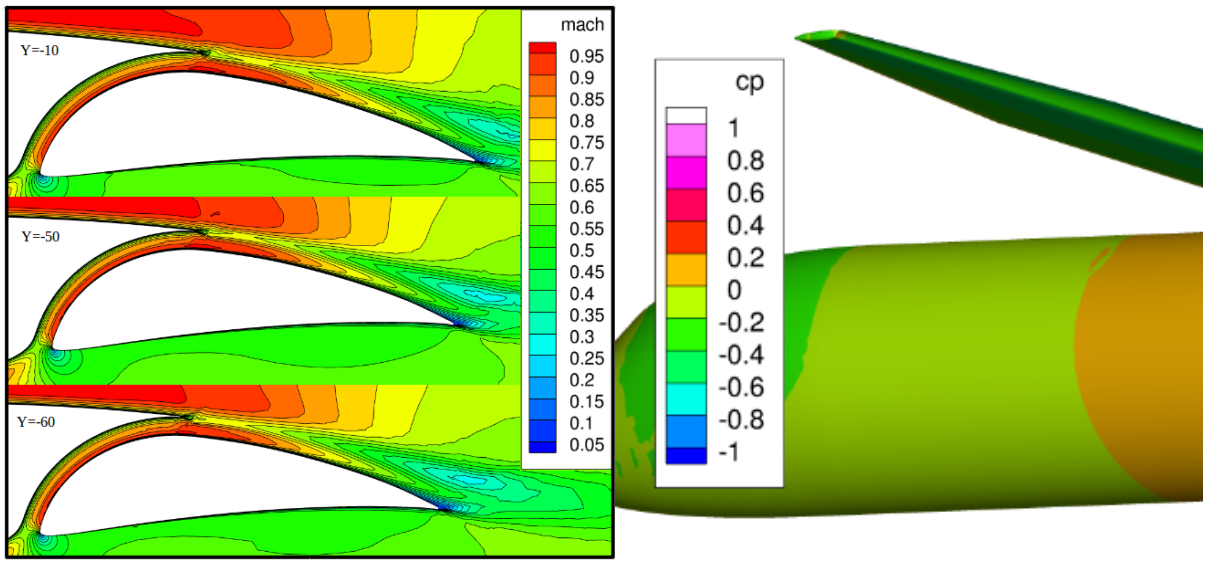

(a) Mach Contours at 12.2% (top) , 61.4% (middle), 73.7% (bottom) Span

(b) C_p Contour Through Slot with Flap Removed for Visualization

Figure 4.6: Configuration 2 NSU3D-SA Fully Turbulent Flow Characteristics at Mach = 0.7, Re = 12.3x10^6, AOA = 0°

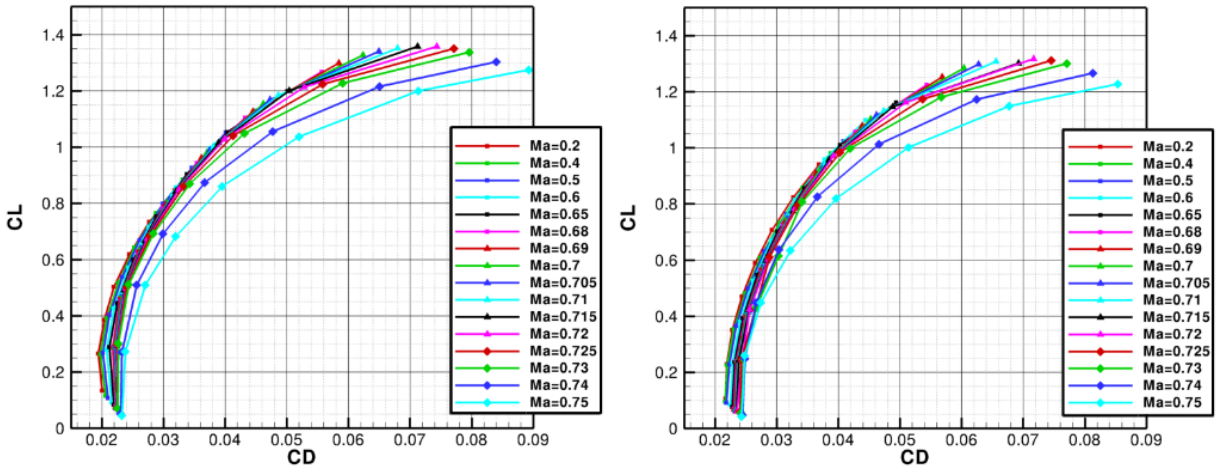

(a) NSU3D-SA-Menter Free Transition

(b) NSU3D-SA Fully Turbulent

Figure 4.7: Configuration 2 Performance Polars for Re = 12.3x10^6

Comparing spanwise lift values with two-dimensional results at a Mach number of 0.7 and an angle of attack of 0° reveals that, over the entire span, the sectional C_L based on local chord falls within the bounds of the upper and lower limits of the low-drag bucket [10], as shown in Figure 4.11. Additionally, the figure shows how the redesigned wing configuration achieves a smooth, nearly elliptic MAC-based lift distribution, which is just further evidence of no shock waves forming in the slot.

In order to further investigate the possible causes of the early transition on Configuration 2, computed C_p profiles at select spanwise stations are compared to two-dimensional results obtained on the S207 airfoil at the same conditions. This offers insight as to whether or not sectional C_L values in three dimensions are similar to C_L values computed in two dimensions. All comparisons are done using results from fully turbulent simulations. This eliminates any need to consider possible discrepancies between transition prediction implementations. Figure 4.12 illustrates the NSU3D-SA fully turbulent computed surface pressure profiles for both the fore and aft elements at spanwise locations of 8.6%, 18.4%, and 36.9% for a Mach number of 0.7 and angle of attack of 0° overlaid against the NSU2D-SA fully turbulent solutions for a Mach number of 0.7, Reynolds number of 13.2 million and angles of attack of -1.0° and -1.3°. Agreement is quite poor at the location nearest the fuselage (8.6%), particularly at the trailing-edge of the fore element and through the slot. Locations further

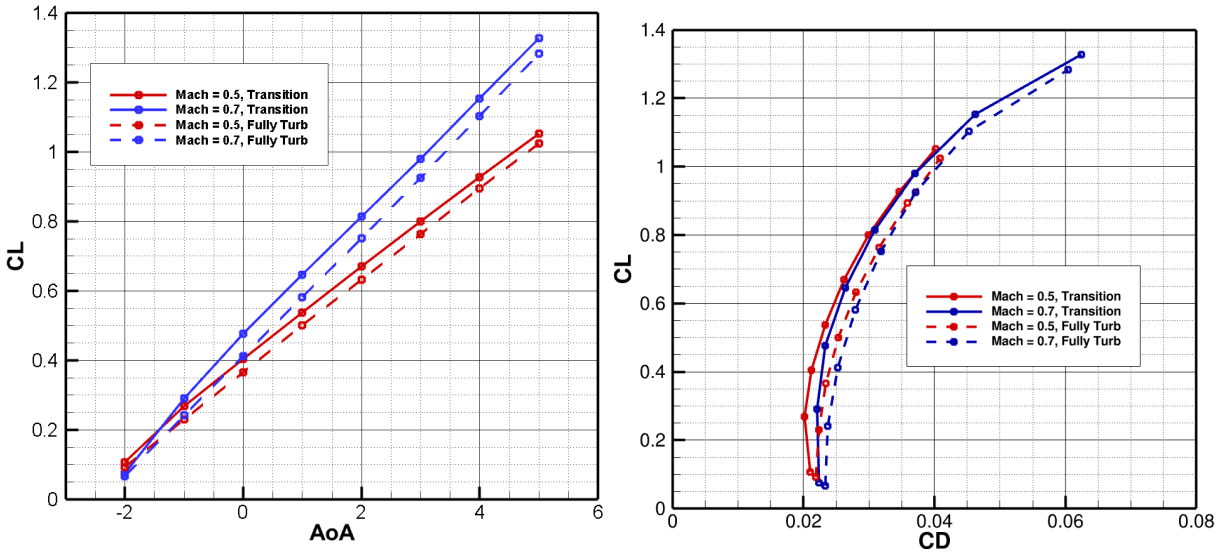

(a) Lift Curves (b) Polars

Figure 4.8: Configuration 2 Free Transition Effects for Re = 12.3x10^6 and N_{crit}=8.4

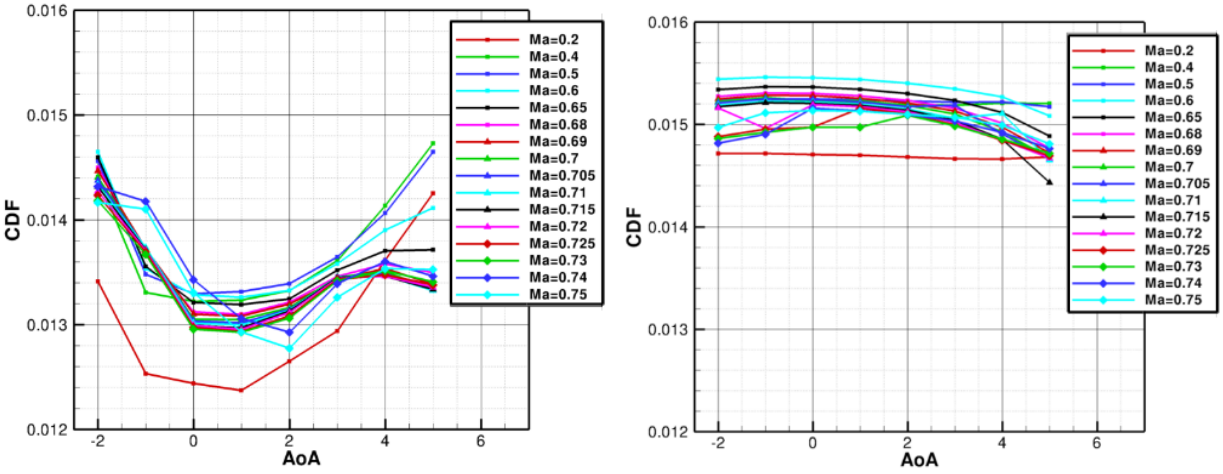

(a) NSU3D-SA-Menter Free Transition (b) NSU3D-SA Fully Turbulent

Figure 4.9: Configuration 2 Skin Friction Drag vs Angle of Attack for Re = 12.3x10^6

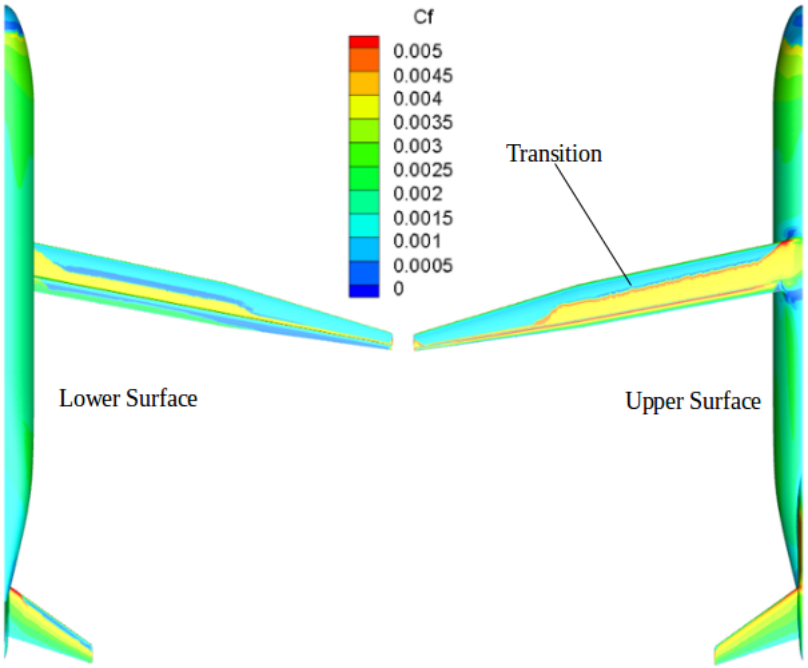

Figure 4.10: Configuration 2 Skin Friction Drag Contour for Mach = 0.7, Re = 12.3x10^6, AOA = 0°

outboard (18.4% and 38.9%) are more consistent with two-dimensional results with the exception of the region associated with the slot. Additionally, the favorable pressure gradient on the upper surface of the fore element, which is responsible for maintaining laminar flow, is less pronounced in the three-dimensional profiles, particularly at the more inboard section. Note that these comparisons do not include any sweep corrections, which would be on the order of 5% given the wing sweep angle of 12.5% [43].

4.4 Initial Results for Configuration 3

In light of the results obtained on Configuration 2, further geometric modifications were made by the ULI members at the University of Tennessee at Knoxville resulting in airfoil sections that more closely aligned with the S207 two-dimensional geometry. A new geometry was defined, denoted as Configuration 3, and an associated grid was generated. A single case was run at a Mach number of 0.7, angle of attack of -1.0, a Reynolds number of 12.3 million (1.4 million per foot with the MAC remaining at 8.786ft), and an N_{crit} of

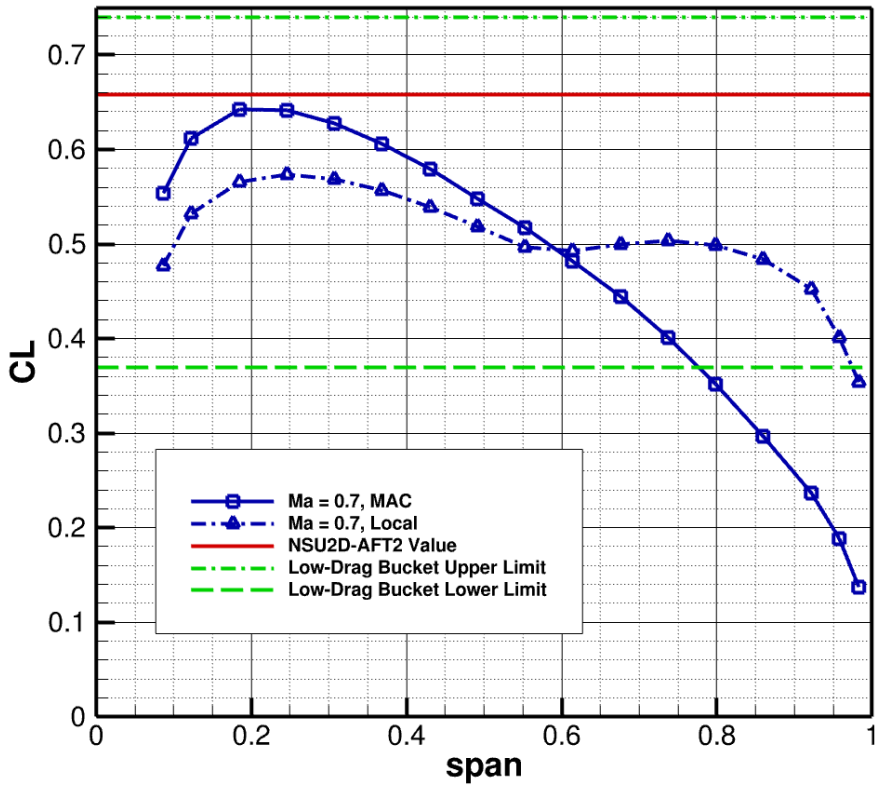

Figure 4.11: Configuration 2 NSU3D-SA-Menter Free Transition Lift Distributions at Mach = 0.7, Re = 12.3x10^6, AOA = 0°, and N_{crit} = 8.4

8.4 for Configuration 3. The upper surface skin friction drag for this simulation is shown as Figure 4.13. The transition location not only doesn't show any improvement compared to Configuration 2, but is significantly worse with the entire upper surface appearing fully turbulent. At this point the decision was made to run the AFT2 transition prediction model in place of the Menter model for this case. The resulting upper surface skin friction drag is shown in Figure 4.14. The AFT2 model predicts delayed transition at these conditions, which is more in line with expectations of the S207 SNLF airfoil.

Though the AFT2 model predicts improved laminar flow behavior, further adjustments to the approach were still necessary. Note that in Figure 4.14 the nose of the aircraft is laminar, with very low skin friction drag. Identical behavior is also observed in Figure 4.10. This is unrealistic as laminar flow is not to be expected on the fuselage [43]. It was at this point in the analysis that the patch-based and box-based transition model application capabilities of NSU3D discussed in Section 2.3 were implemented and utilized.

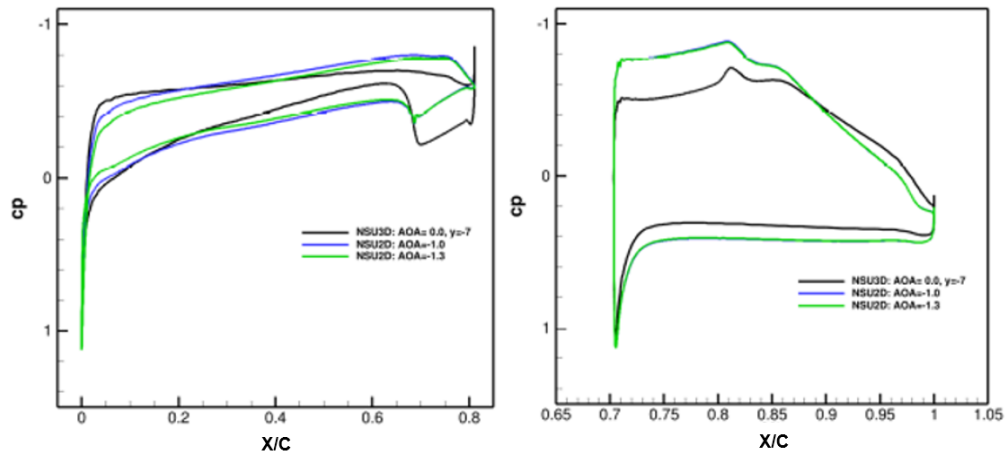

(a) 8.6% Span

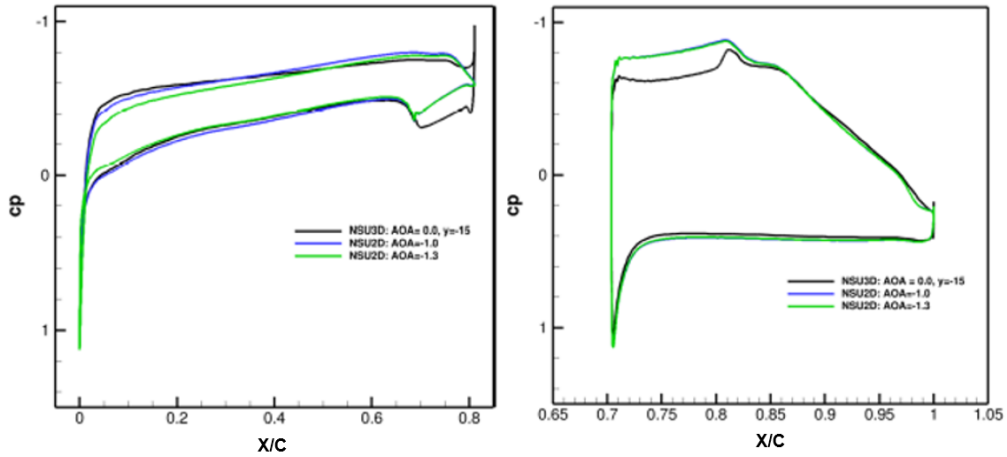

(b) 18.4% Span

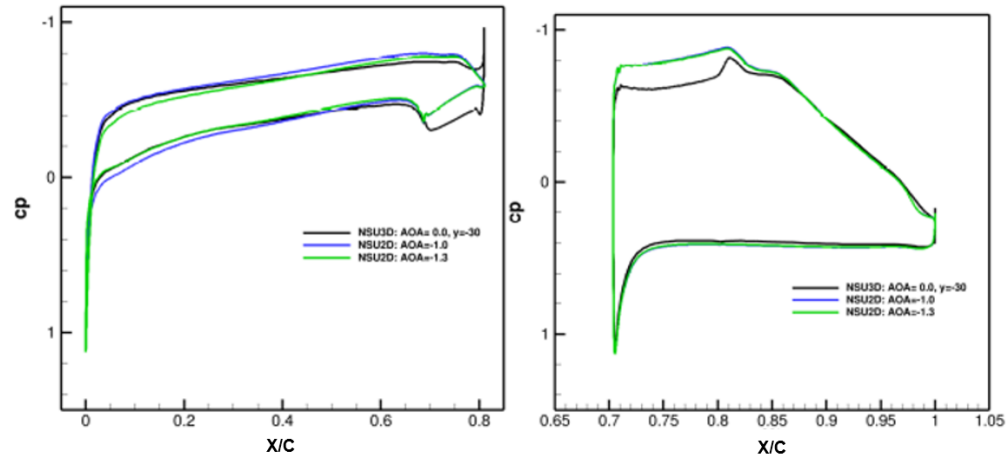

(c) 36.9% Span

Figure 4.12: Configuration 2 NSU3D-SA Fully Turbulent Surface Pressure at Mach = 0.7, AOA = 0°, Re = 12.3x10^6 Compared to NSU2D-SA Fully Turbulent Surface Pressures at Mach = 0.7, Re = 13.2x10^6

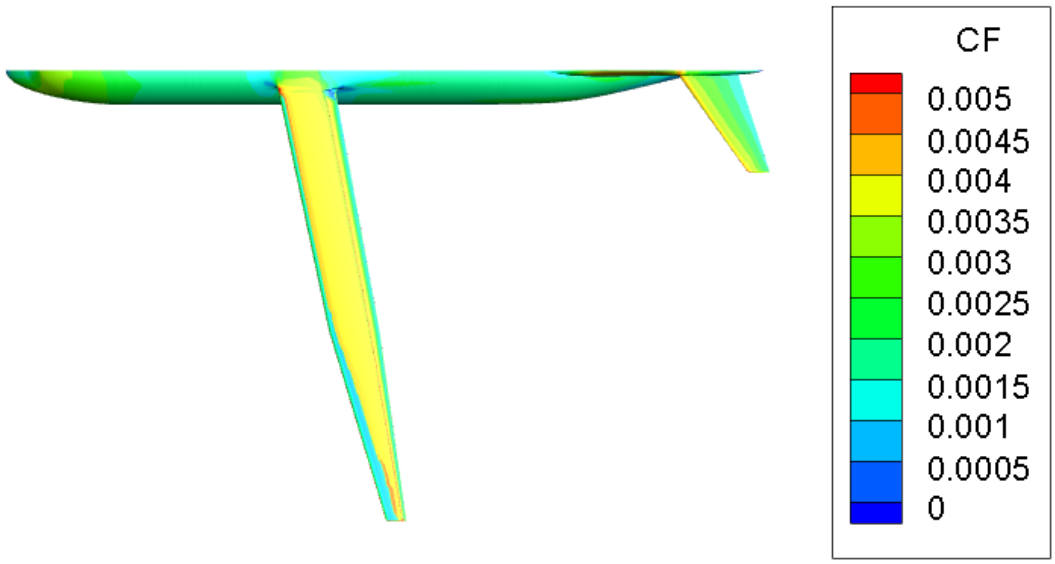

Figure 4.13: Configuration 3 NSU3D-SA-Menter Free Transition Upper Surface Skin Friction Drag for Mach = 0.7, Re = 12.3x10^6, AOA = -1°, and N_{crit} = 8.4

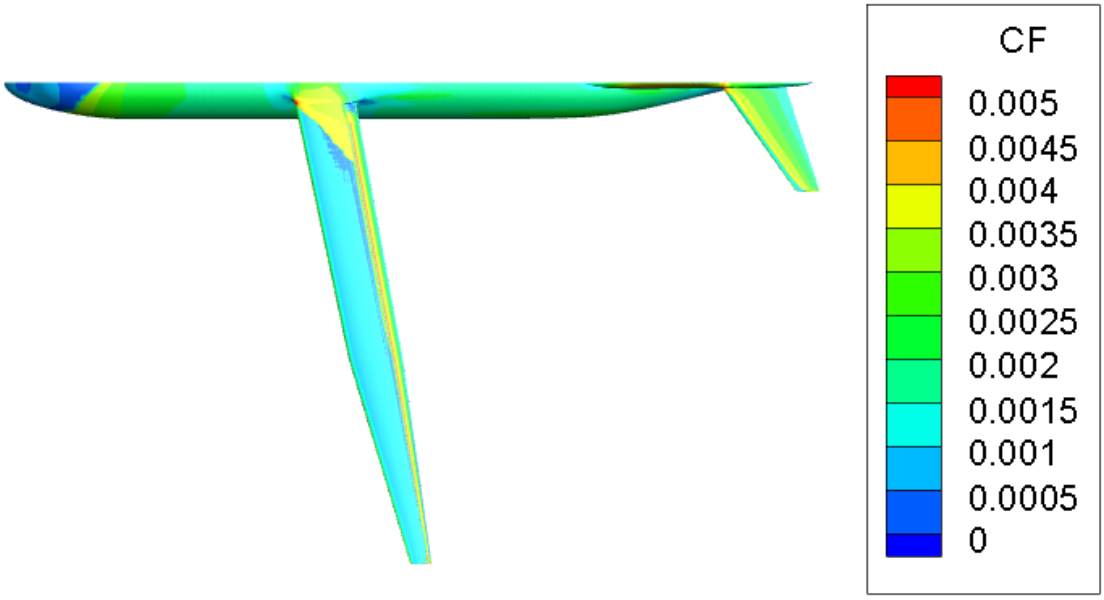

Figure 4.14: Configuration 3 NSU3D-SA-AFT2 Free Transition Upper Surface Skin Friction Drag for Mach = 0.7, Re = 12.3x10^6, AOA = -1°, and N_{crit} = 8.4

Two drag polars, both requested by ULI project members at The Boeing Company and referred to as Cases 1 and 2 from here on in, were developed for a Mach number of 0.7273, a Reynolds number of 12.3 million, and an N_{crit} of 8.4. The angles of attack were constrained to the values of -1°, -2°, 0°, 1°, 1.5°, 2°, and 2.5°. Each case applied the transition model to regions of the wing, excluding the fuselage. Case 1 modeled the entire wing as free transition. Case 2 is representative of leading-edge tripping with the upper surface of the fore element and the entirety of the aft element modeled as free transition, and the lower surface of the fore element starting at 3% chord modeled as fully turbulent to simulate the presence of a Krueger flap that stows on the lower surface of the fore element during cruise. A segmented profile of the S207 airfoil cross section is shown in Figure 4.15, and the specifications of Case 1 and Case 2 are detailed using these segments in Table 4.1. Lift and drag values for each of the simulations conducted as part of Case 1 and Case 2 are compared in Figure 4.16 and Table 4.2. Similarly, the total skin friction drag for each simulation is quantified in Figure 4.17, where formation of a low-drag bucket can be observed. Unsurprisingly, Case 1 predicts higher lift and lower drag for all angles of attack. This is due to more significant runs of laminar flow on the lower surface of the fore element. The upper surface skin friction drag contours for each of the Case 1 simulations are detailed in Figure 4.18, and the same is done for the lower surface in Figure 4.19. From these images it can be stated that laminar flow is more significant on the upper surface for lower angles of attack, and the opposite is true for the lower surface.

A final investigation was undertaken as part of initial computational efforts conducted on Configuration 3 to determine if the transition on the upper surface of the wing would be impacted by a reduction in turbulent flow near the fairing. Three simulations at a Mach number of 0.7273, an angle of attack of 1°, and a Reynolds number of 12.3 million were performed, each with a progressively larger region of application of the free transition model at the wing-fairing junction. This is illustrated in Figure 4.20. The predicted upper surface skin friction drag profiles are catalogued in Figure 4.21. From these results the location of upper surface transition does not seem to be beneficially impacted by more laminar flow in the region of the wing-fairing junction.

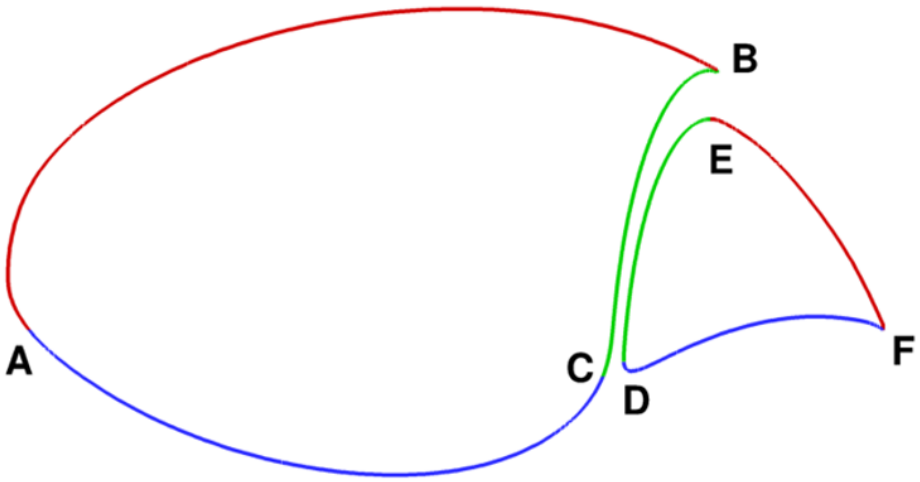

Figure 4.15: Division of S207 Profile for Flow Model Application

Table 4.1: Segment Modeling Summary for Grid 3

Case Number	Element	Segment	Modeling
1	Fore	AB	Free Transition
		AC	Free Transition
		CB	Free Transition
1	Aft	DE	Free Transition
		DF	Free Transition
		EF	Free Transition
2	Fore	AB	Free Transition
		AC	Fully Turbulent
		CB	Fully Turbulent
2	Aft	DE	Free Transition
		DF	Free Transition
		EF	Free Transition

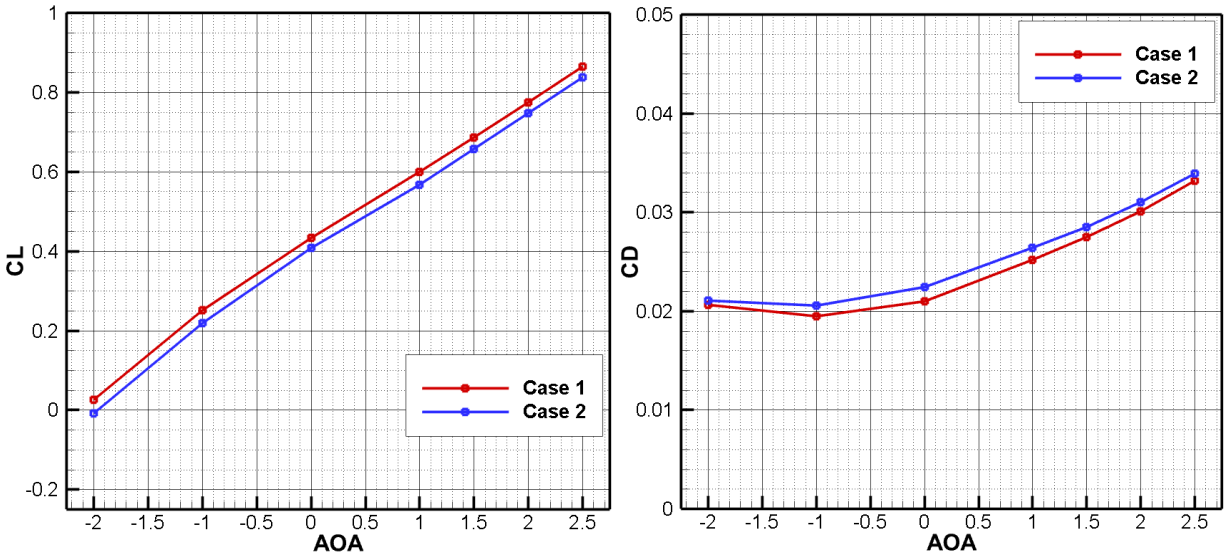

(a) Lift (b) Drag

Figure 4.16: Configuration 3 NSU3D-SA-AFT2 Free Transition Force Coefficient Curves at Mach = 0.7273, Re = 12.3x10^6, and N_{crit} = 8.4

Table 4.2: NSU3D-SA-AFT2 Free Transition Lift and Drag Values for Configuration 3 at Mach = 0.7273, Re = 12.3x10^6, N_{crit} = 8.4

Case Number	Angle of Attack	C_L	C_D
Case 1	-2.00°	0.0250755809	0.0206113068
	-1.00°	0.2519359000	0.0194720149
	0.00°	0.4332683130	0.0210144158
	1.00°	0.6000374260	0.0251781831
	1.50°	0.6864091240	0.0274875215
	2.00°	0.7750443420	0.0301037591
	2.50°	0.8651606570	0.0331735695
Case 2	-2.00°	-0.0087226616	0.0210632758
	-1.00°	0.2192064180	0.0205394374
	0.00°	0.4074759850	0.0224077157
	1.00°	0.5677787590	0.0263974269
	1.50°	0.6571697780	0.0285320763
	2.00°	0.7479776920	0.0309886014
	2.50°	0.8381463260	0.0339210770

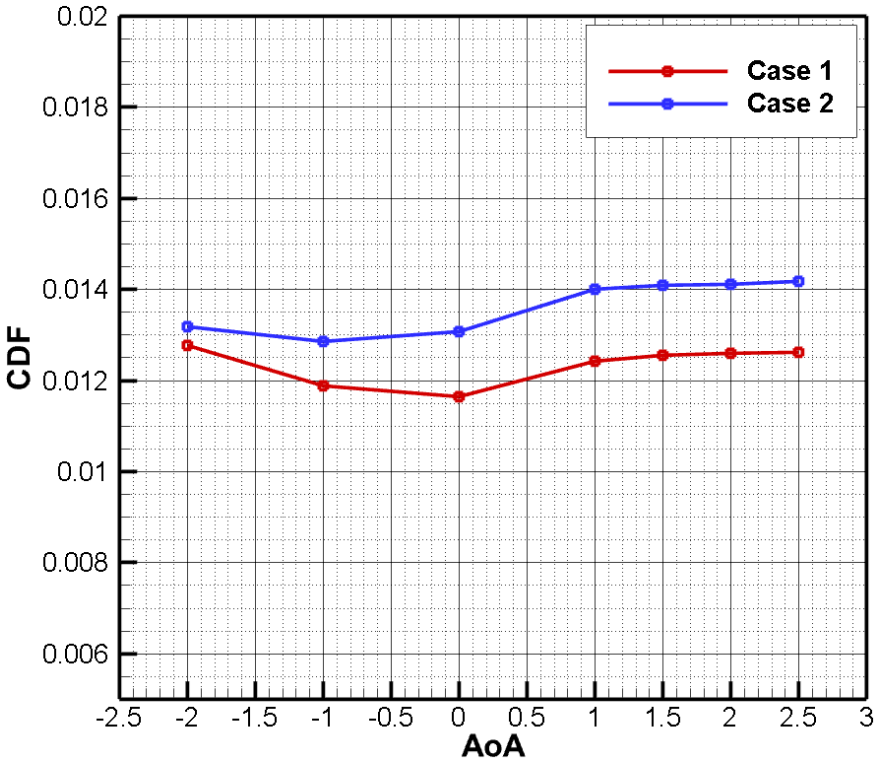

Figure 4.17: Configuration 3 NSU3D-SA-AFT2 Free Transition Skin Friction Drag at Mach = 0.7273, Re = 12.3x10^6, and N_{crit} = 8.4

4.5 Polars for Configuration 3

In addition to a strictly fully turbulent approach, the modeling strategies employed for Cases 1 and 2 in Section 4.4 were further utilized to generate full performance polars in the same manner as Configurations 1 and 2. The fully turbulent drag polars and drag polars where free transition was applied to the entire wing (Case 1 specifics) were run for Mach numbers ranging from 0.200 to 0.750. Angles of attack were incremented from -2° to 5°. The polars developed by applying free transition modeling to the entire wing except for the lower surface of the fore element (Case 2 specifics) required a reduction in cases due to lack of computational resources. The upper and lower limit of Mach numbers used were adjusted to 0.400 and 0.730, with every other Mach number typically used being omitted. Additionally, angles of attack were instead only incremented from -1° to 3°. MAC-based Reynolds number was 12.3 million and in the case of free transition modeling an N_{crit} of 8.4 was used. This data was once again requested and provided to ULI associates at The Boeing Company for

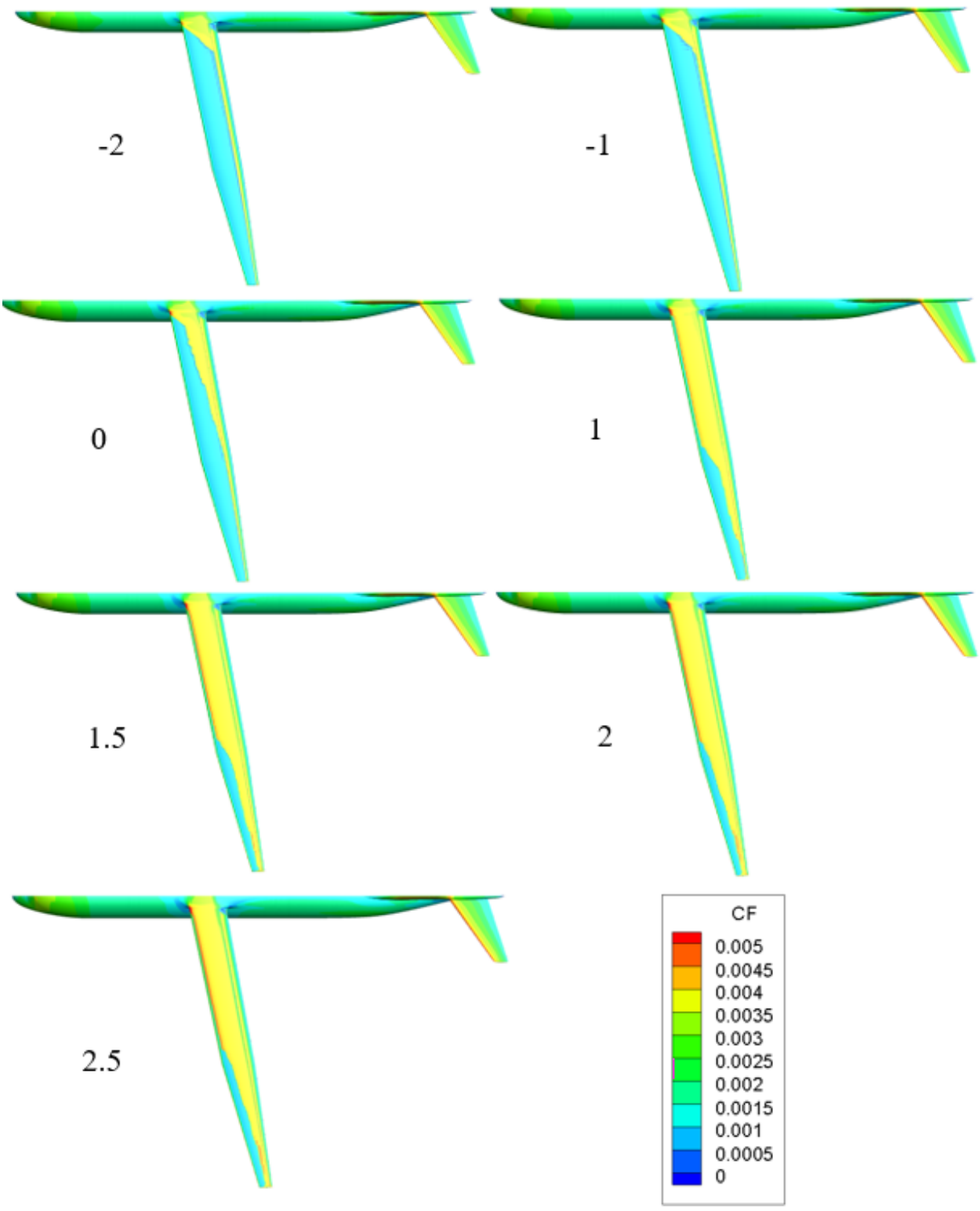

Figure 4.18: Configuration 3 NSU3D-SA-AFT2 Free Transition Case 1 Upper Surface Skin Friction Drag Contours at Mach = 0.7273, Re = 12.3x10^6, and N_{crit} = 8.4

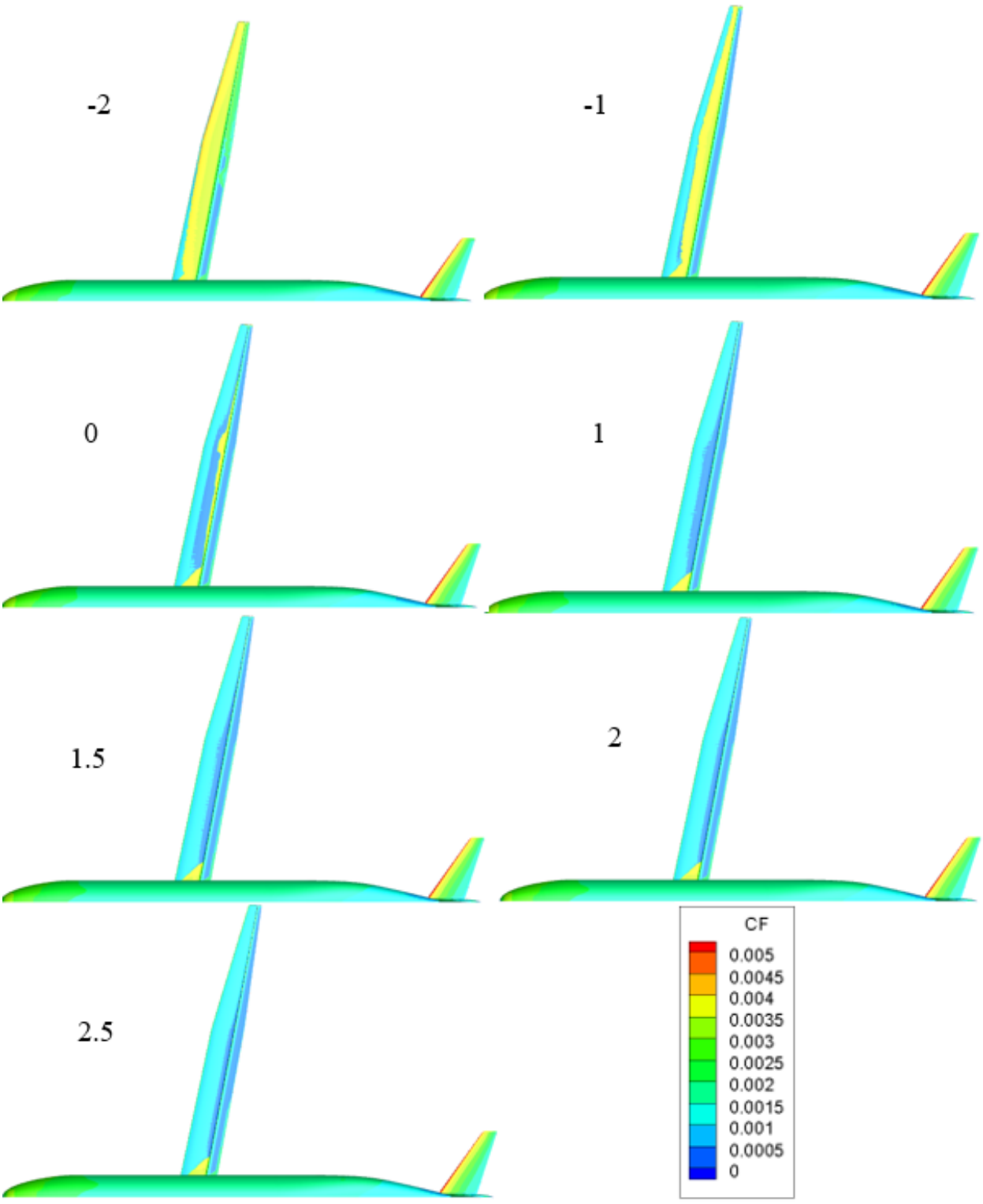

Figure 4.19: Configuration 3 NSU3D-SA-AFT2 Free Transition Case 1 Lower Surface Friction Drag Contours Mach = 0.7273, Re = 12.3x10^6, and N_{crit} = 8.4

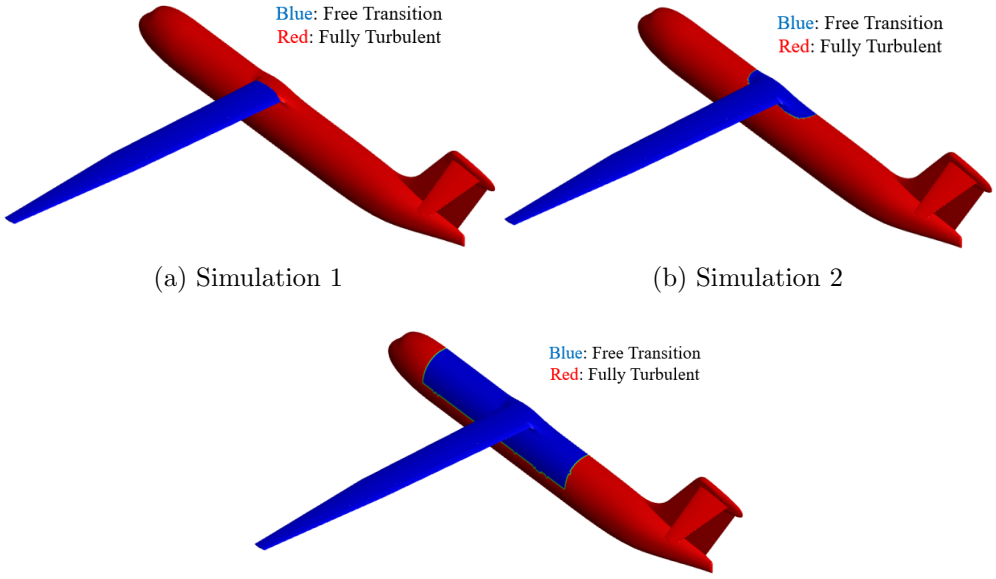

(a) Simulation 1

(b) Simulation 2

(c) Simulation 3

Figure 4.20: Configuration 3 NSU3D-SA-AFT2 Free Transition Expansion Summary

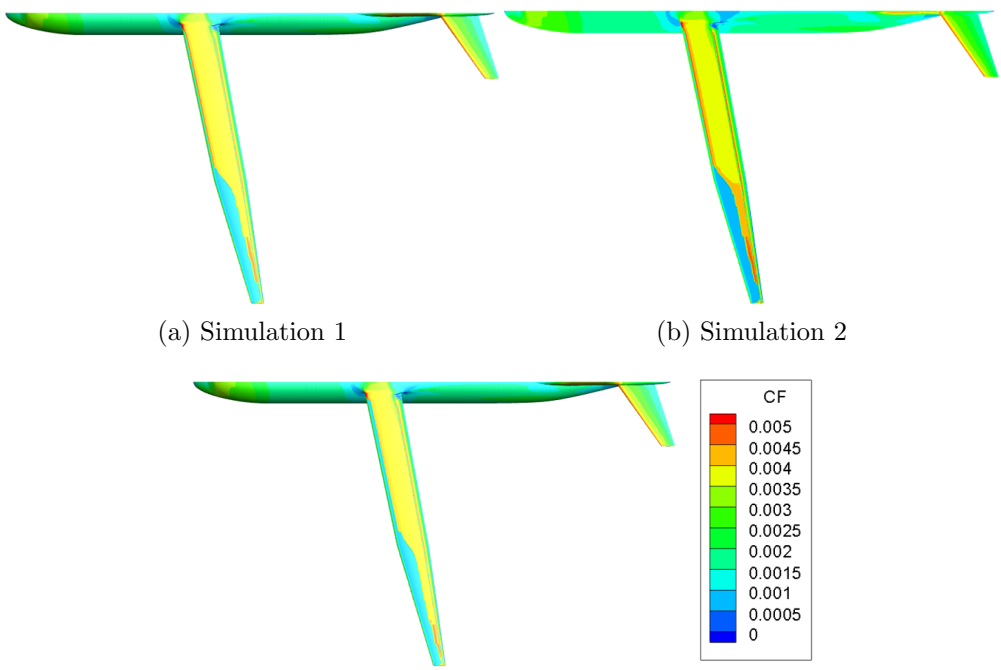

(a) Simulation 1

(b) Simulation 2

(c) Simulation 3

Figure 4.21: Configuration 3 NSU3D-SA-AFT2 Free Transition Expansion Results at Mach=0.7, Re = 12.3x10^6, AOA=1°, and N_{crit} = 8.4

use in their analysis of the S207-based SNLF TTBW aircraft.

Lift and drag curves for the fully turbulent simulations are shown in Figure 4.22, and drag polars are shown in Figure 4.23. Pitching moment curves are included as Figure 4.24, and both pressure drag and skin friction drag are quantified in Figure 4.25. Note that the skin friction drag profile is relatively constant for each Mach number as expected for fully turbulent cases.

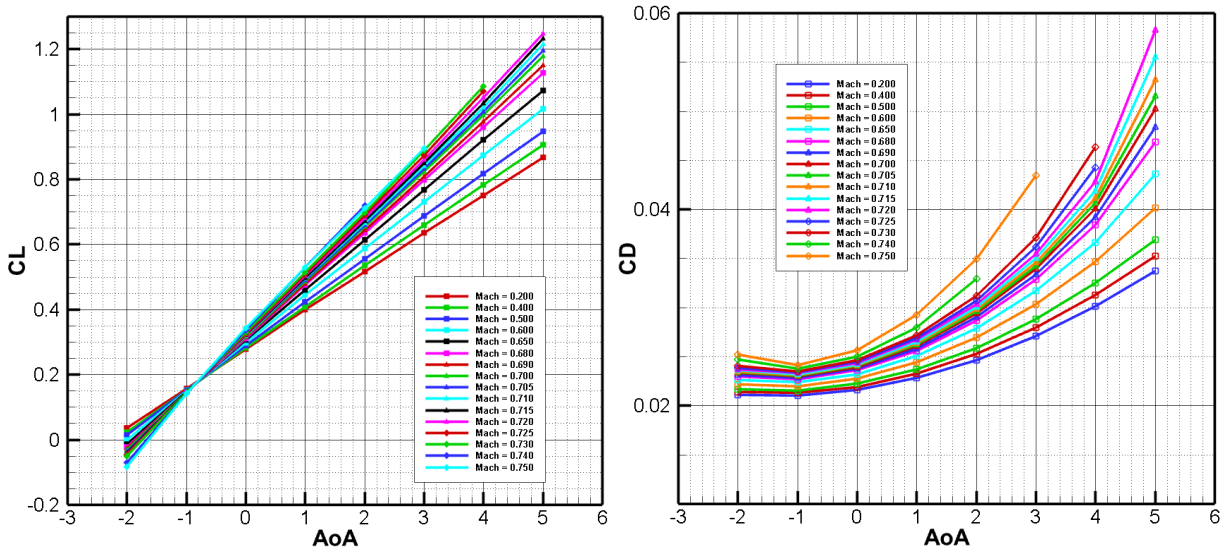

(a) Lift (b) Drag

Figure 4.22: Configuration 3 NSU3D-SA Fully Turbulent Force Coefficient Curves

The lift and drag curves associated with data generated by applying free transition modeling to the entire wing are viewable in Figure 4.26. The drag polars are shown in Figure 4.27a, and these drag polars for Mach numbers of 0.5 and 0.7 are compared to the corresponding fully turbulent curves in Figure 4.27b. Again, more beneficial behavior is observed with the application of a transition prediction model as was demonstrated in two dimensions. The pitching moment curves and drag curves are included as Figure 4.28 and 4.29, respectively. Figure 4.29a predicts the formation of a low-drag bucket between -1° and 2°, which can be compared to Figure 4.25a which shows no formation of a low-drag bucket for fully turbulent simulations.

Comparisons made in Section 4.3 to two-dimensional results are reproduced using Configuration 3. The spanwise C_L values found using free transition and computed with the

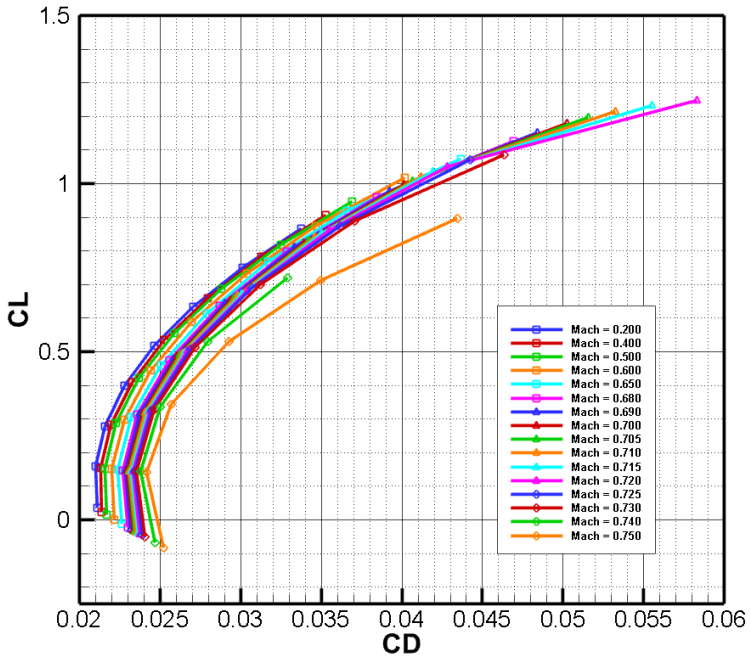

Figure 4.23: Configuration 3 NSU3D-SA Fully Turbulent Drag Polars

MAC and local chord length are plotted for Mach numbers of 0.5 and 0.7 in Figure 4.30. Once again, most of the spanwise C_L values based on local chord for a Mach number of 0.7 and angle of attack of 0° successfully fall between the upper and lower limits of the low-drag bucket as defined in the design report of the S207 airfoil. Fully turbulent C_p profiles between two- and three-dimensional simulations at a Mach number of 0.7 are shown in Figure 4.31. These profiles do not include sweep corrections which would be on the order of 5% for the wing sweep of 12.5°. The station nearest the fuselage shows poor agreement with two-dimensional predictions. The outboard stations show better agreement but the C_P values on the upper and lower surfaces are closer together than what is predicted by two-dimensional and Configuration 2 results, so less lift is generated in comparison. The pressure at the trailing edge of the fore element, however, is computed to be less adverse than what is predicted by two-dimensional results.

The lift and drag curves for the polars developed by limiting the regions of free transition to the upper surface of the fore element and the entirety of the aft element are shown in Figure 4.32. Drag polar curves are shown in Figure 4.33, and skin friction drag and pressure drag curves are shown in Figure 4.34. Note that in Figure 4.32b the Mach=0.4

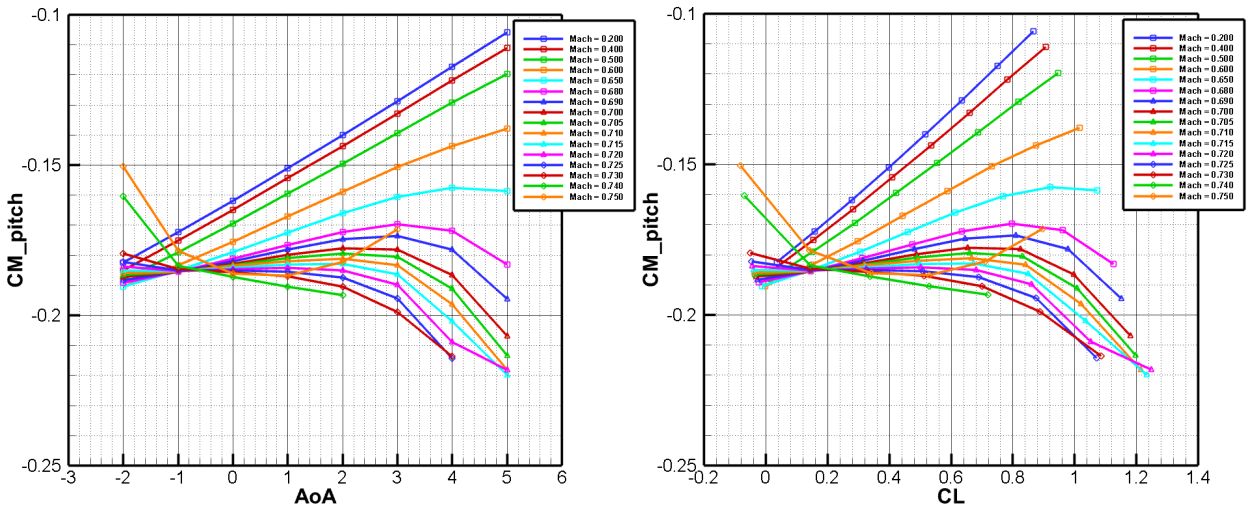

(a) Function of AoA

(b) Function of C_L

Figure 4.24: Configuration 3 NSU3D-SA Fully Turbulent Pitching Moment Curves

and Mach=0.5 curves cross over each other at an angle of attack of 0°. This behavior is even more pronounced in Figure 4.34a. Skin friction drag contours for these two cases are shown in Figure 4.35. There is more laminar flow predicted to occur at a Mach number of 0.5 than there is at a Mach number of 0.4 when the angle of attack is 0° which results in less drag at this higher Mach number. The same comparison was made for the previous polar set in which free transition was applied to the entire wing, as shown in Figure 4.36. Similar behavior is observed. The pressure gradient along the upper surface is expected to become less favorable as Mach number decreases [10], so the weaker suction peaks and weaker compressibility effects are likely the cause of this observed cross over between results for Mach numbers of 0.4 and 0.5.

In summary, CFD solutions generated for the ULI relevant S207-based SNLF TTBW aircraft configuration were instrumental in the the redesign of a wing capable of closely reproducing pressure distributions more in line with design intent, which in turn is critical for maintaining laminar flow. Following corrections of the geometry, significant runs of laminar flow were observed at cruise conditions for angles of attack ranging from -2° and 1°. However, several discrepancies remain. The transition region is still further upstream compared to two-dimensional S207 airfoil results. A deficiency of this aircraft design is that

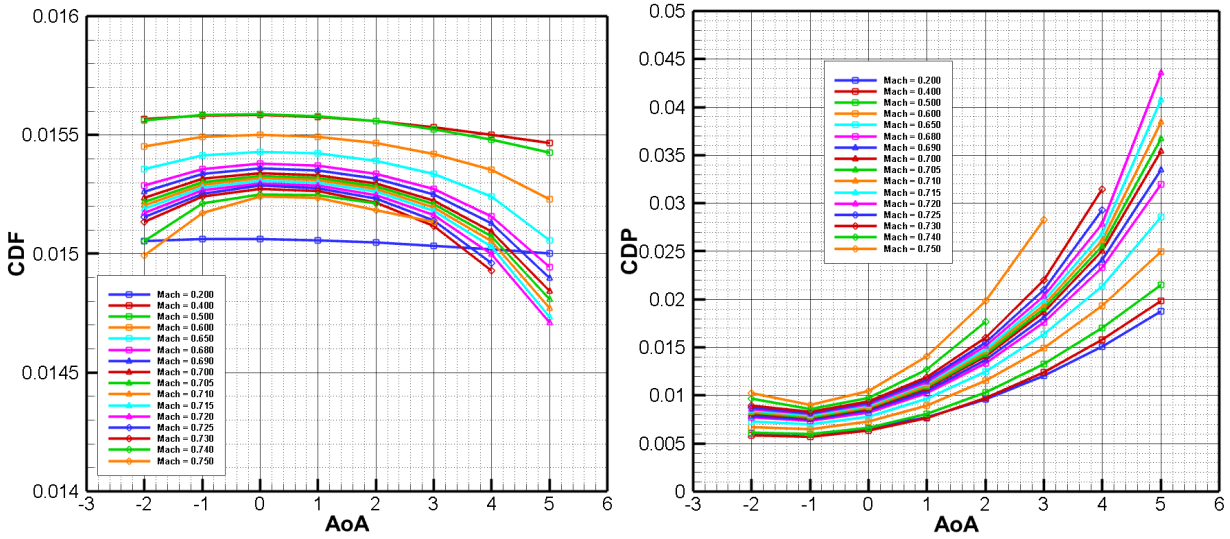

(a) Friction Drag

(b) Pressure Drag

Figure 4.25: Configuration 3 NSU3D-SA Fully Turbulent Drag Profiles

the fairing at the wing-fuselage junction is in need of improvement, and was observed to produce a local region of separation. The transition line is most forward near the wing-body junction which suggests this separation is causing early transition at the root of the wing, which then propagates out spanwise. Additionally, although the sectional- and MAC-based lift coefficient values fell within the low-drag bucket range for the S207 airfoil, significant differences in fully turbulent C_P profiles at wing spanwise cuts versus 2D airfoil results remain, particularly in the slot. This suggests further consideration of 3D effects in the design of the wing cross section may need to be taken into account to more closely match the design intent of the S207 airfoil in a three-dimensional swept wing setting. Additionally, several full drag polars that were generated and provided to ULI project members at The Boeing Company were instrumental in additional analysis of the S207-based SNLF TTBW aircraft. Both fully turbulent and free transitional runs, including runs with specified regions of both, were provided.

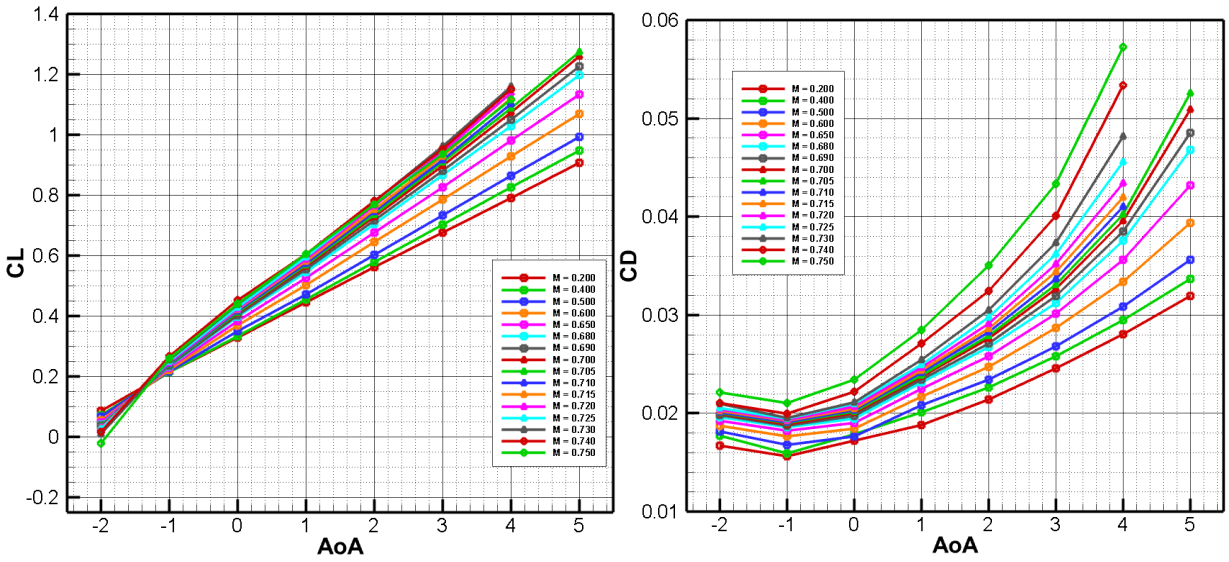

(a) Lift (b) Drag

Figure 4.26: Configuration 3 NSU3D-SA-AFT2 Free Transition Force Coefficient Curves with Free Transition Applied to Only the Wing

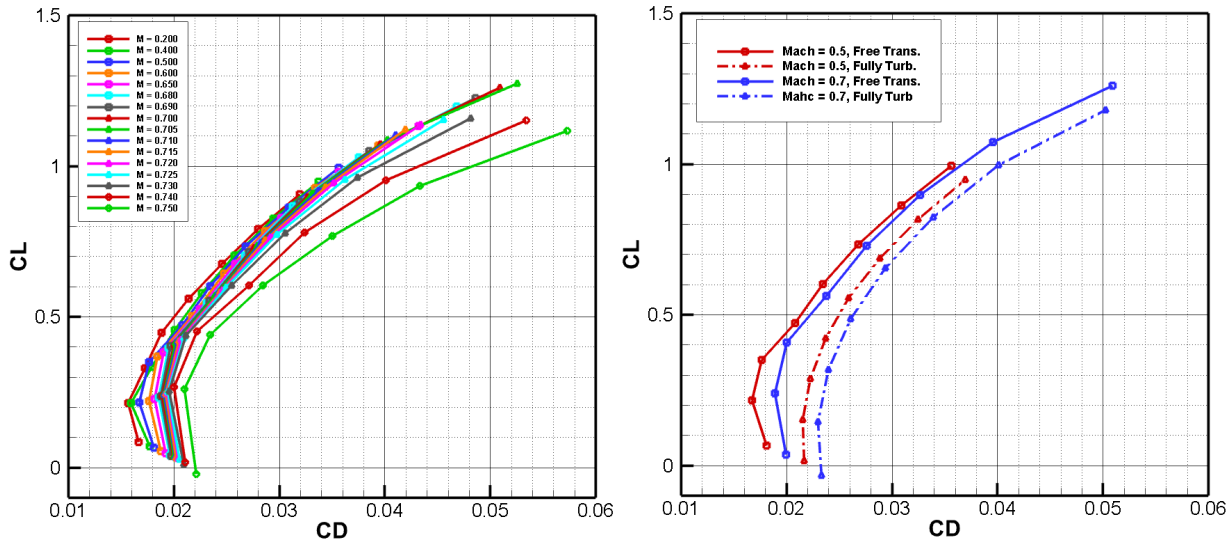

(a) All Simulations (b) Fully Turbulent Comparison

Figure 4.27: Configuration 3 NSU3D-SA Fully Turbulent Drag Polars with SA-AFT2 Free Transition Applied to Only the Wing

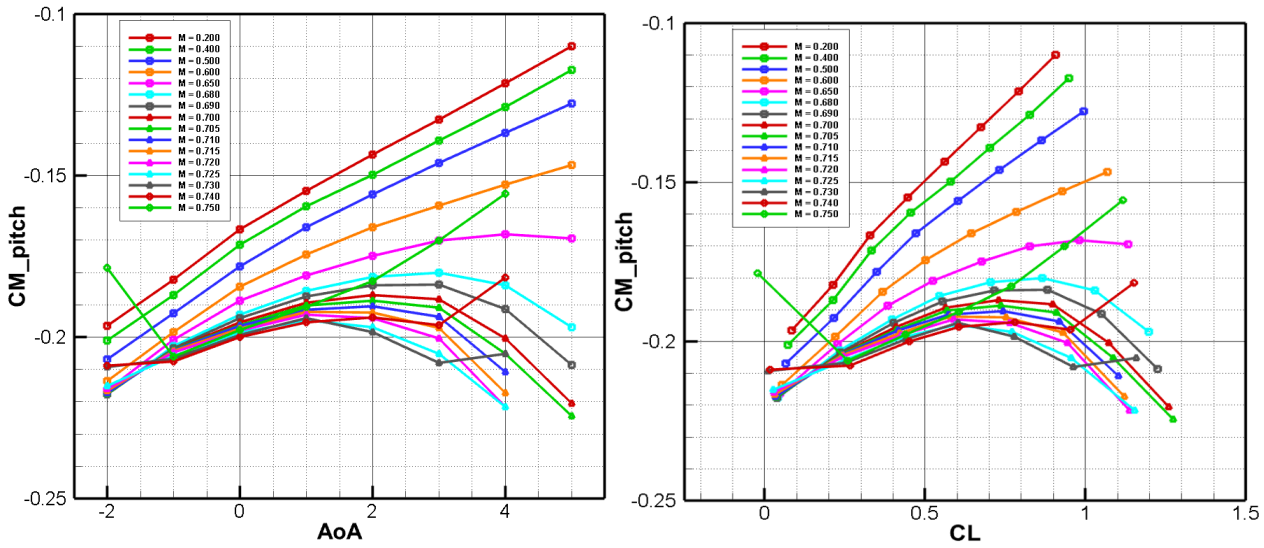

(a) Function of AOA

(b) Function of C_L

Figure 4.28: Configuration 3 NSU3D-SA Fully Turbulent Pitching Moment Curves with SA-AFT2 Free Transition Applied to Only the Wing

4.6 Additional 3D Free Transition Investigation with Configuration 3

Section 3.3 describes an investigation conducted to study the location of the transition line on the S207 airfoil as it relates to the freestream turbulence intensity. Freestream turbulence values of 0.02% (N_{crit}=12.0) to 0.04% (N_{crit}=10.34) were found to be most successful in establishing correspondence between NSU2D CFD solutions and original design values acquired using MSES [10]. In this section, the effect of freestream turbulence intensities of performance prediction is expanded to three dimensions via the development of a single polar for Configuration 3 at a Mach number of 0.7273, a MAC-based Reynolds number of 12.3 million, and a N_{crit} value of 10.4. Note that this N_{crit} is approximately equal to a freestream turbulence intensity value of 0.04%. The upper and lower surface skin friction drag contours for these polar simulations are included in Figure 4.37 and Figure 4.38, respectively. These solutions show laminar flow on the nose of the aircraft as the transition prediction model was applied to the entire body. However, it can be assumed the presence of this laminar flow on the nose does not impact the flow regime on the wing given the results from the study asso-

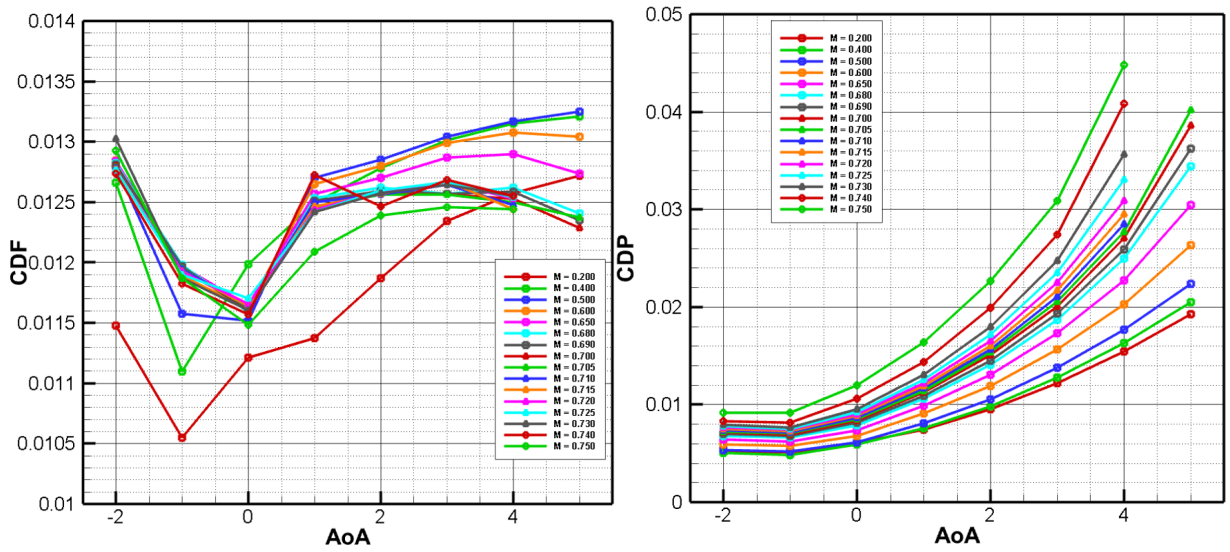

(a) Friction Drag (b) Pressure Drag

Figure 4.29: Configuration 3 NSU3D-SA Fully Turbulent Drag Profiles with SA-AFT2 Free Transition Applied to Only the Wing

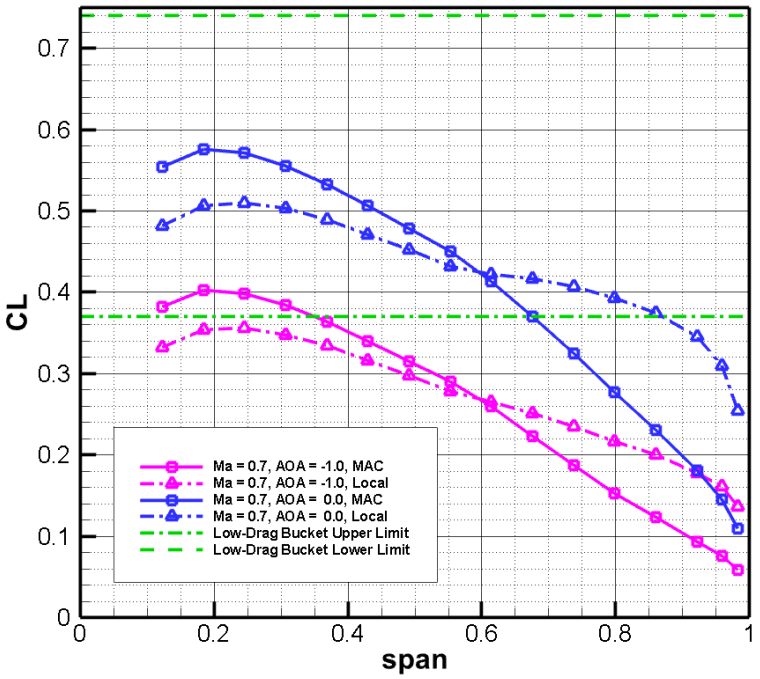

Figure 4.30: Configuration 3 NSU3D-SA Fully Turbulent Spaniwse Lift Distributions with SA-AFT2 Free Transition Applied to Only the Wing

ciated with Figure 4.20 and described in Section 4.4. Comparing the results for a N_{crit} value of 10.4 to Figure 4.18 and Figure 4.19 suggests once again that the freestream turbulence intensity value of roughly 0.04% predicts behavior that is more in line with design intent for the S207 airfoil compared to a freestream turbulence intensity value of 0.07%. Particularly, the transition line that seems to bleed out from the wing-fairing junction is not observed until an angle of attack of 1°, as opposed to an angle of attack of 0° when the freestream turbulence intensity is 0.07%.

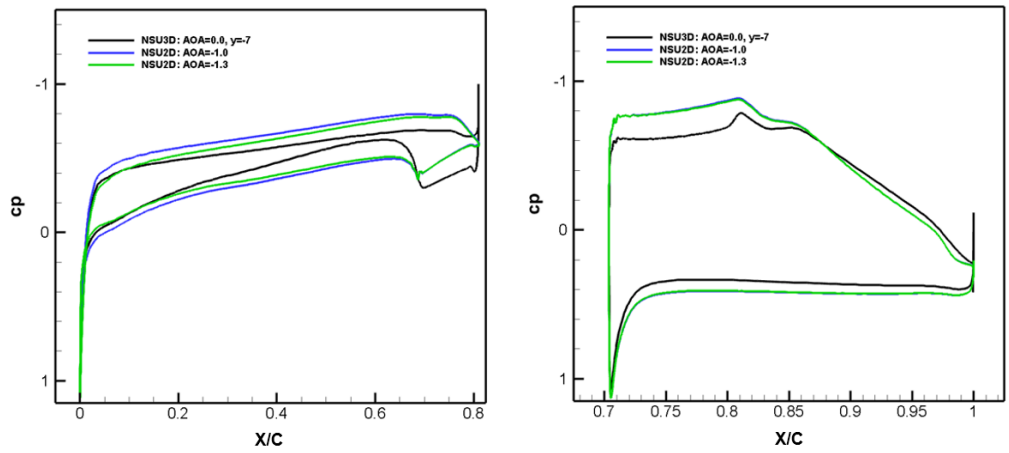

(a) 8.6% Span

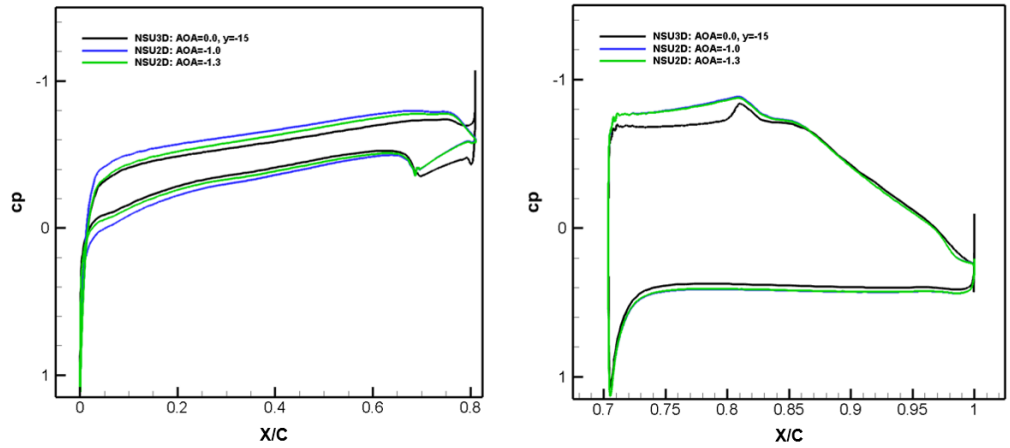

(b) 18.4% Span

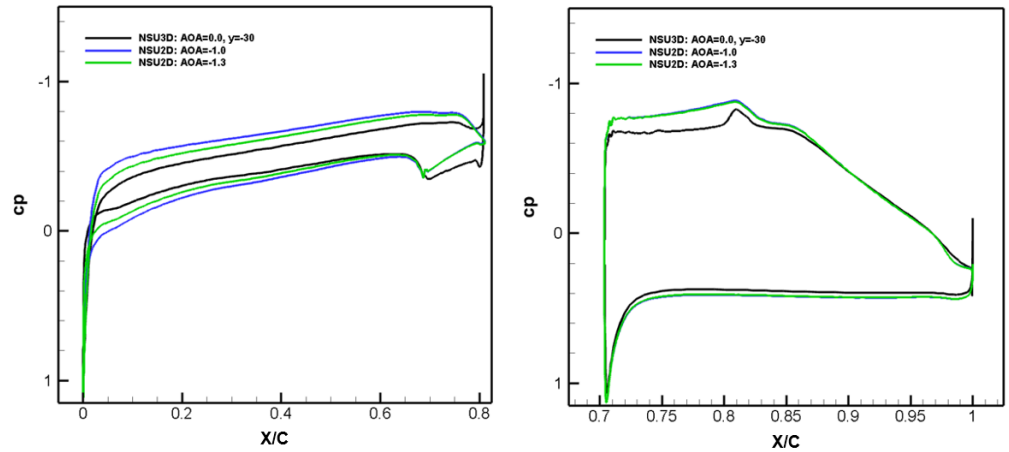

(c) 36.9% Span

Figure 4.31: Configuration 3 NSU3D-SA Spanwise Surface Pressure Profiles at Mach = 0.7, Re = 12.3x10^6 Compared to NSU2D-SA Surface Pressure at Mach = 0.7, Re = 13.2x10^6

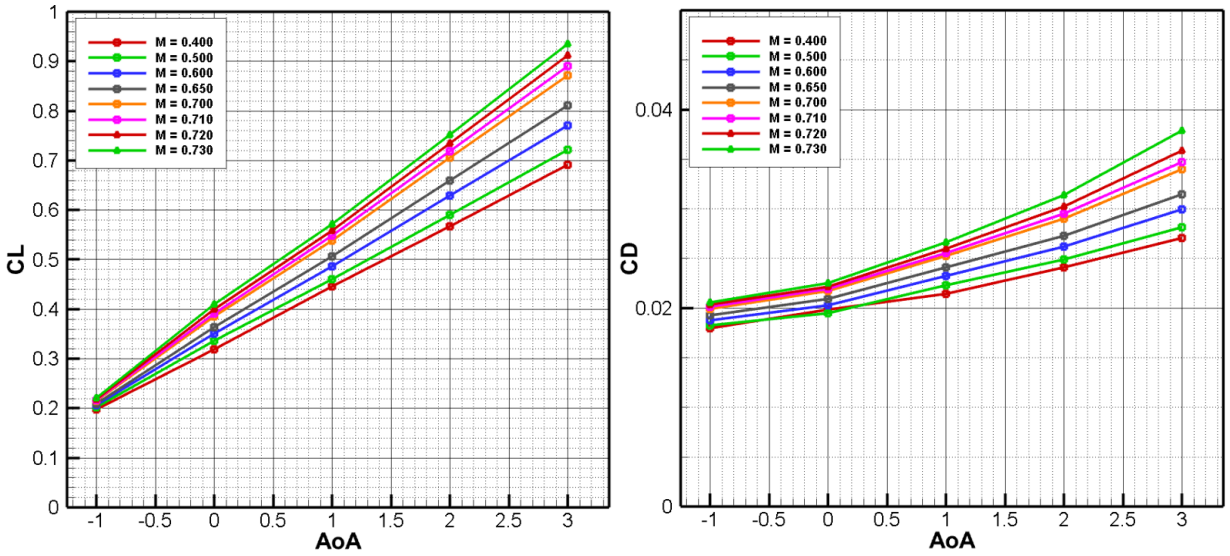

(a) Lift (b) Drag

Figure 4.32: Configuration 3 NSU3D-SA Fully Turbulent Force Coefficient Curves with SA-AFT2 Transition Applied Partially to the Wing

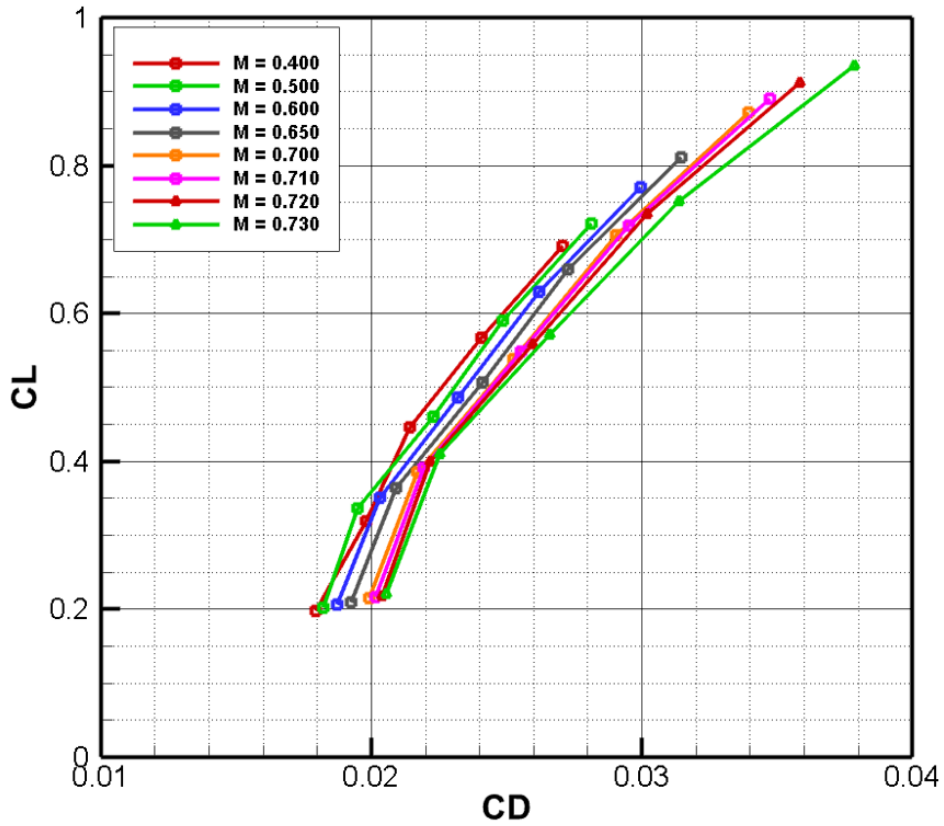

Figure 4.33: Configuration 3 NSU3D-SA Fully Turbulent Drag Polars with SA-AFT2 Free Transition Applied Partially to the Wing

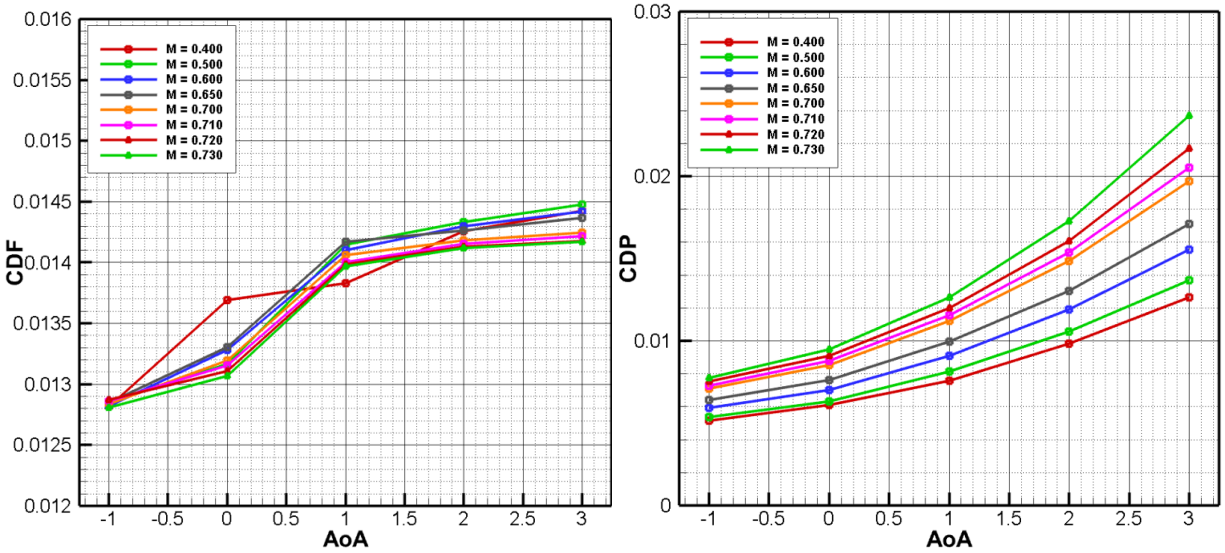

(a) Friction Drag (b) Pressure Drag

Figure 4.34: Configuration 3 NSU3D-SA Fully Turbulent Drag Profiles with SA-AFT2 Free Transition Applied Partially to the Wing

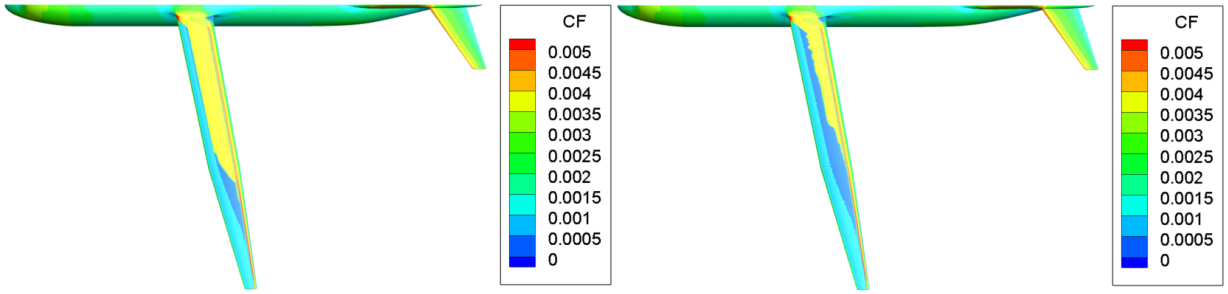

(a) Mach = 0.400 (b) Mach = 0.500

Figure 4.35: Configuration 3 NSU3D-SA Fully Turbulent Skin Friction Drag Profiles with SA-AFT2 Free Transition Applied Partially to the Wing at AOA = 0° at Re = 12.3x10^6

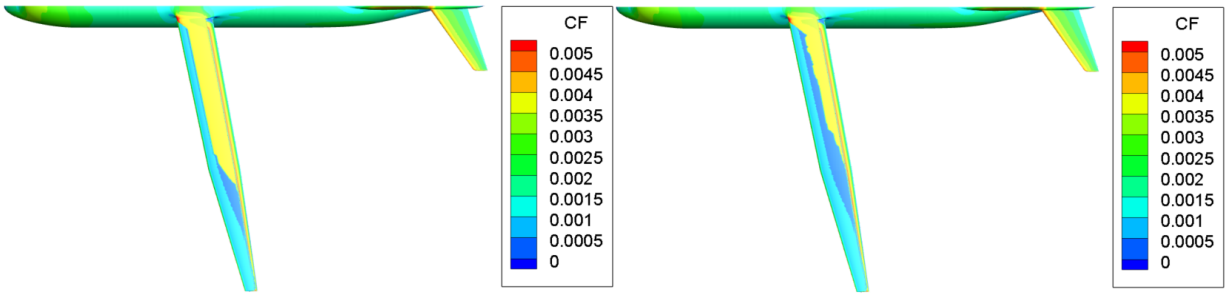

(a) Mach = 0.400 (b) Mach = 0.500

Figure 4.36: Configuration 3 NSU3D-SA Fully Turbulent Skin Friction Drag Profiles with SA-AFT2 Free Transition Applied to Entire Wing at AOA = 0° at Re = 12.3x10^6

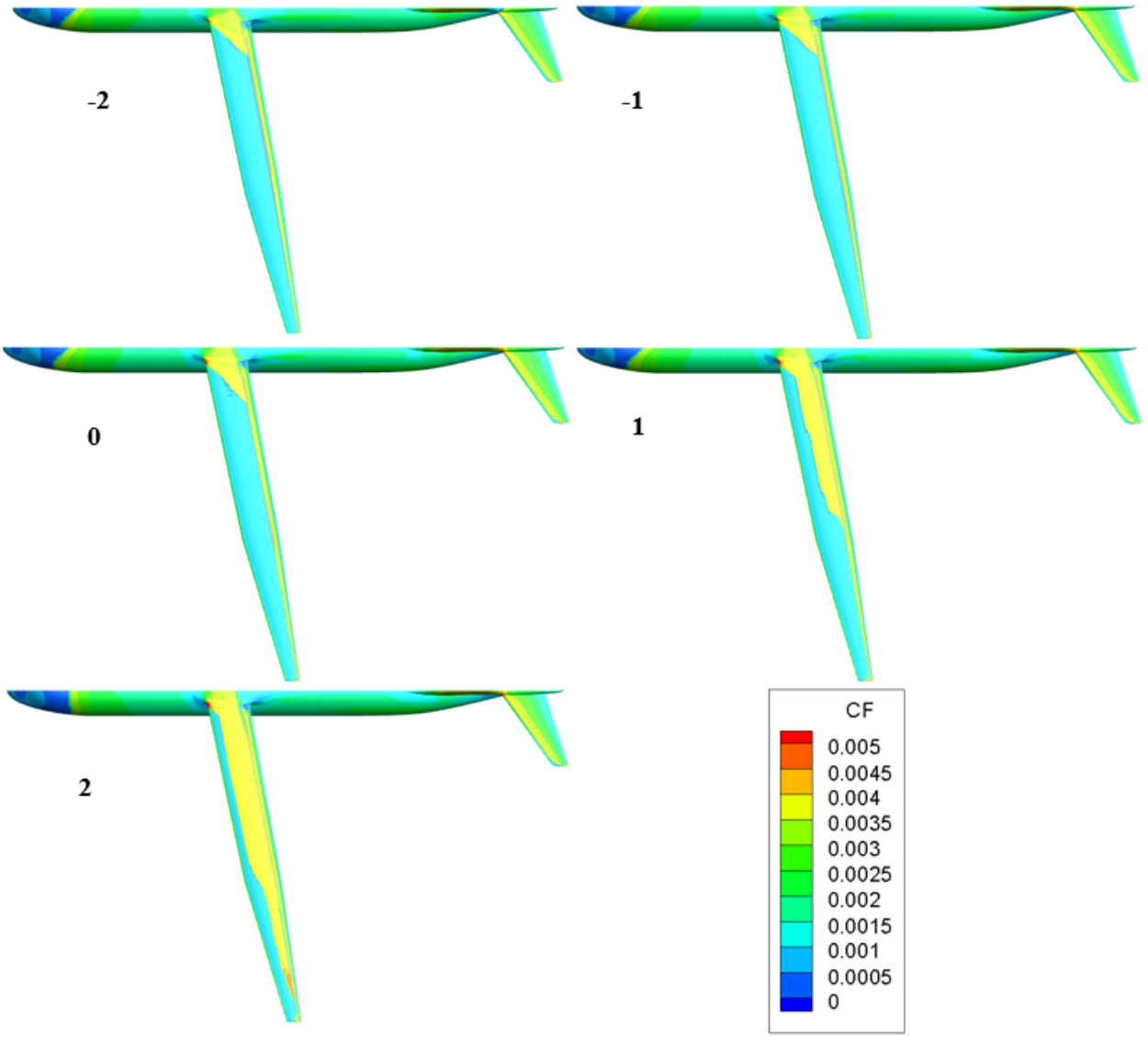

Figure 4.37: Configuration 3 NSU3D-SA-AFT2 Free Transition Upper Surface Skin Friction Drag Contours at Mach = 0.7273, Re = 12.3x10^6, and N_{crit} = 10.4

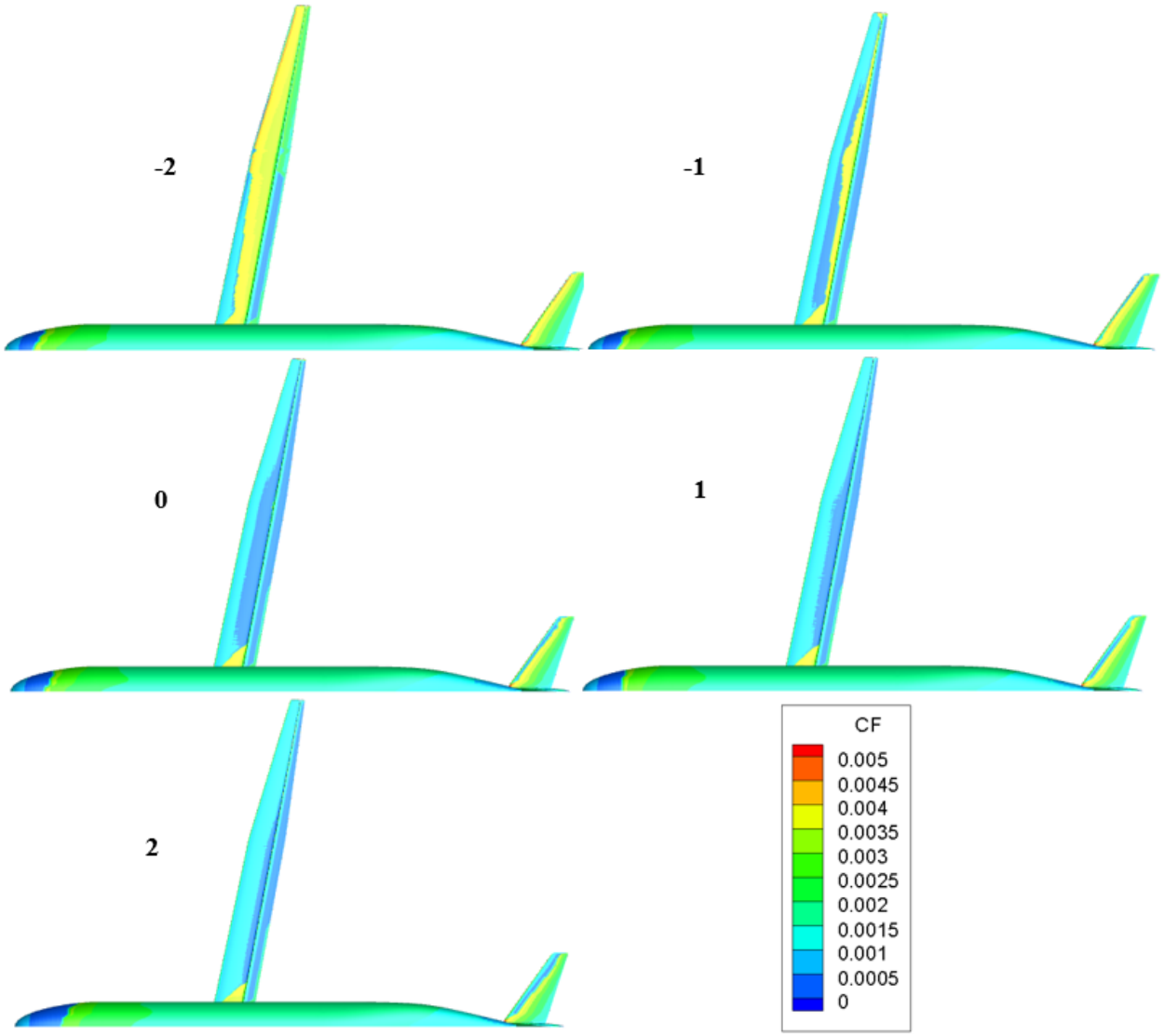

Figure 4.38: Configuration 3 NSU3D-SA-AFT2 Free Transition Lower Surface Skin Friction Drag Contours at Mach = 0.7273, Re = 12.3x10^6, and N_{crit} = 10.4

Chapter 5

Computational Results for a S207 Wind Tunnel Model

5.1 The NASA Ames Wind Tunnel Tests

Efforts conducted under the NASA ULI to thoroughly establish the benefits of SNLF technology and set forth the S207 as a superior foundation for commercial aircraft included a capstone demonstration performed in the NASA Ames UWPT 11-ft transonic wind tunnel in Febuary and March of 2022. A main consideration of the experimental campaign was to determine if desired regions of natural laminar flow could be maintained on an S207-based model with moderate sweep and the necessary bracketing hardware to connect the fore and aft element. The sweep of this S207-based model was 12.5°, and the chord was a constant 2ft. Three connectors attached the aft element to the fore element and enabled aft element repositioning for high-lift configurations. Three rows of pressure ports were installed at inboard, midboard, and outboard locations. A diagram summarizing the construction of the model can be viewed in Figure 5.1. The completed installation in the wind tunnel is included as Figure 5.2.

The model was painted matte black in anticipation of infrared (IR) thermography analysis. Figure 5.3a shows an image acquired using this methodology visualizing the flow on the upper surface near the fairing at a Mach number of 0.699, an angle of attack of -0.002, and

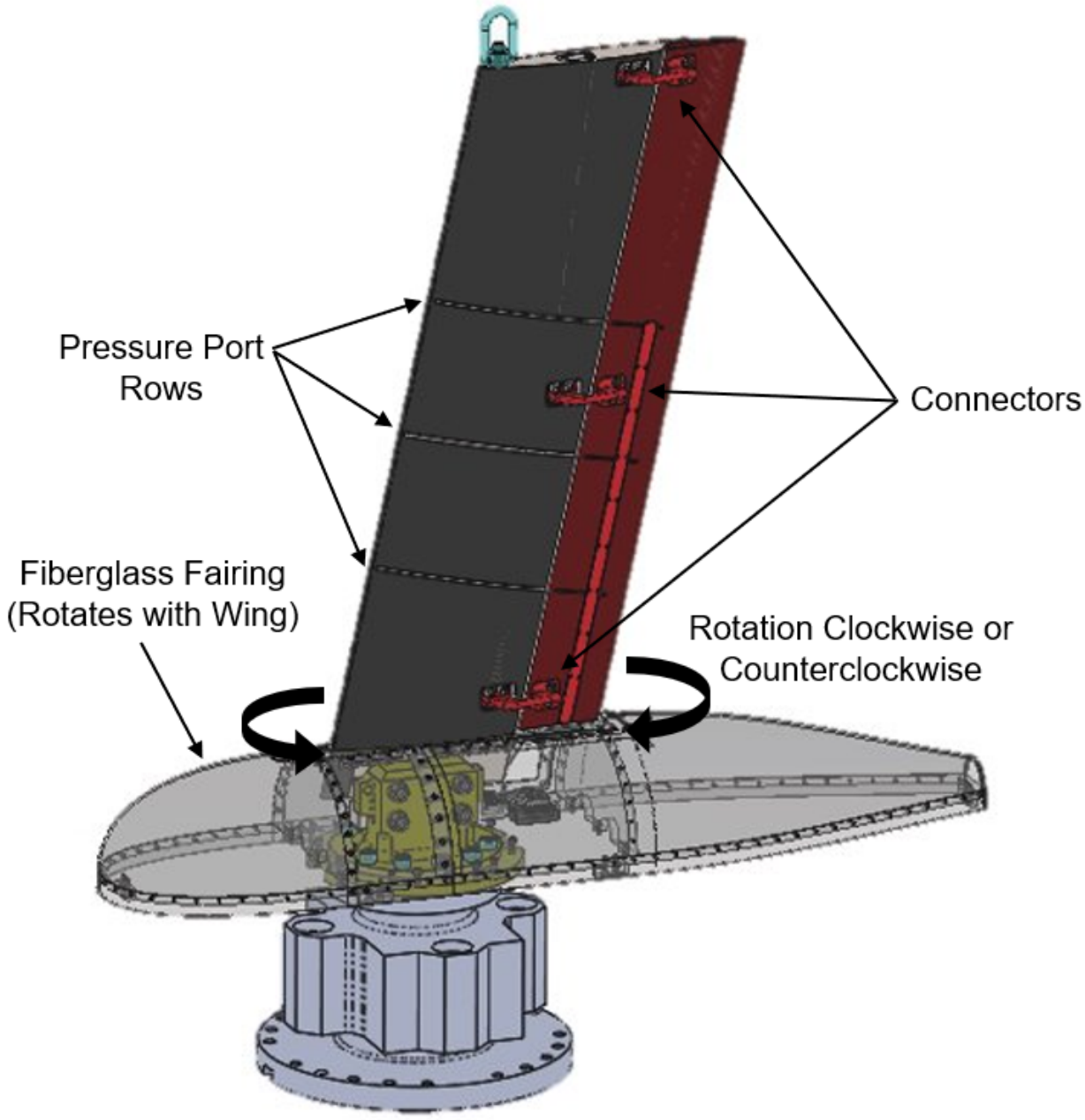

Figure 5.1: Wind Tunnel Model Construction Diagram

Figure 5.2: Wind Tunnel Model Installation Photograph

a Reynolds number of 12.93 million. Similarly, Figure 5.3b shows the flow at this location for a Mach number of 0.701, an angle of attack of -1.000°, and a Reynolds number of 12.95 million. Distinct transition lines produced by the pressure port rows are observed in Figure 5.3b. In comparison, Figure 5.3a shows no indication of transition, suggesting that laminar flow is present for the entirety of the upper surface of the wing at these flow conditions. These results confirm that the configuration produces large regions of natural laminar flow and thus behaves as intended according to design. Additionally, results suggest that any cross flow instabilities resulting from the 12.5° of sweep are not significant enough to induce transition for angles of attack of 0° and -1°.

5.2 Wind Tunnel Model Grid

The wind tunnel campaign was supported with CFD simulations completed on a wind tunnel model representative of the experimental setup. The grid was generated by collaborators at the University of Tennessee at Knoxville using the Pointwise software. The mesh is unstructured with 168,877,277 nodes, and it is hybrid with prisms in the near-wall boundary layer and pyramids and tetrahedral elements in the regions of inviscid flow. The mesh of the wing-fairing structure is shown in Figure 5.4 and is accompanied by additional images of the wing-fairing junction to emphasize the refinement through the slot.

The wing-fairing structure is placed in a channel 84.7 chord lengths from inlet to outlet. The inlet and outlet are square being 5.36 chord lengths in width and length. The nose of the fairing is a distance of 5.33 chord lengths from the inlet. Diagrams of the full channel are shown in Figure 5.5.

5.3 Results for Initial Simulations

The first simulation performed using the wind tunnel model grid utilized a fully turbulent approach. This was done to both establish a successful run prior to introducing the complexities associated with transition prediction, and to gain insight on the computational

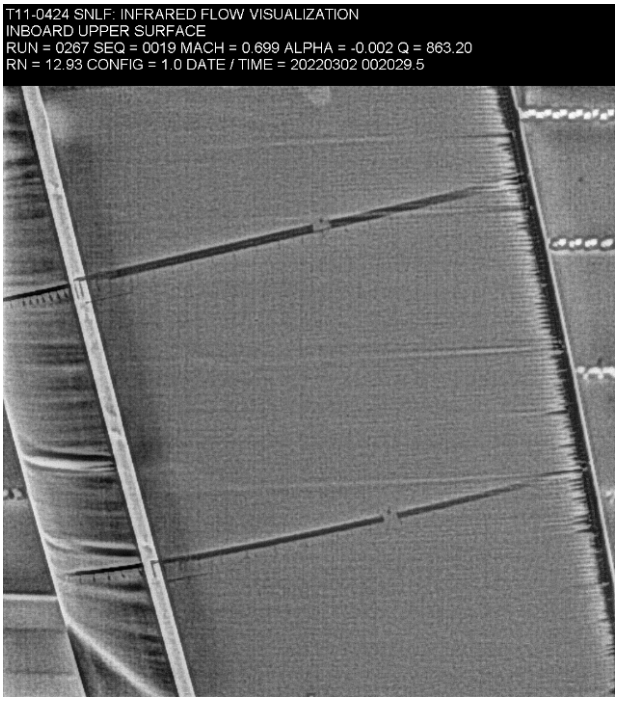

(a) Mach=0.699, AOA=-0.002,Re=12.93x10^6

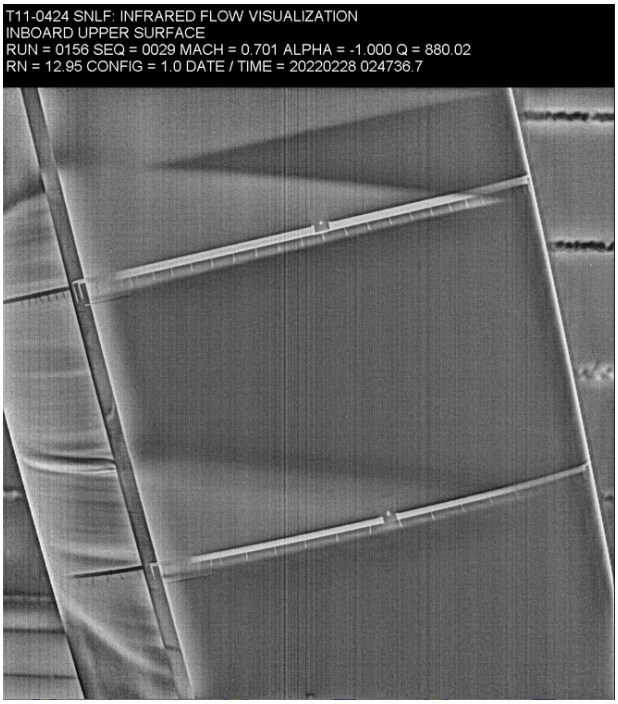

(b) Mach=0.701, AOA=-1.000,Re=12.95x10^6

Figure 5.3: IR Images of Right to Left Moving Flow on the Upper Surface of the Wing Near the Fairing with Evident Transition Lines for AOA = -1.000°

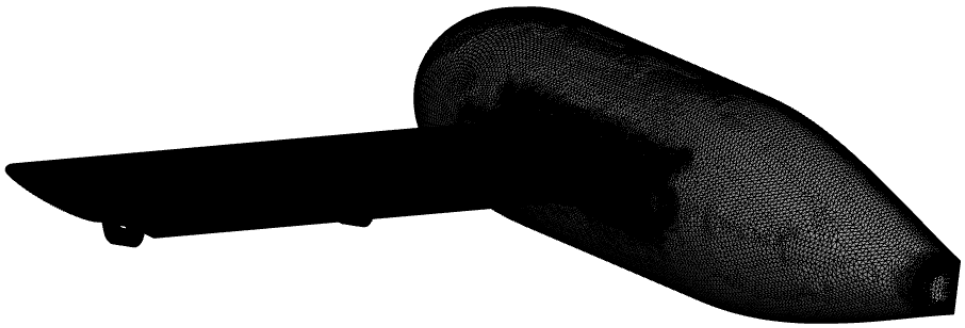

(a) Wing-Fairing Model

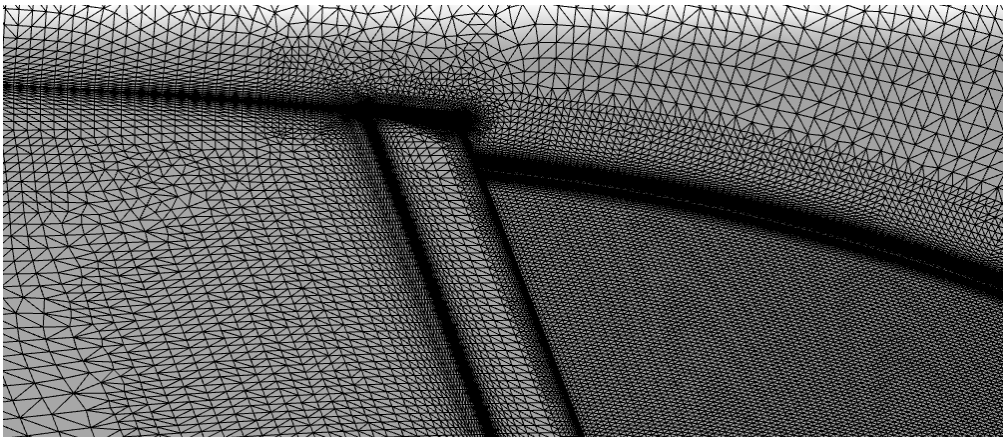

(b) Wing-Fairing Junction

(c) Slot at Wing-Fairing Junction

Figure 5.4: Wind Tunnel Model Computational Mesh

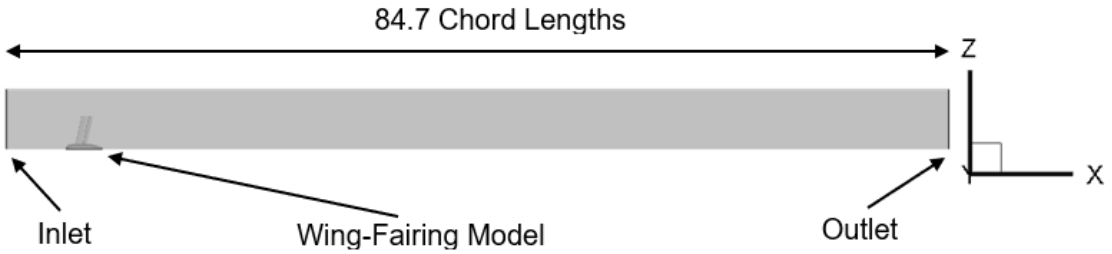

(a) Full Channel

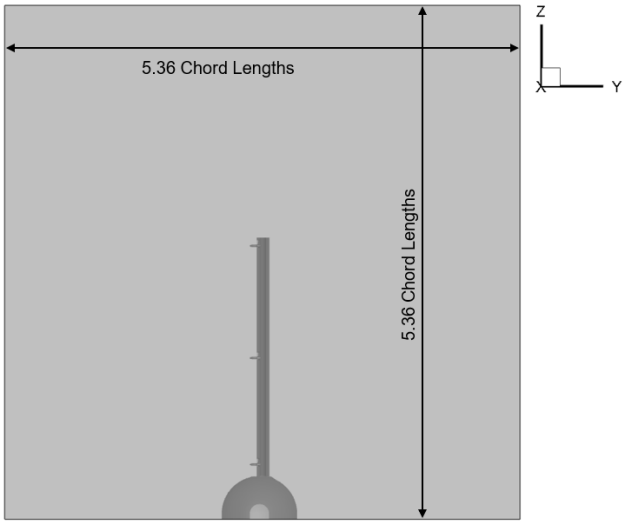

(b) Channel Inlet View

Figure 5.5: Wind Tunnel Channel Specifications

requirements for this grid, given its size. This simulation was run at a Mach number of 0.7, an angle of attack of 0°, and a Reynolds number of 12 million. The CL and CD values were computed to be 0.3611 and 0.0335, respectively. The convergence history over 10000 cycles for CL and the density residual are shown in Figure 5.6. It is apparent from this plot that this grid requires a large number of cycles to arrive at a converged solution. This behavior can be expected to be more severe when a transition prediction model is used.

In anticipation of the increased computational demands associated with the transition prediction model and to ensure that adjusting the CFL number would not drastically impact the transition location when utilizing a free transition model, a numerical effort was undertaken in which three free transition simulations, using the AFT2 model, were completed

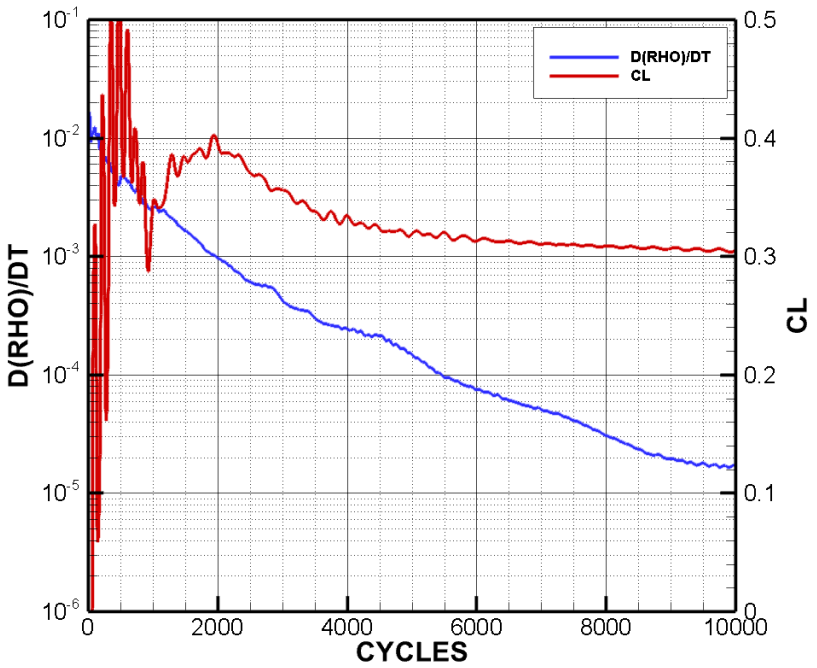

Figure 5.6: NSU3D-FT Wind Tunnel Model Solution at Mach=0.7, AOA=0, Re=12x10^6

with varying CFL numbers. These simulations are denoted as Simulation 1, Simulation 2, and Simulation 3. It became clear immediately following initial runs that a solution started from uniform freestream conditions would numerically diverge if the CFL number was set to a value greater than 2. The decision was made to run a single free transition simulation for 10000 cycles using a CFL number of 2 that would then be used to start the three desired solutions with varying CFL numbers. This simulation is denoted as Baseline. All solutions, Simulations 1, 2, 3, and Baseline, used an N_{crit} value of 8.4, which as mentioned in Section 2.1 is a parameter of the transition model. No longer being started from a uniform freestream solution, the CFL number for Simulation 1 was set to 10 and the CFL number for Simulation 2 was set to 25. Both of these cases were ran for an additional 10000 cycles. Simulation 3 experienced no increase in CFL number and was instead ran for another 32000 iterations at a CFL number of 2. Table 5.1 more compactly summarizes each case and their specifications along with corresponding computed force coefficient values. Figure 5.7 shows the CL and density residual convergence histories. It should be noted that the residuals in NSU3D are scaled by the CFL number, so the increase in the density residuals observed for Simulations 1 and 2 in Figure 5.7b does not indicate undesirable convergence. However,

the residual for Simulation 2 increases over 5000 cycles which is not ideal or desirable, and running for longer than 10000 additional cycles defeated the purpose of the cost reduction benefits expected with the increase in CFL.

Each of the three simulations computed roughly the same C_L value of ≈0.32. This is an indication that altering the CFL number does not significantly impact the final solution values. To further support this claim and to investigate the behavior of the transition line as each simulation evolved, skin friction contours were made at various stages of each solution. Figure 5.8 shows the upper and lower skin friction profiles at the end of the Baseline simulation. In this case, both the upper and lower surface show laminar flow along the entire chord length of the wing with some turbulence near the fuselage and wingtip. Skin friction contours for the upper and lower surface of the wing at the end of Simulation 1 and Simulation 2 are shown in Figure 5.9 and Figure 5.10, respectively. Simulation 3 skin friction contours were made for solutions at 18000 cycles (28000 total if including Baseline) and at the end cycle of 32000 (42000 total if including Baseline). These are shown for the upper and lower surfaces in Figure 5.11.

Table 5.1: NSU3D-SA-AFT2 Wind Tunnel Model Simulations Performed at Mach = 0.7, AOA = 0, Re = 12x10^6, and N_{crit} = 8.4

Case	CFL	Initial Condition	Total Cycles	CL	CD
Baseline	2	Freestream	10000	0.4260	0.02947
Simulation 1	10	Baseline	10000	0.3230	0.02715
Simulation 2	25	Baseline	10000	0.3214	0.02731
Simulation 3	2	Baseline	32000	0.3254	0.02696

Simulations 1, 2, and 3 show that the transition line moves, albeit very slowly, toward the leading-edge of the fore element as the solution converges. These simulations also predict the transition line to become stationary at approximately 40% the chord length, demonstrating that the steady-state transition line is predicted at roughly the same location by all runs with different CFL values, provided these cases are run for sufficient number of cycles. These results depict much more significant regions of turbulent flow in comparison to wind tunnel data discussed in Section 5.1.

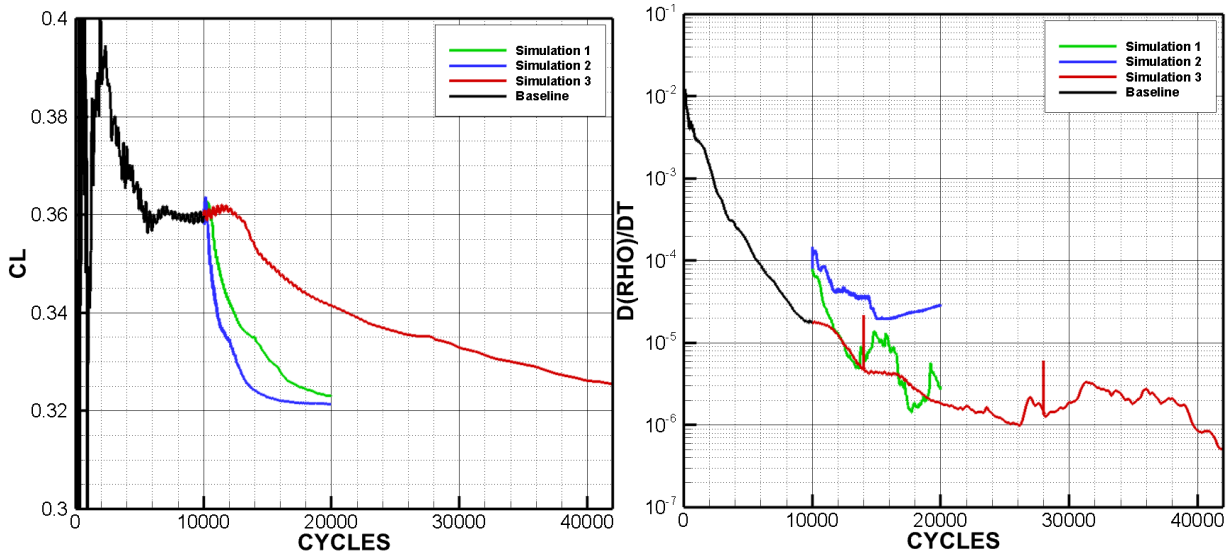

(a) CL History (b) Density Residual History

Figure 5.7: NSU3D-SA-AFT2 Wind Tunnel Model Simulation Histories at Mach = 0.7, AOA = 0, Re = 12x10^6, and N_{crit} = 8.4

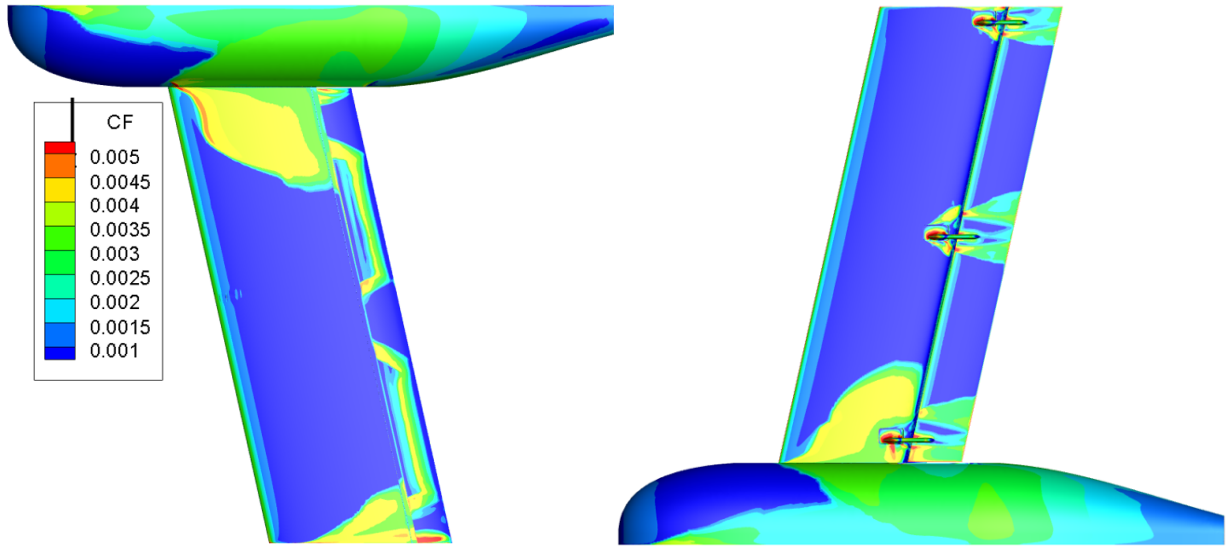

(a) Upper Surface (b) Lower Surface

Figure 5.8: NSU3D-SA-AFT2 Skin Friction Distribution for Baseline solution at Mach = 0.7, AOA = 0, Re = 12x10^6, and N_{crit} = 8.4

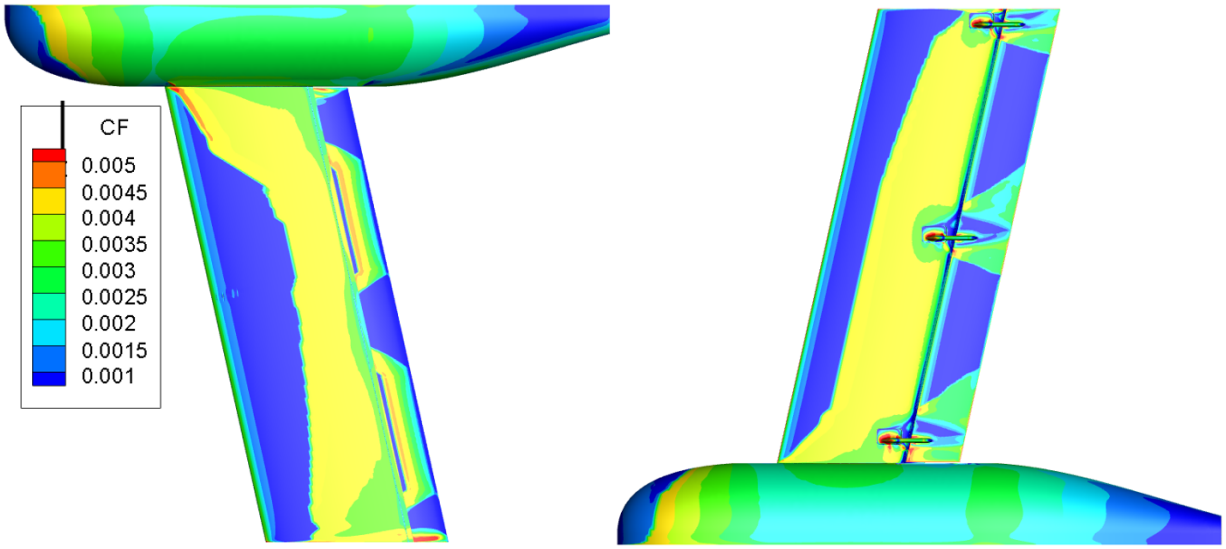

(a) Upper Surface (b) Lower Surface

Figure 5.9: NSU3D-SA-AFT2 Skin Friction Distribution for Simulation 1 at Mach = 0.7, AOA = 0, Re = 12x10^6, and N_{crit} = 8.4

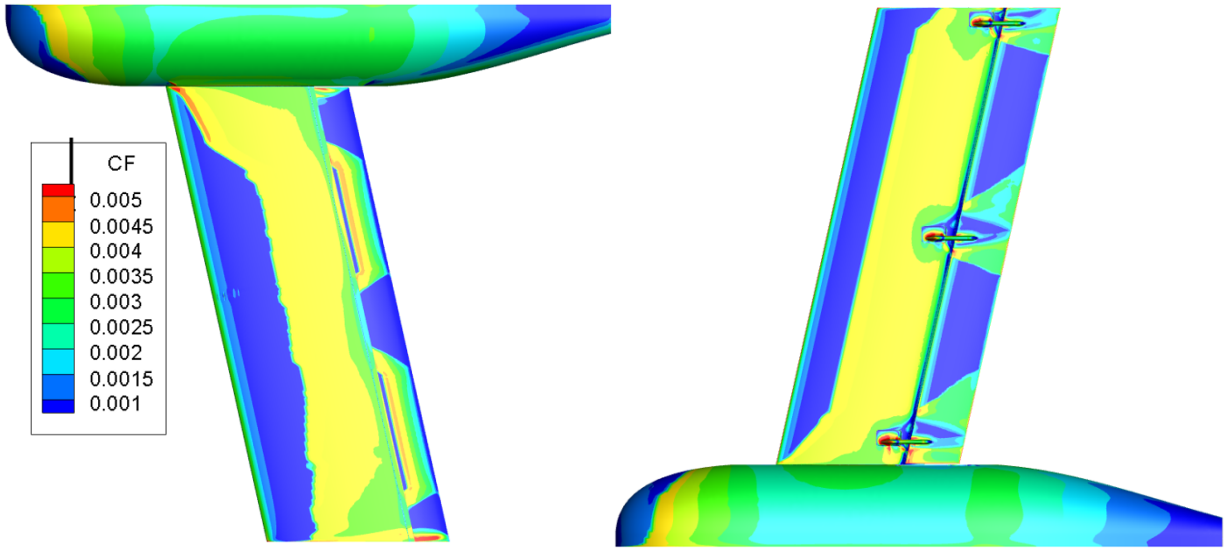

(a) Upper Surface (b) Lower Surface

Figure 5.10: NSU3D-SA-AFT2 Skin Friction Distribution for Simulation 2 at Mach = 0.7, AOA = 0, Re = 12x10^6, and N_{crit} = 8.4

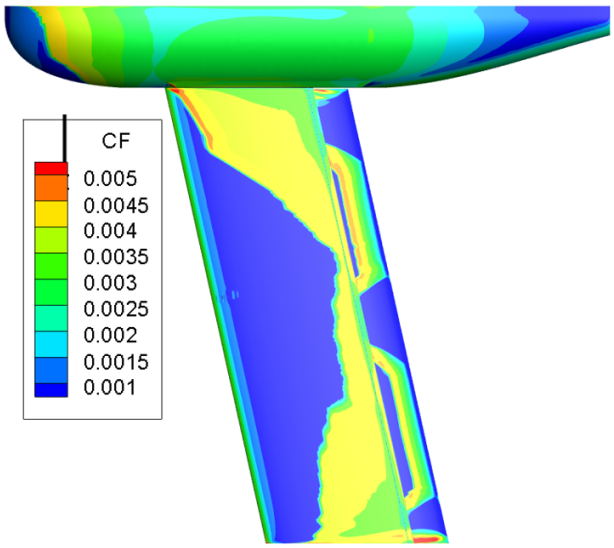

(a) Upper Surface at 18000 Cycles

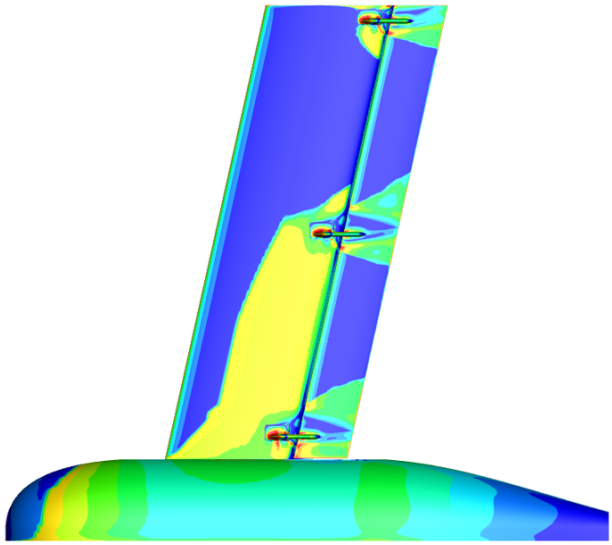

(b) Lower Surface at 18000 Cycles

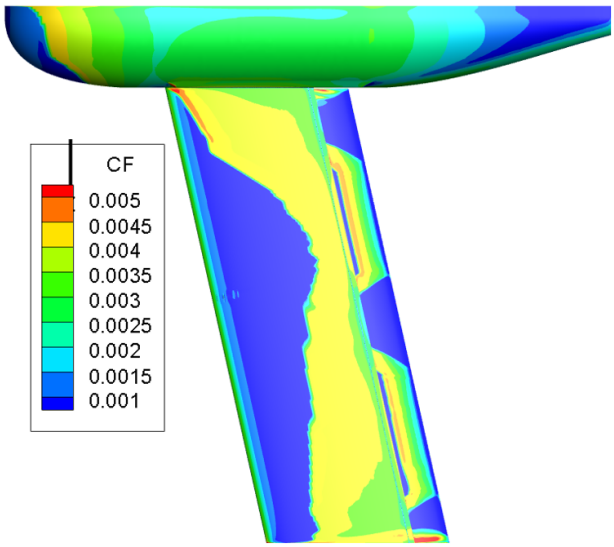

(c) Upper Surface at 32000 Cycles

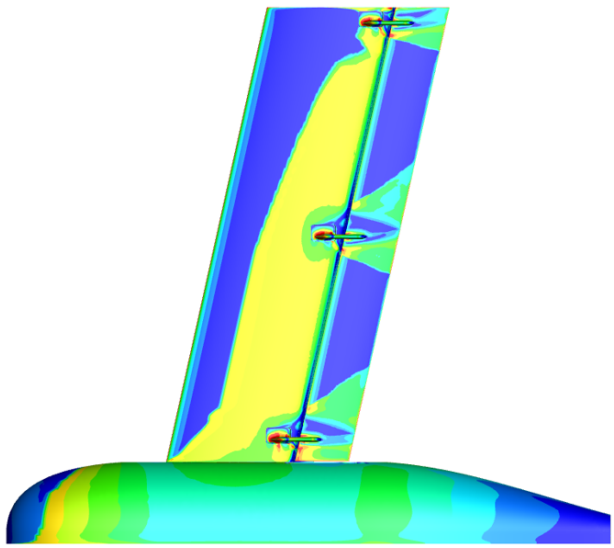

(d) Upper Surface at 32000

Figure 5.11: NSU3D-SA-AFT2 Skin Friction Distributions for Simulation 3 at Mach = 0.7, AOA = 0, Re = 12x10^6, and N_{crit} = 8.4

5.4 Results for N_{crit} of 6

Following the delivery of results presented in the previous section to the ULI team at the University of Tennessee at Knoxville, a request was made for an additional simulation with an N_{crit} value of 6. This value was chosen to more accurately represent expected wind tunnel freestream turbulence conditions. This simulation was ran at a Mach number of 0.7, a Reynolds number of 12 million, and an angle of attack of 0°. The CFL number was held at 2 to ensure the residuals did not begin to increase as was observed with Simulation 2, and 30000 cycles were executed. The convergence history for C_L and the density residual are shown in Figure 5.12. The C_L is computed to be 0.326 which is approximately equal to the value predicted by Simulations 1, 2, and 3, whose N_{crit} value was 8.4.

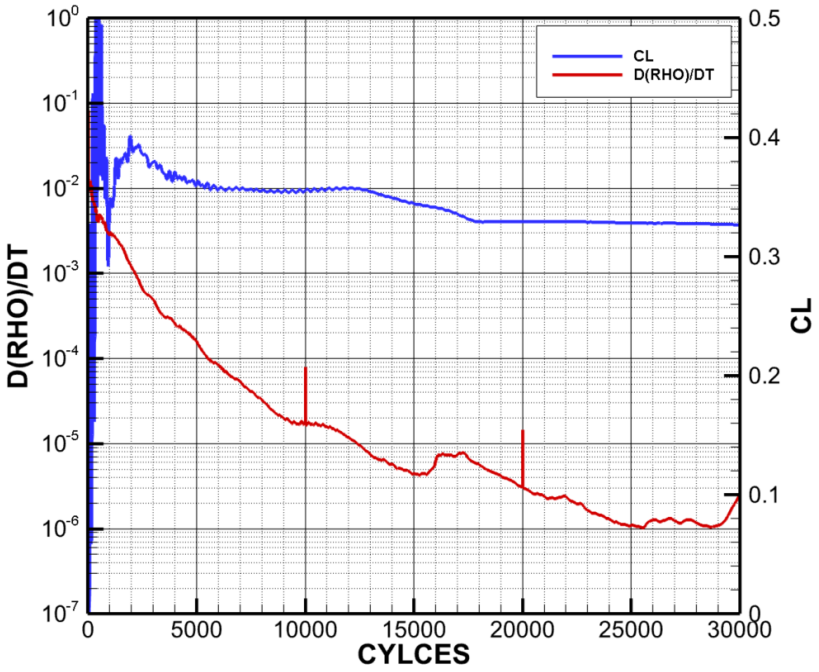

Figure 5.12: NSU3D-SA-AFT2 Wind Tunnel Model Solution at Mach=0.7, AOA=0, Re=12x10^6, and N_{crit}=6

Skin friction distribution contours were once again generated for various cycle numbers to evaluate the behavior of the transition line. Contours for the upper and lower surfaces are shown at 10000 cycles, 20000 cycles, and 30000 cycles in Figure 5.13. These skin friction contours show that when N_{crit} is set to 6 the transition line begins at the trailing-edge of the

fore element and moves toward the leading-edge, stopping at about 40% of the chord length, as the solution converged. This is similar to the behavior observed with Simulations 1, 2, and 3, but again is in disagreement with the extensive runs of laminar flow observed in the NASA Ames wind tunnel tests for these flow conditions.

To investigate the discrepancies between computational and experimental results further, surface pressure profiles collected at three experimental pressure port row locations, as shown in Figure 5.1, were compared to computational results. These pressure port row locations are denoted as L1 for the inboard location, L2 for the midboard location, and L3 for the outboard location. Data for two wind tunnel tests at approximately a Mach number of 0.7, a Reynolds number of approximately 13 million, and an angle of attack of roughly 0 were available for examination. They are denoted as Run 204 and Run 297, and their exact flow parameters are summarized in Table 5.2. Surface pressure data was post-processed and provided by ULI associates at Texas A&M University. Figure 5.14 illustrates the C_P profiles for both Run 204 and Run 297 plotted against the C_P profiles of the N_{crit}=6 solution at 10000 cycles and 30000 cycles. Figure 5.15 shows surface pressure contours across the upper and lower surfaces for the CFD solution at 10000 cycles and 30000 cycles appended with lines associated with the pressure port row locations.

Upon examination of Figure 5.14, it can be stated that the surface pressure profiles for the computational solution at 10000 cycles and 30000 cycles do not differ much with the exception of in the region of the slot and on the upper surface of the flap. Surprisingly, there are notable differences between the experimental runs. Run 297 has a lower, or more negative, pressure through the slot than Run 204 at all three locations. On the contrary, Run 204 has a lower pressure than Run 297 on the upper surface of the fore element at the trailing edge for all locations. This is also true on the upper surface of the aft element following the exit of the slot. If comparing the experimental and computational results, it is clear that the

Table 5.2: Flow Parameters for Examined Wind Tunnel Runs

Run	Mach	Reynolds Number	Angle of Attack
204	0.7013	12.95 Million	-0.0001
297	0.6994	12.93 Million	-0.0002

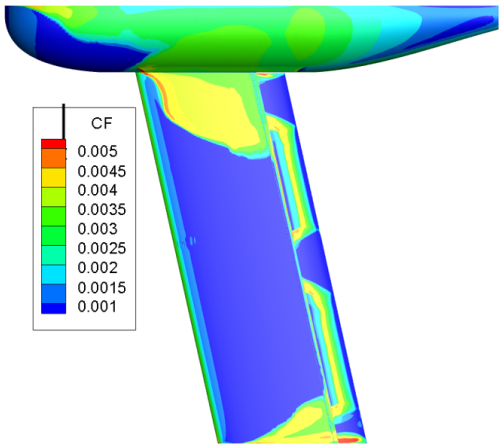

(a) Upper Surface at 10000 Cycles

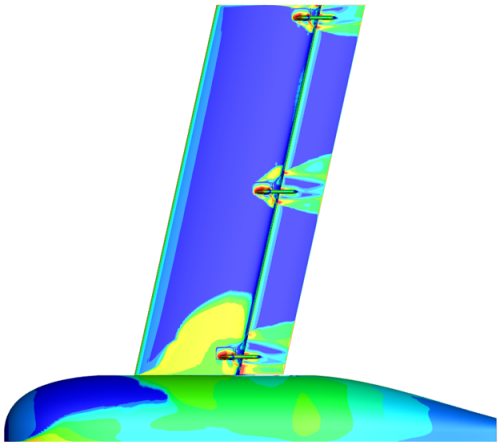

(b) Lower Surface at 10000 Cycles

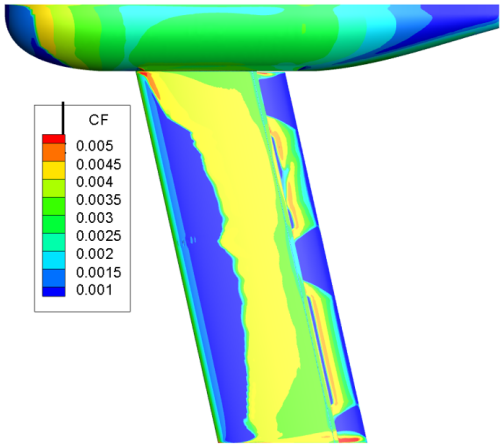

(c) Upper Surface at 20000 Cycles

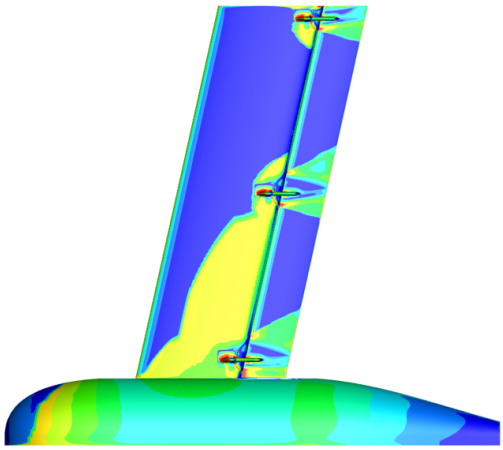

(d) Upper Surface at 20000

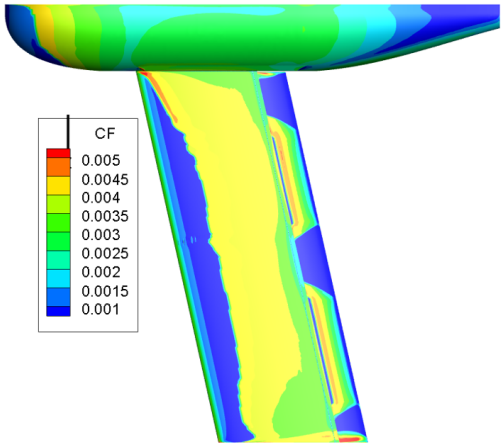

(e) Upper Surface at 30000 Cycles

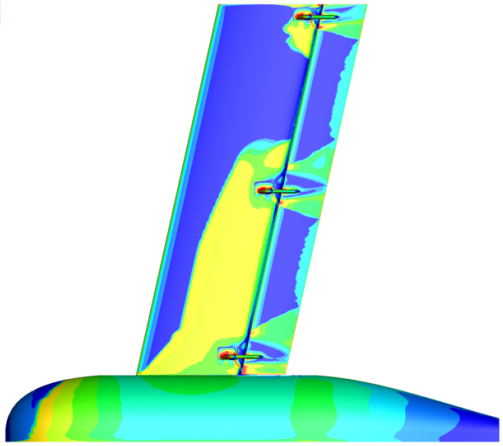

(f) Upper Surface at 30000

Figure 5.13: NSU3D-SA-AFT2 Skin Friction Distributions at Mach = 0.7, AOA = 0, Re = 12x10^6, and N_{crit} = 6.0

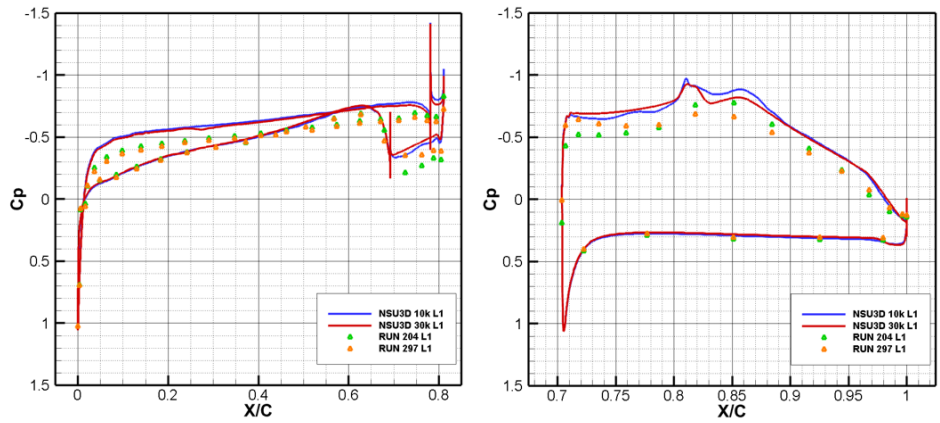

(a) Surface C_P Distributions at Inboard Pressure Port Location L1

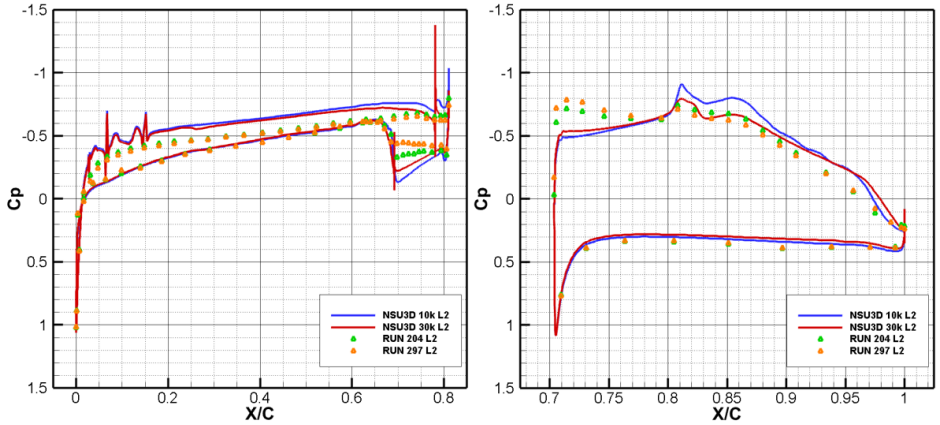

(b) Surface C_P Distributions at Midboard Pressure Port Location L2

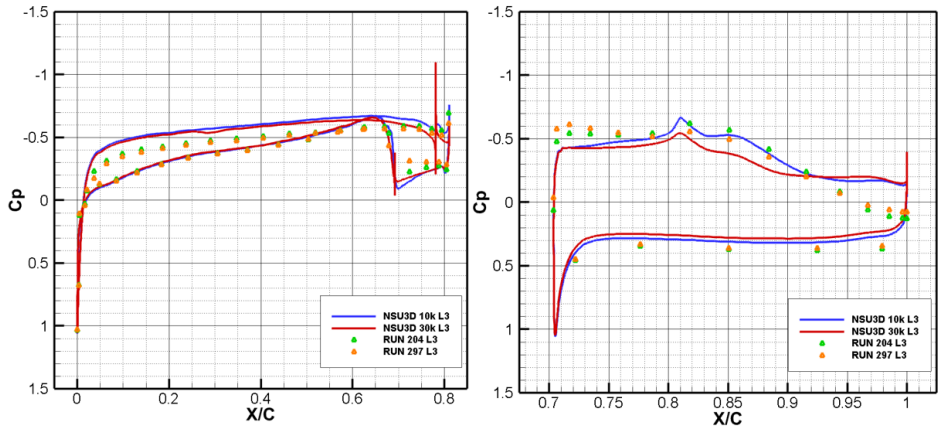

(c) Surface C_P Distributions at Outboard Pressure Port Location L3

Figure 5.14: NSU3D-SA-AFT2 vs. Ames Wind Tunnel Data Surface Pressure Distributions at at Mach = 0.7, AOA = 0

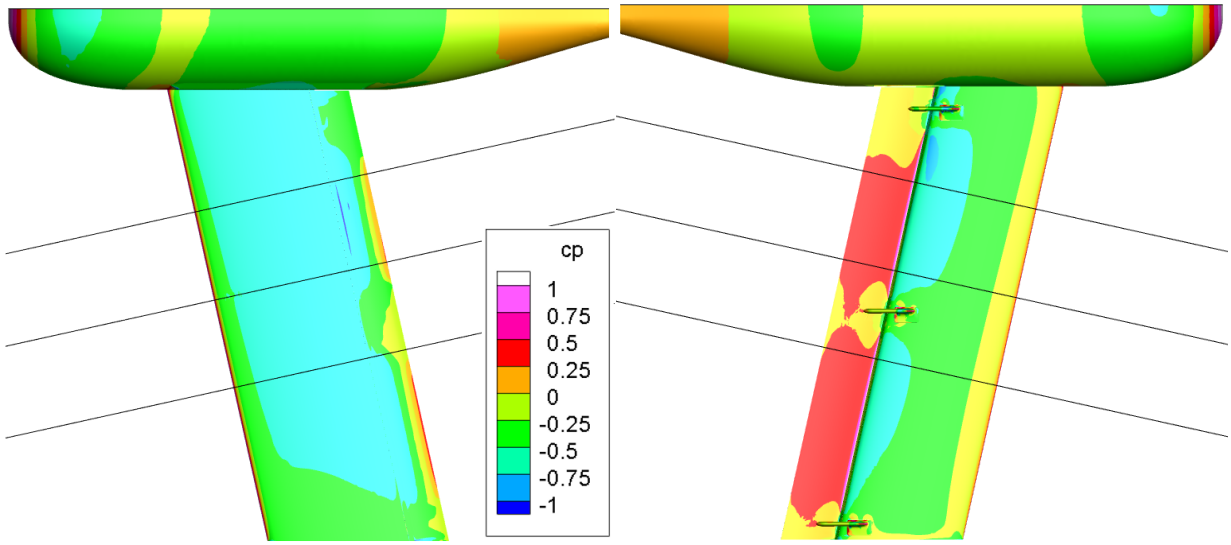

(a) Upper Surface at 10000 Cycles

(b) Lower Surface at 10000 Cycles

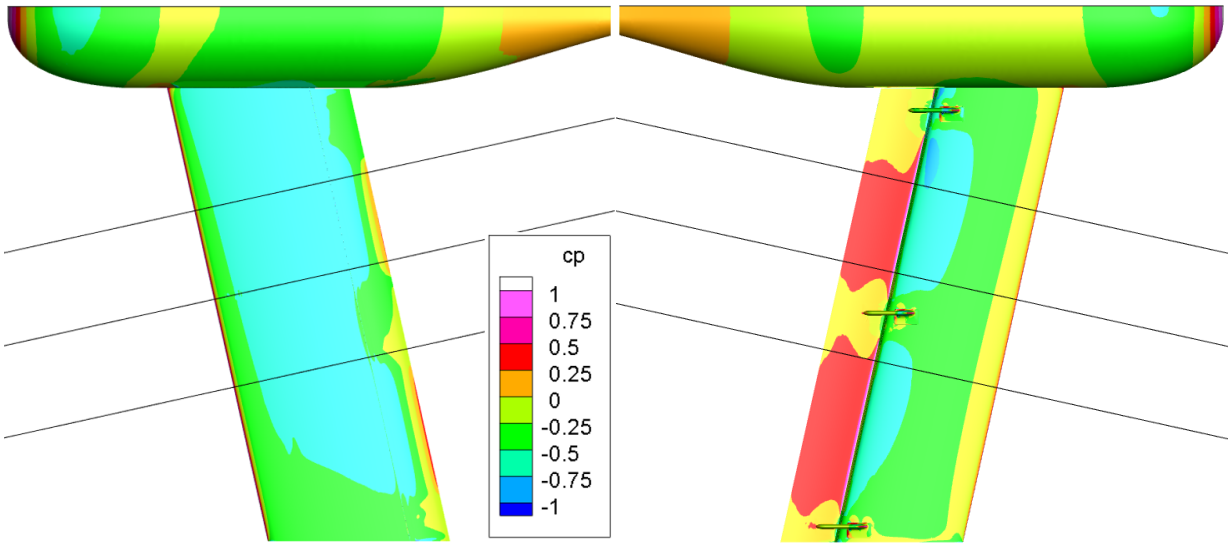

(c) Upper Surface at 30000 Cycles

(d) Lower Surface at 30000

Figure 5.15: NSU3D-SA-AFT2 Surface Pressure Distributions for Mach = 0.7, AOA = 0, Re = 12x10^6, and N_{crit} = 6

pressure on the upper surface of the fore element computed using CFD is lower across the entire surface at all three locations. Location L1 data shows that the computational results have a lower pressure through the slot. The opposite is true at locations L2 and L3, with experimental results having lower pressure through the slot. At the L3 outboard location, computational results agree well with Run 204, but not as well with Run 297. Additionally, the pressure profile on the upper surface at the trailing-edge of the aft element at the L3 location shows a pressure that is much lower than experimental results. It is relatively flat, indicating flow separation. Examination of Figure 5.15 offers evidence that this region of constant pressure starts just slightly outboard of the L2 pressure port row and continues just outboard of the L3 pressure port row. Similar regions of constant pressure are also observed at the trailing-edge near the fairing and at the trailing-edge of the wing tip. Large localized pressure variations, or spikes, are seen on the upper surface of the fore element at location L2. This was traced to the presence of non-smooth surface geometry as shown in Figure 5.16.

In summary, the computational results obtained in support of the wind tunnel tests conducted for a swept SNLF wing-fairing model showed several discrepancies. In particular, significantly more laminar flow was observed in the wind tunnel experiment than in the computational results. This may be due to the convergence difficulties that accompany the transition model used in the computational framework. There is also a possibility that undiscovered errors in the computational geometry are triggering transition earlier than desired. The current geometry did not account for the additional thickness accompanied by the paint layer as well. Given the sensitivity of SNLF technology to geometry, it is possible this lack of consideration may negatively impact the computational performance of the model. Acquiring a solution for the computational model using a different RANS solver could offer further insight into the differences in computational and experimental results as well. However, development of a structured grid for use in OVERFLOW, the other RANS solver available within the scope of current resources, was infeasible due to lack of remaining project timeline. Additionally, difference in the surface pressure profiles between Runs 204 and 297 suggest that there may be issues in the repeatability of the experiment, particularly

at the slot where small geometry changes greatly impact the flow. Furthermore, in the CFD, aeroelastic deformation was not taken into account, and there has been no assessment of what these deflections may be.

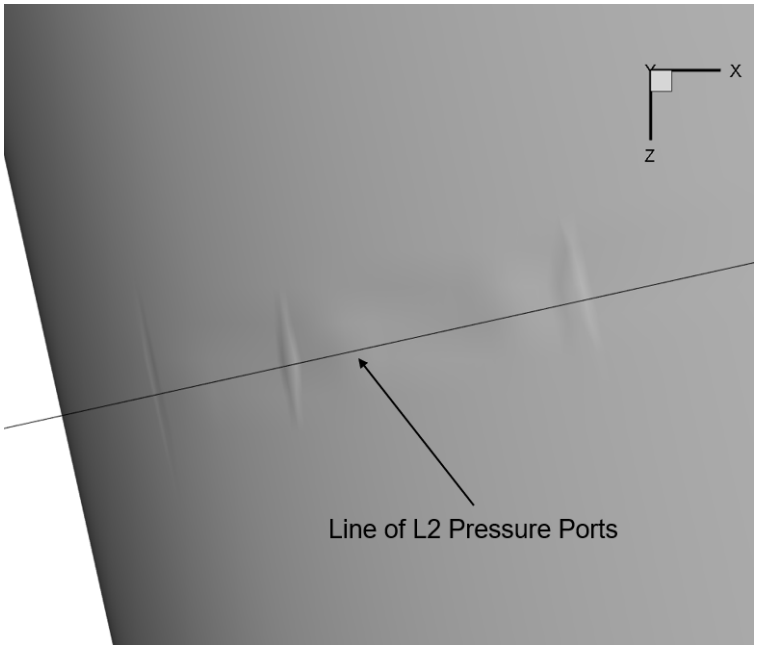

Figure 5.16: Wind Tunnel Computational Model Non-smooth Surface at L2 Pressure Port Location

5.5 Results for N_{crit} of 10.4

Similar to the work described in Section 4.6 that was encouraged by additional study of the behavior of the AFT2 transition prediction model on the S207 airfoil in two dimensions, the effect of freestream turbulence intensity (or N_{crit}) on the transition prediction is further investigated through an additional simulation with the wind tunnel model. Using a N_{crit} value of 10.4, which corresponds to a freestream turbulence intensity of 0.04%, saw closer agreement between CFD solutions for the S207-based TTBW vehicle and the S207 airfoil two-dimensional geometry with design intent [10]. This wind tunnel model simulation was run in an identical manner to the simulation described in the previous section, using up to

30,000 cycles to converge, with the only change being the adjustment in N_{crit} to 10.4. The density residual and lift coefficient convergence histories are compared to the N_{crit} = 6.0 simulation in Figure 5.17. The density residual decreases by the same order of magnitude despite the change in N_{crit}.

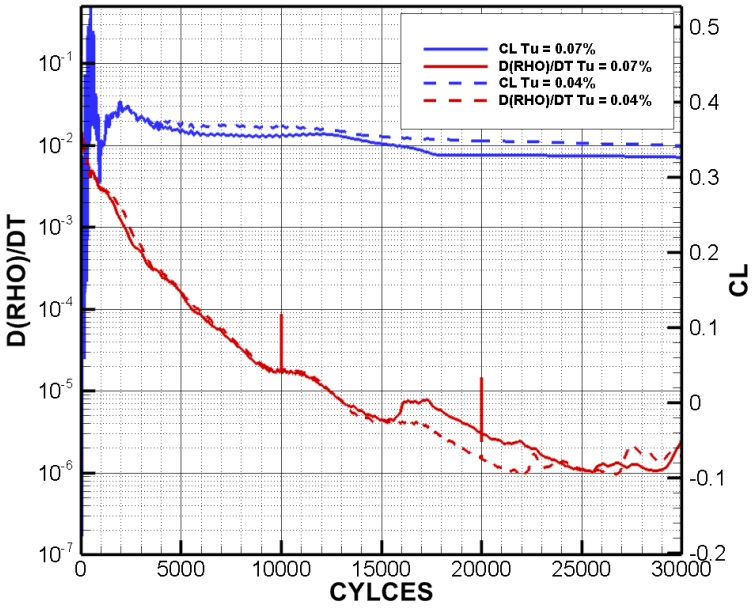

Figure 5.17: Wind Tunnel Model Simulation Convergence Comparison for Varying Freestream Turbulence Intensity

The upper and lower surface skin friction drag contours for the wind tunnel solution in which N_{crit}=10.4 is shown in Figure 5.18. In comparison to the N_{crit}=6.0 simulation after 30000 iterations shown in Figure 5.13e and Figure 5.13f, there is much more laminar flow. The reduction in freestream turbulence intensity results in closer agreement between NSU2D CFD solutions and original S207 airfoil design metrics, and in this case experimental results collected at NASA Ames. Like the results from Section 3.3 and Section 4.6, this apparent inability to replicate desired results for realistic freestream turbulence intensity values suggests the AFT2 transition prediction model implementation is in need of further investigation.

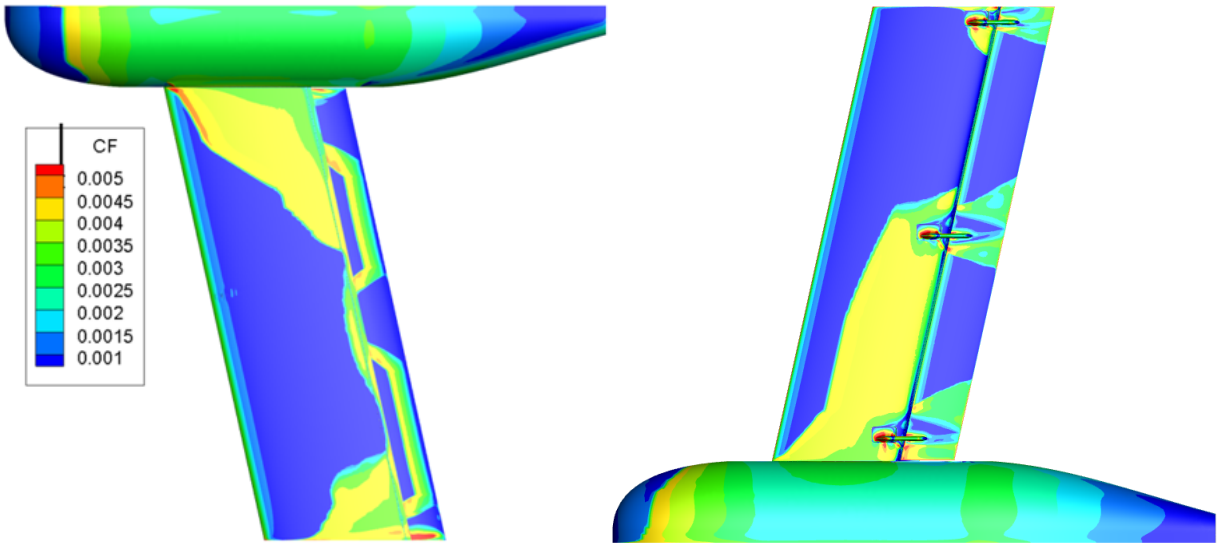

(a) Upper Surface (b) Lower Surface

Figure 5.18: NSU3D-SA-AFT2 Skin Friction Distribution at Mach = 0.7, AOA = 0, Re = 12x10^6, and N_{crit} = 10.4

Chapter 6

Conclusions

The work set forth in this thesis has provided substantial computational evidence supporting the theoretical benefits offered by the S207 SNLF airfoil as the base for a transonic SNLF TTBW aircraft configuration. Additionally, through this work, further ground has been made in the realm of transition prediction modeling.

Computational analysis of the S207 SNLF airfoil as a standalone geometry in two-dimensions with a transition prediction model was successful in reproducing the anticipated performance at nominal flow conditions as set forth in the original design report of the S207 SNLF airfoil [10] when a freeze of the transition prediction equations was invoked. Predicted lift coefficient and drag coefficient values for performed simulations fall within proximity of the low-drag bucket, particularly just slightly lower than the upper limit, of the S207 SNLF airfoil for a Mach number of 0.7, an angle of attack of -1.3°, and Reynolds number of 13.2 million. Additionally, laminar flow was achieved for roughly 84% to 87% the chord length with turbulence being isolated to the upper surface of the aft element. Transition was computed to occur on a small portion of the lower surface of the fore element, which is not in agreement with design intent, for the simulation performed for the S207 airfoil in two dimensions that experienced the longest application of the transition prediction model. This coupled with the difficulty in achieving convergence when the transition equations are permitted to evolve indicates that incorrect performance may be predicted depending on the duration of free transition modeling application. Investigation of the sensitivity of transition locations to

freestream turbulence intensity levels without the use of the freeze of the transition prediction equations was undertaken, and a lower value of 0.04% was found to produce performance characteristics most in line with those predicted in the S207 airfoil design report [10]. A sensitivity study, using the fully turbulent flow assumption, of the S207 airfoil's performance to flap position in two-dimensions showed that detrimental flow behavior is observed for flap displacements greater than 0.1% the chord length. The application of morphed leading edge variants, denoted as the A00, 503, and 511, within a computational framework was successful in increasing the maximum lift coefficient and delaying stall. However, lack of agreement between MSES, OVERFLOW, and NSU2D was observed. NSU2D and OVERFLOW were consistent in computing lift coefficient values up until stall, at which point OVERFLOW predicted the stall angle to be roughly 4° higher than NSU2D. NSU2D and MSES computed the stall angle to be approximately the same value, but NSU2D predicted a higher lift coefficient value at all angles of attack. Further analysis is needed to identify the sources of these discrepancies.

Fully turbulent and free transition modeling approaches were used to uncover geometric anomalies for initial design configurations of an S207-based SNLF TTBW configuration. These CFD results predicted the formation of a shock wave in the slot in the outboard region past the sweep break which led to a redesign of the swept wing. Results generated for a final grid of the S207-based SNLF TTBW configuration using the AFT2 transition prediction model showed that design goals were met in three-dimensions. Significant runs of laminar flow were observed for angles of attack ranging from -1° to 2°, which corresponds with the formation of a low-drag bucket observable through variation of the skin friction drag coefficient as a function of angle of attack. Spanwise lift coefficient values based on the MAC and local chord fell within the upper and lower limits of the low-drag bucket for the S207 SNLF airfoil. However, comparison of fully turbulent sectional surface pressure profiles at select spanwise locations to two-dimensional surface pressure profiles revealed that there is some lack of agreement between two-dimensional and three-dimensional results, particularly through the slot. A full understanding of where this discrepancy originates is still being developed. Three-dimensional effects likely play a role and further three-dimensional

geometric modifications or optimizations may be possible for improving the performance of swept SNLF-based wings. Additionally, the S207-based SNLF TTBW aircraft that was the subject of this study suffered from a poorly designed fairing at the wing-fuselage junction, producing regions of separated flow. Transition from laminar to turbulent flow on the upper surface of the wing, particularly at the root, may have been caused by this flow behavior at the fairing. Variations in the transition locations with freestream turbulence intensity were as expected, with a value of 0.04% resulting in delayed transition.

Simulations conducted in support of wind tunnel experiments completed at NASA Ames resulted in notable differences between computational and experimental results. In the wind tunnel, laminar flow was observed on the entire upper surface of the wing at a Mach number of 0.699, Reynolds number of 12.93 million, and an angle of attack of -0.002°. Computational results predicted the transition from laminar to turbulent flow at approximately 40% the chord length, and adjustments in parameters such as CFL saw only minor changes in the final solution. Differences in computational and experimental results were further studied through comparison of surface pressure profiles at three pressure port row locations. At each location there was a significant difference in the pressures present through the slot. Additionally, at the most outboard station of the CFD solution, flow separation was indicated by a lower, constant pressure on the upper surface of the aft element. Full understanding of where differences between computational and experimental results originate has yet to be acquired. However, the current model did not consider the added thickness of the paint layer, and the modeling approach did not consider possible aeroelastic deflections experienced in the wind tunnel. Additionally, variations in the wind tunnel results at near identical flow conditions suggest that repeatability of experimental results may suffer, particularly at the slot where performance is known to be significantly impacted by small geometric variations.

Additional investigation of the behavior of the AFT2 transition prediction model inspired by evidence of a slow transient present on the wind tunnel model supports the claim that the AFT2 model implementation is in need of further investigation. Though the model is successful in predicting trends in laminar flow as a function of angle of attack, failure to meet design metrics was observed for the two-dimensional S207 geometry without the

freeze of the transition equations. This was only remediated with a reduction in freestream turbulence intensity to a value that was lower than that used in the MSES design runs [10]. This adjustment saw more agreement between results obtained with the three-dimensional TTBW and wind tunnel geometries with design intent as well.

This work has demonstrated the benefit in using CFD for the analysis of SNLF type wings. A turbulence model can be applied independently, but also coupled with a transition prediction model to more accurately capture the physics associated with laminar flow. Consequently, performance benefits that accompany extensive runs of laminar flow can be quantified through comparison of results acquired using each modeling capability. This was done with the standalone S207 SNLF airfoil in two dimensions at cruise conditions, and a higher lift and lower drag was predicted by the free transition approach. Additionally, the impact of laminar flow can be further explored by applying it to surfaces of interest in three dimensions. This was done for the final configuration of the S207-based SNLF TTBW aircraft using the patch- and box-based transition prediction model application capability.

Though the use of free transition is vital for SNLF airfoil analysis, fully turbulent modeling has its place in the computational framework. Transition prediction modeling is a new science, still in the infancy of its understanding, and so it is accompanied by unique challenges. With application of free transition, a substantial increase in computation time is often observed. Furthermore, achieving convergence becomes more challenging due to the flow physics, as well as slow transients that may affect transition location and require excessive computing time. Fully turbulent simulations then serve as a valuable tool for gaining insight to performance trends. This was evident in the two-dimensional flap position study, where application of the fully turbulent flow assumption was advantageous, especially for the larger flap displacements that saw severe flow separation and shock wave formation.

There are several possible routes for work moving forward in this area. It is known that the S207-based SNLF TTBW aircraft considered for this work had a poorly designed fairing at the wing-fuselage junction. It is suspected that the flow separation observed as a consequence of this design is causing the transition from laminar to turbulent flow at the root of the wing. Thus, a redesign of the fairing can be undertaken, and subsequent impact on transition

location can be studied. Further investigation toward identifying sources of the disagreement observed between two-dimensional and three-dimensional pressure profiles is necessary, particularly for the slot region. This may be improved with further geometric changes, and determining whether closer alignment between three-dimensional and two-dimensional pressure profiles will establish a more aft transition line on the three-dimensional geometry is worth additional efforts. An optimization strategy, such as the gradient-based adjoint method [47], may be used to conduct a twist distribution or general shape optimization. Efforts on this front, including the effect of structural displacements, have already been conducted on an SNLF-based configuration [33]. This strategy may result in more closely aligned pressure profiles between three-dimensional and two-dimensional results. Furthermore, the computational framework is in need of further development. Currently implemented transition prediction models do not consider the effects of cross flow instabilities. Though in context to this work cross flow instabilities are not expected to trigger transition given the sweep angle of the considered SNLF TTBW aircraft configuration, the capability to computationally account for this mechanism offers certainty and understanding in its relevance to a swept SNLF wing. Additionally, notable difficulty is still experienced with converging free transition simulations. Though the models used in this work were validated, discrepancies between CFD solutions and experimental results collected at NASA Ames were still observed. This may be due partially to geometry and this will be explored further in the near future via a run with an updated model that considers the thickness of the paint. However, the slow and sometimes incomplete convergence of free transitional simulations makes it difficult to assess whether observed discrepancies are due to model performance or incomplete convergence. Further study of grids used in three dimensions is also needed. Although the grids run for results presented in this work were quite fine, it is probable they are not as well resolved as the two-dimensional S207 SNLF airfoil grid. Parameters such as streamwise resolution, spanwise resolution, and boundary layer resolution, and their impact on the transition line location needs to be studied further. Particularly, boundary layer resolution guidelines typically used for fully turbulent simulations need to be reconsidered as laminar boundary layers are much thinner than turbulent boundary layers.

References

[1] International Energy Agency, "CO_2 Emmissions From Fuel Combustion: Highlights," 2019. Accessed Nov., 2022. URL: https://iea.blob.core.windows.net/assets/eb3b2e8d-28e0-47fd-a8ba-160f7ed42bc3/CO2_Emissions_from_Fuel_Combustion_2019_Highlights.pdf.

[2] S. Gossling and A. Humpe, "The Global Scale, Distribution and Growth of Aviation: Implications for Climate Change," *Global Environmental Change*, vol. 65, 2021. doi: https://doi.org/10.1016/j.gloenvcha.2020.102194.

[3] O. Boucher, A. Borella, T. Gasser, and D. Hauglustaine, "On the Contribution of Global Aviation to the CO_2 Radiative Forcing of Climate," *Atmospheric Environment*, vol. 267, 2018. doi: https://doi.org/10.1016/j.atmosenv.2021.118762.

[4] NASA Aeronautics, "Strategic Implementation Plan: 2019 Update," 2019. Accessed Aug., 2021. URL: https://nasa.gov/aeroresearch/strategy.

[5] S. Gudmundsson, "Aircraft Drag Analysis," in *General Aviation Aircraft Design*, pp. 661–760, Butterworth-Heinemann, 2014. doi: http://dx.doi.org/10.1016/B978-0-12-397308-5.00015-5.

[6] D. Somers, "An Exploratory Investigation of a Slotted, Natural-Laminar-Flow Airfoil," NASA/CR-2012-217560, July, 2012.

[7] D. Somers, "Laminar Flow Airfoil," US Patent 6905092 B2, June 14, 2005.

[8] J. Coder and D. Somers, "Design of a Slotted, Natural-Laminar-Flow Airfoil for Commercial Transport Applications," *Aerospace Science and Technology*, vol. 106, Nov. 2020. doi: https://doi.org/10.1016/j.ast.2020.106217.

[9] A.M.O. Smith, "High-Lift Aerodynamics," *Journal of Aircraft*, vol. 12, no. 6. doi: https://doi.org/10.2514/3.59830.

[10] D. Somers, "Design of a Slotted, Natural-Laminar-Flow Airfoil for Transport Aircraft," NASA/CR-2019-220403, June, 2019.

[11] J. Coder, M. Maughmer and D. Somers, "Theoretical and Experimental Results for the S414, Slotted, Natural-Laminar-Flow Airfoil," *Journal of Aircraft*, vol. 51, no. 6, pp. 1883–1890, Nov. 2014. doi: https://doi.org/10.2514/1.C032566.

[12] M. Maughmer, J. Coder and D. Somers, "Exploration of a Slotted, Natural-Laminar-Flow Airfoil Concept," AIAA Paper 2018-3815, 2018 Applied Aerodynamics Conference, July 25-29, Atlanta, GA. doi: https://doi.org/10.2514/6.2018-3815.

[13] D. Somers, "Design of a Slotted, Natural-Laminar-Flow Airfoil for Business Jet Applications," NASA/CR-20120217559, April, 2012.

[14] M. Bradley and C. Droney, "Subsonic Ultra Green Aircraft Research Phase 2: N+4 Advanced Concept Development," NASA/CR-20120217556, May, 2012.

[15] J. Coder, "Advanced Aerodynamic Design Center for ultra-Efficient Commercial Vehicles: ARMD Strategic Thrust: Ultra-Efficient Commercial Vehicles (Thrust 3A)," Presented at the University Leadership Initiative Annual Review, Sep., 2021.

[16] P. Camacho, K. Pham, L. Chou, N Harrison and A. Khodadoust, "Progress on Aerodynamic Performance Analysis of SNLF Transonic Truss-Braced Wing," AIAA Paper 2020-1025, 2020 AIAA SciTech Forum, Jan. 6-10, Orlando, FL. doi: https://doi.org/10.2514/6.2020-1025.

[17] C. Perkins, Z. Yang, I. Topcuoglu, D. Mavriplis, J. Coder, E. Hereth, and C. Axten, "Aerodynamic Analysis of a Slotted, Natural-Laminar-Flow Transonic Trussed-Braced

Wing Aircraft Configuration," AIAA Paper 2022-2536, 2021 AIAA SciTech Forum, Jan 3rd-7th, San Diego, CA. doi: https://doi.org/10.2514/6.2022-2536.

[18] C. Perkins, Z. Yang, D. Mavriplis, J. Coder, C. Axten, and L. Shoemake, "Effect of transition modeling for analysis of a slotted, natural-laminar-flow transonic truss-braced wing aircraft configuration," 2023. AIAA Paper 2023-XXXX, To be presented at the 2023 AIAA SciTech Forum, San Diego, CA., Jan 23-27, 2022.

[19] S. Klausmeyer and J. Lin, "Comparative Results From a CFD Challenge Over a 2D Three-Element High-Lift Airfoil," 1997. NASA TM-112858.

[20] F. Menter, P. Smirnov, and T. Liu, "A One-Equation Local Correlation-Based Transition," *Flow, Turbulence and Combustion*, vol. 95, no. 1, pp. 593–619, 2015. doi: https://doi.org/10.1007/s10494-015-9622-4.

[21] F. Menter, R. Langtry and S. Volker, "Transition Modelling for General Purpose CFD," *Flow, Turbulence and Combustion*, vol. 77, no. 1, pp. 202–277, 2006. doi: https://doi.org/10.1007/s10494-006-9047-1.

[22] R. Nichols, "Addition of a Local Correlation-Based Boundary Layer Transition model to the CREATETM-AV Kestrel Unstructured Flow Solver," 2019. AIAA Paper 2019-1343, 2019 AIAA SciTech Forum, Jan. 7-11, San Diego, CA. doi: https://doi.org/10.2514/6.2019-1343.

[23] J. Coder, "Further Development of the Amplification Factor Transport Transition Model for Aerodynamic Flows," AIAA Paper 2019-0039, 2019 AIAA SciTech Forum, Jan. 7-11, San Diego, CA. doi: https://doi.org/10.2514/6.2019-0039.

[24] L. Mack, "Transition and Laminar Instability," 1977. NASA CR-153203.

[25] Z. Yang and D. Mavriplis, "Implementation of Transition Modeling for Analysis and Optimization of Two-Dimensional Airfoil Problems," AIAA Paper 2019-0293, 2019 AIAA SciTech Forum, Jan. 7-11, San Diego, CA. doi: https://doi.org/10.2514/6.2019-0294.

[26] W. Valarezo and D. Mavriplis, "Navier-Stokes Applications to High-Lift Airfoil Analysis," *Journal of aircraft*, vol. 32, no. 3, pp. 618–624, 1995. doi: https://doi.org/10.2514/3.46764.

[27] P. Spalart and S. Allmaras, "A One-Equation Turbulence Model for Aerodynamic Flow," *Recherche Aerospatiale*, pp. 5–21, 1994. doi: https://doi.org/10.25.14/6.1992-439.

[28] D. Mavriplis, "An Advancing Front Delaunay Triangulation Algorithm Designed for Robustness," *Journal of Computational Physics*, vol. 117, no. 1, pp. 90–101, 1995. doi: https://doi.org/10.1006/jcph.1995.1047.

[29] K. Mani and D. Mavriplis, "Unstructured Mesh Solution Techniques Using the NSU3D Solver," 2014. AIAA Paper 2014-0081, 52nd Aerospace Sciences Meeting, January 2014. doi: https://doi.org/10.2514/6.2014-0081.

[30] M. Park, K. Laflin, M. Chaffin, N. Powell and D. Levy, "CFL3D, FUN3D, and NSU3D Contributions to the Fifth Drag Prediction Workshop," *Journal of Aircraft*, vol. 51, no. 4, pp. 1268–1283, July 2014. doi: https://doi.org/10.2514/1.C032613.

[31] D. Mavriplis, M. Long, T. Lake and M. Langlois, "NSU3D Results for the Second AIAA High Lift Prediction Workshop," *Journal of Aircraft*, vol. 52, no. 4, pp. 1063–1081, Aug. 2015. doi: https://doi.org/10.2514/1.C033042.

[32] D. Mavriplis, Z. Yang and M. Long, "Results Using NSU3D for the First Aeroelastic Prediction Workshop," AIAA Paper 2013-0786, 51st AIAA Aerospace Sciences Meeting, Jan. 7-10, 2013, Dallas/FT. Worth, TX. doi: https://doi.org/10.2514/6.2013-786.

[33] D. Mavriplis, Z. Yang, and E. Anderson, "Development of an Analysis and Optimization Tool for Slotted Wing Natural-Laminar-Flow Aircraft," AIAA Paper 2020-1292, 2020 AIAA SciTech Forum, Jan 6-10, Orlando, FL. doi: https://doi.org/10.2514/6.2020-1292.

[34] R. Petzold and R. Radespiel, "Transition on a Wing with Spanwise Varying Crossflow and Linear Stability Analysis," *AIAA Journal*, vol. 53, no. 2, pp. 321–335, Feb. 2015. doi: https://doi.org/10.2514/1.J053127.

[35] Z. Yang and D. Mavriplis, "Improved Fluid-Structure Interface for Aeroelastic Computations with Non-Matching Outer Mold Lines," AIAA Paper 2021-0844, 2021 AIAA SciTech Forum, Virtual Event, Jan 2021. doi: https://doi.org/10.2514/6.2021-0844.

[36] M. Drela, "A User's Guide to MSES 3.05," MIT Department of Aeronautics and Astronautics, July 2007.

[37] A. Bottai, R. Campbell and M. Johnson, "Vibrations of a High-Aspect Ratio, Two Element Wing," 2022. AIAA Paper 2022-2537, AIAA SciTech Forum, San Diego, CA., Jan 3-7, 2022. doi: https://doi.org/10.2514/10.2514/6.2022-2537.

[38] D. Twiss, C. Colletti, and P. Ansell, "High-Lift Configuration of a Slotted Natural Laminar Flow Airfoil," 2019. AIAA Paper 2019-0291, AIAA Scitech Forum, San Diego, CA., Jan 7-11. doi: https://doi.org/10.2514/6.2019-0291.

[39] H. Ortiz-Melendez, J. Coder, and A. Shmilovich, "High-Lift Simulations of Slotted, Natural-Laminar-Flow Airfoils," 2019. AIAA Paper 2019-0290, AIAA Scitech Forum, San Diego, CA., Jan 7-11. doi: https://doi.org/10.2514/6.2019-0290.

[40] H. Ortiz-Melendez, E. Long, G. Toth, K. Keely, and J. Coder, "High-Lift Simulations of Slotted, Natural-Laminar-Flow Airfoils with Drooped Leading Edge," 2020. AIAA Paper 2020-1289, AIAA SciTech Forum, Orlando, FL, Jan 6-10. doi: https://doi.org/10.2514/6.2020-1289.

[41] C. Colletti and P. Ansell, "Design of an Airfoil Morphing Leading Edge for High-Lift Applications using a Genetic Algorithm," 2021. AIAA Paper 2021-0947, AIAA SciTech Forum, Virtual Event, Jan 11-15 & 19-21. doi: https://doi.org/10.2514/6.2021-0947.

[42] C. Colletti and P. Ansell, "Airfoil Morphed Leading Edge Design for High-Lift Applications using a Genetic Algorithm," *Journal of Aircraft*. Under Review.

[43] M. Bradley and C. Droney, "Subsonic Ultra Green Aircraft Research: Phase 2. Volume 2; Hybrid Electric Design Exploration," NASA/CR-2015-218704/Volume II, NASA Langley Research Center, Hampton, VA, April 2015.

[44] L. Metkowski and M. Maughmer, "Winglet and Strut Configuration Study for a Slotted, Natural-Laminar-Flow Strut-Braced Transport Aircraft," AIAA Paper 2021-0843, AIAA Scitech Forum 2021, Virtual event, January 2021. doi: `https://doi.org/10.2514/6.2021-0843`.

[45] K. Risse, F. Schueltke and E. Stumpf, "Conceptual Wing Design Methodology for Aircraft with Hybrid Laminar Flow Control," AIAA Paper 2014-0023, AIAA SciTech 2014 Forum, Jan. 1014. doi: `https://doi.org/10.2514/6.2014-0023`.

[46] R. Cummings, W. Mason, S. Morton and D. McDaniel, "Applied Computational Aerodynamics: A Modern Engineering Approach," 2015. Cambridge Aerospace Series, New York NY. doi: `https://doi.org/10.1017/CBO9781107284166`.

[47] E. Nielson, "Adjoint-Based Aerodynamic Design of Complex Aerospace Configurations," FEDSM2016-7573, Proceedings of the ASME 2016 Fluids Engineering Division Summer Meeting, Washington D.C., July 10-14 2016.